

HARVARD UNIVERSITY  
Graduate School of Arts and Sciences



DISSERTATION ACCEPTANCE CERTIFICATE

The undersigned, appointed by the

Department of Physics

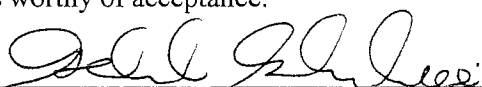
have examined a dissertation entitled

Antimatter Plasmas Within a Penning-Ioffe Trap


presented by

William Steven Kolthammer

candidate for the degree of Doctor of Philosophy and hereby  
certify that it is worthy of acceptance.

Signature 

Typed name: Professor Gerald Gabrielse, Chair

Signature 

Typed name: Professor Adam Cohen

Signature 

Typed name: Professor John Doyle

Date: September 14, 2011



# Antimatter Plasmas Within a Penning-Ioffe Trap

A dissertation presented

by

William Steven Kolthammer

to

The Department of Physics

in partial fulfillment of the requirements

for the degree of

Doctor of Philosophy

in the subject of

Physics

Harvard University

Cambridge, Massachusetts

September 2011

UMI Number: 3491922

All rights reserved

INFORMATION TO ALL USERS

The quality of this reproduction is dependent upon the quality of the copy submitted.

In the unlikely event that the author did not send a complete manuscript and there are missing pages, these will be noted. Also, if material had to be removed, a note will indicate the deletion.



UMI 3491922

Copyright 2012 by ProQuest LLC.

All rights reserved. This edition of the work is protected against unauthorized copying under Title 17, United States Code.



ProQuest LLC  
789 East Eisenhower Parkway  
P.O. Box 1346  
Ann Arbor, MI 48106-1346

©2011 - William Steven Kolthammer

All rights reserved.

Thesis advisor

Author

**Professor Gerald Gabrielse**

**William Steven Kolthammer**

## **Antimatter Plasmas Within a Penning-Ioffe Trap**

### **Abstract**

Improved techniques for preparing cold antimatter plasmas and a new apparatus for trapping antihydrogen bring us closer to the long-term goal of the precise spectroscopy of antihydrogen. Antihydrogen is synthesized within a magnetic trap for the first time. With the aim to capture a large number of antihydrogen atoms, we implement methods to characterize and control the antiproton and positron plasmas from which they are produced. The geometry and density of trapped plasmas are determined by measurements of internal oscillation frequencies and controlled with rotating electric fields. The temperature of plasmas are investigated by two methods: direct measurement of the axial energy distribution and the temperature dependence of oscillation frequencies. Improved accumulation methods prepare plasmas of up to 10 million antiprotons and 4 billion positrons, a greater than ten-fold improvement in each case. Antiproton cooling by embedded electrons and adiabatic expansion produce temperatures as low as 3.5 K, the coldest antiprotons yet achieved. Centrifugal separation in antiproton-electron plasmas is observed for the first time. The design and construction of a second-generation apparatus is discussed. A unique magnetic trap provides for single-atom detection, an improved trap depth, and the generation of two trap geometries.

# Contents

Title Page . . . . .	i
Abstract . . . . .	iii
Table of Contents . . . . .	iv
Publications . . . . .	vii
<b>1 Introduction</b>	<b>1</b>
1.1 Antihydrogen and Fundamental Physics . . . . .	2
1.2 A Brief History of Antihydrogen Research . . . . .	6
1.3 Overview of this Work . . . . .	9
<b>2 Apparatus and Standard Methods</b>	<b>13</b>
2.1 Penning-Ioffe Trap . . . . .	15
2.1.1 Penning Trap . . . . .	17
2.1.2 Ioffe Trap . . . . .	20
2.2 Particle Loading . . . . .	23
2.2.1 Electron Loading . . . . .	23
2.2.2 Antiproton Loading . . . . .	24
2.2.3 Positron Loading . . . . .	26
2.3 Particle Transfer and Detection . . . . .	27
2.3.1 Particle Transfer . . . . .	27
2.3.2 Charge Counting . . . . .	28
2.3.3 Antiproton Annihilation Detection . . . . .	29
<b>3 Search for Trapped Antihydrogen</b>	<b>32</b>
3.1 Charged Particles Confined in a Penning-Ioffe Trap . . . . .	33
3.2 Antihydrogen Produced in a Penning-Ioffe Trap . . . . .	38
3.3 Search for Trapped Antihydrogen . . . . .	41
3.4 Discussion . . . . .	44
<b>4 Controlling the Geometry of Trapped Plasmas</b>	<b>46</b>
4.1 Theory . . . . .	47

4.2	Plasma Modes of Oscillation . . . . .	50
4.2.1	Instrumentation and an Example Measurement . . . . .	52
4.2.2	Controlling the Geometry of a Plasma with Trap Fields . . . . .	56
4.3	Compression of a Plasma by a Rotating Electric Field . . . . .	56
4.3.1	Demonstration . . . . .	58
4.3.2	Suggestions for Further Rotating-Wall Studies . . . . .	62
4.4	Summary . . . . .	63
<b>5</b>	<b>Measuring the Temperature of Trapped Plasmas</b>	<b>65</b>
5.1	Axial Energy Distribution . . . . .	66
5.1.1	Space-Charge Potential Model . . . . .	71
5.1.2	Measurement Example . . . . .	74
5.1.3	Discussion . . . . .	75
5.2	Measurement of Plasma Oscillation Frequencies . . . . .	77
5.2.1	Background and Theory . . . . .	77
5.2.2	Measurements . . . . .	78
5.2.3	Discussion . . . . .	81
<b>6</b>	<b>Embedded-Electron and Adiabatic Cooling of Antiprotons to 4 K</b>	<b>84</b>
6.1	Embedded-Electron Cooling . . . . .	85
6.1.1	Temperature Rate Equations . . . . .	88
6.1.2	Counting Embedded Electrons . . . . .	89
6.2	Adiabatic Cooling . . . . .	90
6.3	Discussion . . . . .	93
<b>7</b>	<b>Improved Particle Accumulation: <math>10^7</math> Antiprotons and <math>10^9</math> Positrons</b>	<b>96</b>
7.1	Improved Antiproton Accumulation . . . . .	97
7.1.1	Increased Magnetic Fields . . . . .	99
7.1.2	Compression of Antiprotons by a Rotating Wall . . . . .	101
7.2	Improved Positron Accumulation . . . . .	104
<b>8</b>	<b>Centrifugal Separation of Antiprotons and Electrons</b>	<b>107</b>
8.1	Density Distribution and Separation Temperature . . . . .	108
8.2	Measurement by Axial Ejection . . . . .	110
8.3	Measurement by Magnetic Expansion . . . . .	113
8.4	Discussion and Suggestions for Further Studies . . . . .	115
<b>9</b>	<b>An Improved Penning-Ioffe Trap</b>	<b>117</b>
9.1	Design Objectives . . . . .	119
9.2	Winding Design . . . . .	122
9.3	Liquid Helium Enclosure . . . . .	127
9.4	Rapid Turn Off and Quench Protection . . . . .	129
9.5	Penning Trap and Cryostat . . . . .	132



---

<b>10 Conclusion</b>	<b>134</b>
<b>Bibliography</b>	<b>139</b>

# Publications

1. *Adiabatic cooling of antiprotons*  
G. Gabrielse, W.S. Kolthammer, R. McConnell, P. Richerme, R. Kalra, E. Novitski, D. Grzonka, W. Oelert, T. Sefzick, M. Zielinski, D. Fitzakerley, M.C. George, E.A. Hessels, C.H. Storry, M. Weel, A. Müllers, and J. Walz, Physical Review Letters **106**, 073002 (2011).
2. *Pumped helium system for producing 1.2 K positrons and electrons*  
J. Wrubel, G. Gabrielse, W.S. Kolthammer, P. Larochele, R. McConnell, P. Richerme, D. Grzonka, W. Oelert, T. Sefzick, M. Zielinski, J.S. Borbely, M.C. George, E.A. Hessels, C.H. Storry, M. Weel, A. Müllers, J. Walz, and A. Speck, Nuclear Instruments and Methods in Physics Research A **640**, 232 (2011).
3. *Centrifugal separation of antiprotons and electrons*  
G. Gabrielse, W.S. Kolthammer, R. McConnell, P. Richerme, J. Wrubel, R. Kalra, E. Novitski, D. Grzonka, W. Oelert, T. Sefzick, J.S. Borbely, D. Fitzakerley, M.C. George, E.A. Hessels, C.H. Storry, M. Weel, A. Müllers, J. Walz, and A. Speck, Physical Review Letters **105**, 213002 (2010).
4. *Antihydrogen production within a Penning-Ioffe trap*  
G. Gabrielse, P. Larochele, D. Le Sage, B. Levitt, W.S. Kolthammer, R. McConnell, P. Richerme, J. Wrubel, A. Speck, M.C. George, D. Grzonka, W. Oelert, T. Sefzick, Z. Zhang, A. Carew, D. Comeau, E.A. Hessels, C.H. Storry, M. Weel, and J. Walz, Physical Review Letters **100**, 113001 (2008).
5. *Single-component plasma of photoelectrons*  
B. Levitt, G. Gabrielse, P. Larochele, D. Le Sage, W.S. Kolthammer, R. McConnell, J. Wrubel, A. Speck, D. Grzonka, W. Oelert, T. Sefzick, Z. Zhang, D. Comeau, M.C. George, E.A. Hessels, C.H. Storry, M. Weel, and J. Walz, Physics Letters B **656**, 25 (2007).
6. *Density and geometry of single component plasmas*  
A. Speck, G. Gabrielse, P. Larochele, D. Le Sage, B. Levitt, W.S. Kolthammer, R. McConnell, J. Wrubel, D. Grzonka, W. Oelert, T. Sefzick, Z. Zhang, D. Comeau, M.C. George, E.A. Hessels, C.H. Storry, M. Weel, and J. Walz, Physics Letters B **650**, 119 (2007).
7. *Antiproton confinement in a Penning-Ioffe trap for antihydrogen*  
G. Gabrielse, P. Larochele, D. Le Sage, B. Levitt, W.S. Kolthammer, I. Kuljanishvili, R. McConnell, J. Wrubel, F.M. Esser, H. Glückler, D. Grzonka, G. Hansen, S. Martin, W. Oelert, J. Schillings, M. Schmitt, T. Sefzick, H. Soltner, Z. Zhang, D. Comeau, M.C. George, E.A. Hessels, C.H. Storry, M. Weel, A. Speck, F. Nillius, J. Walz, and T.W. Hänsch, Physical Review Letters **98**, 113002 (2007).

# Chapter 1

## Introduction

Antihydrogen provides a unique opportunity to investigate fundamental physics with antimatter. As the counterpart to the common hydrogen atom, antihydrogen ( $\bar{\text{H}}$ ) consists of a positron ( $e^+$ ) and antiproton ( $\bar{p}$ ). Antihydrogen atoms are stable and amenable to the precise experimental control achieved in modern atomic physics. This provides the potential for new and compelling measurements with antimatter such as precise spectroscopy and the study of gravitational acceleration. A few years ago, low-energy  $\bar{\text{H}}$  was synthesized for the first time [1, 2, 3]. A central goal of  $\bar{\text{H}}$  research is now to capture substantial numbers of  $\bar{\text{H}}$  atoms in a neutral particle trap for the long-time confinement required for laser cooling and spectroscopy [4]. This thesis present progress toward that ambition.

We begin with initial experiments performed in a combined Penning-Ioffe trap [5], an apparatus designed to confine  $\bar{\text{H}}$  produced from trapped positrons and antiprotons. These studies include the first synthesis of  $\bar{\text{H}}$  within an atom trap [6] and efforts to detect captured atoms. We find that too few atoms are trapped to enable

spectroscopy, so the principle focus of this thesis becomes the development of experimental methods and apparatus for increasing the quantity of trapped  $\bar{\text{H}}$  and the sensitivity with which we can detect it.

To this end, we explore and implement techniques to fully characterize the trapped plasmas used in  $\bar{\text{H}}$  production. These diagnostics are used to investigate novel techniques to cool  $\bar{\text{p}}$ , improve  $\bar{\text{p}}$  accumulation, and study the dynamics of electron-antiproton plasmas. Antiproton plasmas containing up to 10 million particles as cold as 3.5 K (a factor of three colder and  $10^4$  more particles than previously realized for cryogenic  $\bar{\text{p}}$ ) are prepared for  $\bar{\text{H}}$  experiments. These improved  $\bar{\text{p}}$  plasmas promise direct application in greatly increasing the number of trapped  $\bar{\text{H}}$ , and the diagnostics developed for  $\text{e}^+$  plasmas will enable careful study of the formation of cold, trappable  $\bar{\text{H}}$ . The second focus of this thesis is the design and construction of a second-generation Penning-Ioffe trap for antihydrogen studies. The principle improvement in this apparatus is a unique Ioffe trap which provides an improved trap depth, generation of multiple field geometries, and a brief turn-off time for detection of a single trapped atom.

## 1.1 Antihydrogen and Fundamental Physics

A principle motivation for this work is to achieve a precise test of  $CPT$  symmetry. This symmetry pertains to an invariance of fundamental theories to the combined operations of charge conjugation ( $C$ ), parity inversion ( $P$ ), and time reversal ( $T$ ). Although it is not a readily apparent property of nature, invariance to this combination of operations is at the core of modern physics.  $CPT$  invariance is feature

of any Lorentz-invariant local quantum field theory [7], and as such it underlies the Standard Model of particle physics. A consequence of *CPT* symmetry that is accessible to precise low-energy tests is that a particle and its corresponding antiparticle have equal masses and opposite electric charges. For hydrogen and antihydrogen, *CPT* invariance predicts equal bound-state energies and, thus, identical spectra – a prediction that we strive to precisely test.

Until fifty years ago, it was widely believed that each of the discrete operations that constitute *CPT* corresponded to individual symmetries. These were seen as intuitive properties of nature, and there were no experimental observations to the contrary. In 1956, however, a proposal was made to test *P* invariance of weak interactions for the first time [8]. Remarkably, *P* violation was demonstrated shortly thereafter in the  $\beta$ -decay from polarized  $^{60}\text{Co}$  [9]. Experimental confirmation followed, and it was soon accepted that *P* symmetry is in fact maximally violated in the weak interaction. Shortly thereafter, it was proposed instead that nature is invariant under the combined transformation *CP* [10], and this became a widely accepted symmetry of nature. In 1964, however, a small *CP* violation was first observed in the decay of neutral kaons [11].

It now appears that nature is invariant under the combined transformation *CPT*. This symmetry has been supported by all observations to date, and as mentioned, it appears to be an intrinsic feature of quantum field theories. On the other hand, there are serious problems yet resolved by this theoretical framework. Notably, a quantum field theory of gravity has yet to be formulated, and we lack a compelling explanation for the observed matter-antimatter baryon asymmetry in the observable

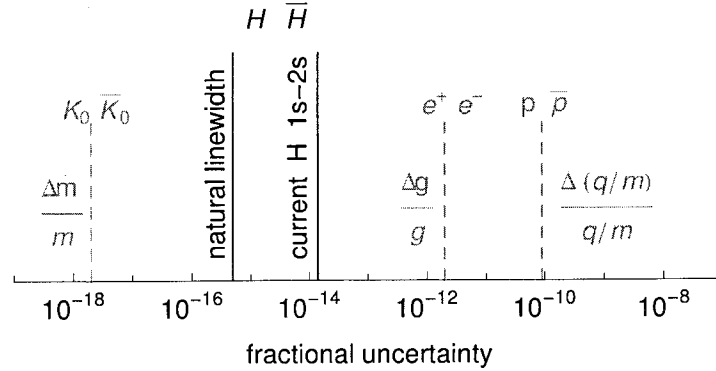


Figure 1.1: Comparison of fractional precisions relevant to hydrogen 1s–2s spectroscopy (black) and precise  $CPT$  tests (gray), including kaon mass [16], electron magnetic moment [17], and proton charge-to-mass ratio [18] comparisons. Adapted from Ref. [19].

universe. Given the scope of these challenges that confront modern physics, it seems prudent to precisely investigate  $CPT$  symmetry in various aspects of nature accessible to measurement.

An attractive  $CPT$  test with  $H$  and  $\bar{H}$  is provided by two-photon spectroscopy of the 1s–2s transition. For  $H$ , this transition has been measured to a relative uncertainty of  $1.4 \times 10^{-14}$ , and the fractional linewidth of  $5 \times 10^{-16}$  suggests further improvements are attainable [12]. However, this measurement was achieved with a cold  $H$  beam, an approach that would require the production of  $\bar{H}$  beyond foreseeable capabilities. The scarcity of  $\bar{H}$  motivates us instead to undertake spectroscopy in a magnetic trap [4]. For trapped  $H$ , a relative uncertainty of  $1.2 \times 10^{-12}$  on the 1s–2s frequency was achieved in a measurement limited by laser stability [13]. As proposed in Ref. [14], it appears this level of accuracy can be achieved with  $10^3 \bar{H}$  at 0.2 K in a magnetic trap, and one-atom spectroscopy may become possible in the future [14, 15].

Figure 1.1 compares these hydrogen 1s–2s benchmarks to the relative uncertainty

achieved by a variety of tests of *CPT* symmetry. The decay of neutral kaons can be interpreted as a mass comparison with a relative uncertainty of  $10^{-18}$  [16]. For leptons and baryons, the most precise tests currently involve the study of single particles in a Penning trap [17, 18]. While the relative natural linewidth indicates an eventual potential for the measurement, even at a relative uncertainty of  $10^{-12}$ , 1s–2s spectroscopy of H and  $\bar{\text{H}}$  achieves a greater relative uncertainty than current tests with either leptons or baryons. To directly compare these measurements, we may consider the associated Rydberg constants

$$\frac{(R_\infty)_{\bar{\text{H}}}}{(R_\infty)_{\text{H}}} = \frac{m_{e^+}}{m_{e^-}} \left( \frac{q_{\bar{\text{p}}}}{q_{\text{p}}} \right)^2 \left( \frac{q_{e^+}}{q_{e^-}} \right)^2 \frac{1 + m_{e^-}/m_{\text{p}}}{1 + m_{e^+}/m_{\bar{\text{p}}}} \quad (1.1)$$

where for this comparison, we needn't consider the small additional nuclear affects included in deducing  $R_\infty$  from the 1s–2s frequency at high precision [20]. With this framework, we see that the proposed comparison of  $\bar{\text{H}}$  and H is most sensitive to the equality of the charges of the constituent particles as well as the masses of the leptons.

Without a specific theory for *CPT* violation, it is not clear how various tests of *CPT* can be compared. For this reason, above we argued for precise tests in a variety of sectors. A possible framework for comparing various measurements is provided by the Standard-Model Extension, an effective field theory that seeks to parameterize small Lorentz violating additions to the Standard Model (some of which involve *CPT* violation) that are consistent with other seemingly well-grounded principles such as energy-momentum conservation [21]. Within this framework, it has been verified that precise spectroscopy of the 1s–2s transition in trapped H and  $\bar{\text{H}}$  promises an improved constraint on Lorentz violation [22]. It is also noted that the hyperfine transition between the two trapped low-field-seeking states, which amounts to a proton (or  $\bar{\text{p}}$ )

spin flip, provides for a separate test of *CPT* violation related to the proton (and  $\bar{p}$ ) magnetic moments. An ambitious experiment underway at CERN is working towards producing a spin-polarized  $\bar{H}$  beam suitable for such a measurement [23].

Lastly, we mention the intriguing possibility that cold  $\bar{H}$  may provide for the first measurement of the gravitational acceleration of antimatter. Notably,  $\bar{H}$  avoids the stringent requirements on stray electric fields that predictably thwarted previous gravitational studies with antiprotons [24]. The challenge of a precise measurement of gravitation even with  $\bar{H}$ , however, is apparent from a comparison of thermal and gravitational energies. The short wavelength of cooling transitions and small mass conspire to set foreseeable laser cooling limits at roughly 1 mK [25], and as pointed out in Ref. [26], 1 mK of energy is approximately equal to the gravitational energy gained by an  $\bar{H}$  atom elevated by 1 m. As  $\bar{H}$  trapping and cooling methods advance, however, a precise measurement may nonetheless be possible. As a start, an experiment currently under construction at CERN proposes to measure the gravitational acceleration with a beam of  $\bar{H}$  atoms to a relative uncertainty of  $10^{-2}$  [27]. An alternate, novel approach proposed in Ref. [25] suggests that much colder  $\bar{H}$  for gravity experiments, in the 10-100  $\mu$ K range, might be produced by starting with sympathetically cooled positive antihydrogen ions (the bound state of one  $\bar{p}$  with two  $e^+$ ) in a Penning trap.

## 1.2 A Brief History of Antihydrogen Research

The current goals of low-energy antihydrogen research were proposed nearly twenty-five years ago [4]. Shortly after the first capture of low-energy antiprotons, it was sug-



gested that low-energy  $\bar{\text{H}}$  could be produced from  $\bar{\text{p}}$  and  $\text{e}^+$  confined in a Penning trap. Furthermore, Ref. [4] recognized that precise measurements of even a small number of  $\bar{\text{H}}$  would be possible if they were confined in a magnetic trap. Low-energy  $\bar{\text{H}}$  research that has grown from this initial vision is currently undertaken by four international collaborations at CERN's unique Antiproton Decelerator [28, 29, 30, 31].

This research program is made feasible by key developments that enable us to slow [32], trap [33], and electron-cool [34] antiprotons. Antiprotons are currently produced with GeV of energy and slowed to MeV within the Antiproton Decelerator storage ring, but antihydrogen must be produced at energies  $10^{11}$  times lower to be confined in a magnetic trap. Groundbreaking  $\bar{\text{p}}$  research made this plausible, demonstrating the first factor of  $10^8$  early on in  $\bar{\text{p}}$  clouds suitable for antihydrogen production [34] and presenting methods for further improvement [35]. Reference [36] is a relatively recent review of these techniques that are now used in all  $\bar{\text{H}}$  experiments.

Positrons have a relatively longer history in charged-particle traps, as they are readily available from radioactive sources. A variety of methods to provide  $\text{e}^+$  for  $\bar{\text{H}}$  experiments have been developed since the  $\bar{\text{H}}$  trapping was first proposed (reviewed in Ref. [19]). Current  $\bar{\text{H}}$  experiments accumulate  $\text{e}^+$  in apparatus in which fast  $\text{e}^+$ , originating from decays in  $^{22}\text{Na}$ , collisionally cool in a series of room-temperature Penning traps with progressively lower buffer-gas pressure [37].

While progress to produce and trap  $\bar{\text{H}}$  was underway, a proposal was made to look for  $\bar{\text{H}}$  formed by energetic  $\bar{\text{p}}$  binding to a  $\text{e}^+$  formed by pair production [38]. This led to an exciting result of 9 atoms detected [39], which was later confirmed by another laboratory with another 37 atoms [40]. While these experiments demonstrated the

existence of  $\bar{\text{H}}$  for the first time, the approach was not continued as it did not provide a means to precisely measure properties of the atoms.

Cold  $\bar{\text{H}}$  has now been synthesized by two methods that appear to be compatible with our goal of precise spectroscopy. Despite the opposite electric charge of  $\bar{\text{p}}$  and  $\text{e}^+$ , a nested-trap scheme allows for the interaction of  $\bar{\text{p}}$  and  $\text{e}^+$  that remain confined [41]. Shortly following the first co-trapping of  $\text{e}^+$  and  $\bar{\text{p}}$  [42] and observation of collisional cooling of  $\bar{\text{p}}$  by  $\text{e}^+$  [43], thousands of  $\bar{\text{H}}$  atoms were produced and detected by this approach [1, 2, 3]. In this method,  $\bar{\text{H}}$  is formed as a relatively low-density antiproton cloud passes through a positron plasma. The dominant formation mechanism at cryogenic temperatures appears to be three-body recombination, involving a collision of a  $\bar{\text{p}}$  and two  $\text{e}^+$  (the second  $\text{e}^+$  is required to conserve momentum and energy) [41].

The use of this nested-well scheme to load atoms into a magnetic trap depends on the velocity and internal state of the atoms that result from the complicated dynamics of the  $\bar{\text{p}}$  and  $\bar{\text{H}}$  within the  $\text{e}^+$  plasma. Although the distribution of  $\bar{\text{H}}$  produced is largely unknown (in particular for the slowest, most deeply-bound  $\bar{\text{H}}$ ), we should note a pair of novel experiments that are the only to directly measure the properties of some  $\bar{\text{H}}$  produced [3, 44]. In these experiments, two sequential Stark-ionizing regions were positioned near the nested Penning trap. The first region was varied in strength and duty cycle to filter atoms depending on their internal state and velocity, while the second region provided for counting transmitted atoms. Another very recent experiment reports the magnetic confinement of  $\bar{\text{H}}$  for 1000s, an important indirect demonstration that ground-state antihydrogen has been produced [45].

The second method used to form cold  $\bar{\text{H}}$  involves two charge-exchange reactions

[46]. First, Rydberg positronium is formed as a Rydberg Cs beam is directed through a positron plasma. Some of this positronium travels through nearby trapped  $\bar{p}$  and undergoes a second charge-exchange reaction to create  $\bar{H}$ . A first proof-of-principal demonstration detected 14  $\bar{H}$  atoms [47]. A focus of a Ref. [48], a very recent thesis, is scaling-up this initial experiment to produce useful amounts of trapped  $\bar{H}$ .

### 1.3 Overview of this Work

The research presented in this thesis was undertaken within the ATRAP collaboration from 2005 to 2011, and it has benefited greatly from close collaboration within this team as well as the achievements of previous members. In particular, the entire ATRAP apparatus and our standard trap techniques (Chapter 2) result from the contributions of many researchers. The author's contributions to these are varied: the design and construction of a robust upper vacuum and XY-stage bellows assembly with a compact window flange; the preliminary design of the antiproton-loading solenoid, Rydberg Cs apparatus, and an in-vacuum antiproton energy tuning foil; and the fabrication and installation of 1-K cooling lines, trap electrodes, wiring, and control electronics. For the initial studies in the Penning-Ioffe trap (Chapter 3), a central focus of a previous thesis [49], the author studied the consequences of the stability cut-off radius for antihydrogen production and created software to conveniently calculate and analyze the trap fields, which is now used widely in our collaboration. Furthermore, these studies contain the first antiproton experiments run by the author during brief visits to CERN. For the remaining studies presented (Chapters 4 through 8), the author has had a principle or co-principle role in designing, running,

and analyzing the experiments, which were undertaken at CERN over the previous two years. The second-generation Penning-Ioffe trap (Chapter 9) is a major apparatus development led by the author throughout his involvement with ATRAP. Design and construction of the new magnet system, including detailed collaboration with the manufacturer, was the sole responsibility of the author. Additionally, the author designed the modified cryostat for this apparatus and undertook much of its construction. Important contributions to all of these projects by collaborating researchers will be represented in other theses: oversight of the daily operation of the ATRAP apparatus [48]; running many antiproton experiments, design of centrifugal separation measurements, and construction of the second-generation Penning trap [50]; and the undertaking of positron loading experiments [51].

We begin in Chapter 2 by reviewing the apparatus and standard experimental methods for trapping antiprotons, positrons, and electrons that have been developed over the years. Chapter 3 then describes an initial search for trapped  $\bar{\text{H}}$ . The first demonstration of  $\bar{\text{H}}$  synthesis within a magnetic trap is followed by a test for captured  $\bar{\text{H}}$  atoms, in which a limit of fewer than 12 trapped atoms is established by our detector resolution. The following chapters set out to develop methods and apparatus to greatly increase this quantity.

Chapters 4 and 5 present techniques to measure the properties of trapped plasmas used to produce  $\bar{\text{H}}$ . In Chapter 4, we improve methods used to nondestructively determine the geometry, and thus density, of a plasma from its frequencies of internal oscillations. This diagnostic is then used to implement a rotating-wall technique, in which a rotating electric field is used to control the radius of plasmas. In Chapter 5 we

use two methods to measure the remaining key parameter of trapped plasmas: temperature. First,  $\bar{p}$  temperatures are determined by a direct measurement of the axial energy distribution. Then the temperatures of  $e^-$  and  $e^+$  plasmas are investigated by measuring a pressure-shift in their internal oscillation frequencies.

The following three chapters apply these trapped-plasma techniques to prepare plasmas that promise to greatly increase the achievable number of trapped  $\bar{H}$ . In Chapter 6 we study two methods to cool  $\bar{p}$ : sympathetic cooling by embedded electrons and cooling by adiabatic expansion. Used together, these produce plasmas of up to  $3 \times 10^6$   $\bar{p}$  at 3.5 K,  $10^3$  more  $\bar{p}$  and a 3-times lower temperature than previously realized for cryogenic  $\bar{p}$ . In Chapter 7, methods for improved particle accumulation are investigated, including use of the rotating-wall technique to avoid radial loss of particles. Accumulation of 10 million  $\bar{p}$  and 4 billion  $e^+$  is achieved with loading that is linear in time, improvements by factors of 14 and 20 over previous methods. Chapter 8 investigates centrifugal separation in electron-antiproton plasmas, a first for two-component plasmas that cannot be laser-cooled or optically imaged. The implications of centrifugal separation on trapped-antihydrogen experiments are discussed, including its effect on the geometry of  $\bar{p}$  plasmas and a novel method to remove electrons from electron-antiprotons plasmas.

Chapter 9 presents the second focus of this thesis: the design and construction of a second-generation Penning-Ioffe trap that provides improved performance and expanded capabilities for future antihydrogen experiments. A unique superconducting magnet design, made possible by emerging fabrication methods, generates octupole-Ioffe and quadrupole-Ioffe trap geometries. Thorough optimization of the magnet

---

windings results in an improved trap depth over our first-generation apparatus for both configurations. Potential detection of a single trapped atom is made possible by a rapid turn-off time. The second-generation Penning-Ioffe trap, along with its cryostat and substantial high-current circuitry, are now assembled at CERN, and the final preparations for its first use are underway.

## Chapter 2

# Apparatus and Standard Methods

In 2006, ATRAP commissioned a new apparatus to undertake antihydrogen trapping experiments for the first time [49]. At the heart of this apparatus is a combined Penning-Ioffe trap, an unusual trap geometry designed for the production and capture of antihydrogen atoms. The Penning trap provides confinement of the ingredients used to synthesize antihydrogen, antiprotons and positrons. Following now-standard methods that have been developed over the last twenty-five years, these particles are trapped, cooled, and manipulated to form cold antihydrogen. The Ioffe trap, a critical new addition, provides for the confinement of these neutral atoms. In this chapter, we describe the Penning-Ioffe trap and ancillary apparatus that is used throughout this thesis. Additionally, we'll introduce standard methods used to capture, move, and count charged particles in the Penning trap. These topics are reviewed thoroughly in two recent theses [49, 52].

Our antihydrogen apparatus is located within the Antiproton Decelerator (AD) at CERN. Figure 2.1 shows the experiment layout within the AD hall. The Penning-

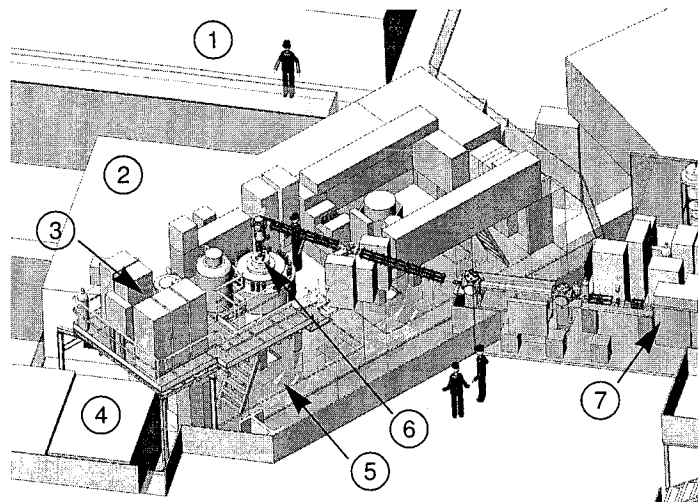


Figure 2.1: Layout of the ATRAP apparatus within the Antiproton Decelerator at CERN with the marked locations of the (1) control room, (2) laser Faraday cage, (3) equipment platform, (4) Penning-trap Faraday cage, (5) antiproton beam line, (6) Penning-Ioffe trap, and (7) positron source.

Ioffe trap receives antiprotons from the AD beam line and positrons from the ATRAP positron accumulator via a magnetic guide. As a consequence of the limited AD real estate, the positron accumulator is located in a zone separated from the Penning-Ioffe trap by approximately 10 m. Equipment for the Penning-Ioffe trap cryostat, detectors, and superconducting magnets are located on and near the adjacent platform. The Penning trap electronics are located in a Faraday cage with a shield extending to the trap feedthroughs. A second, larger Faraday cage contains lasers used in Rydberg Cs charge-exchange experiments and will house the lasers in development for the cooling and spectroscopy of antihydrogen. The control room allows for remote control of the antihydrogen apparatus.



## 2.1 Penning-Ioffe Trap

Our cryogenic Penning-Ioffe trap is shown in Fig. 2.2. The cryostat sits within the room-temperature bore of a superconducting solenoid that produces a uniform magnetic field of up to 3 T over the length of the Penning trap. Thermal insulation from this primary solenoid is provided by a thin three-layer insert that is cooled by a pulse-tube cryocooler. This insert absorbs the radiated heat from the solenoid bore, and acts as a vacuum enclosure within which the cryostat is suspended.

All feedthroughs (electrical, mechanical, and optical), as well as access to the cryogen and vacuum spaces of the cryostat, are located at the top plate, commonly referred to as the hat. Beneath the hat hang radiation baffles and a reservoir for liquid helium. A full reservoir, approximately 40 L, typically provides for one to two days of operation. The liquid helium space continues below to two superconducting magnets: a Ioffe trap and an antiproton-loading solenoid. Following a standard cryogenics method, a second, smaller volume of liquid helium, referred to as a 1-K pot, is connected to the main reservoir with poor conductance. This 1-K pot is kept at pressure of approximately 100 Torr through a dedicated pumping line, and the resulting equilibrium temperature is just above 1 K. Details about this pumped helium system are published in Ref. [53].

A separate vacuum enclosure surrounds the inner bore of the experiment, the space in which particles are trapped. Above the cryostat, this space connects to a room-temperature, ultra-high vacuum positron transfer line. Below the liquid helium reservoir, a 1.5 mm diameter, 13 mm long aperture located on the window flange reduces the conductance to the improved vacuum of the cryogenic trap region. This

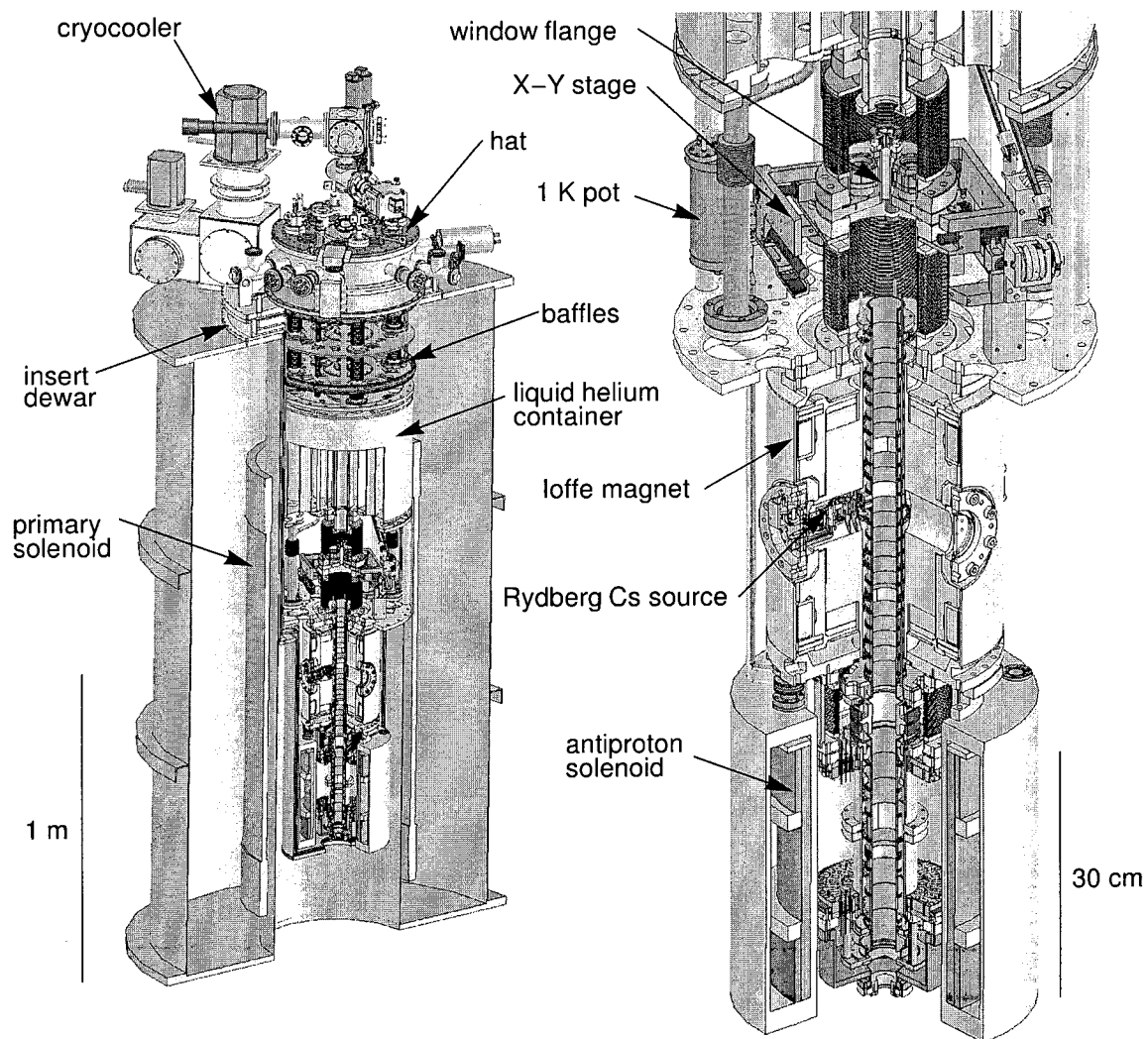


Figure 2.2: The entire cryogenic Penning-Ioffe trap (left) and a closer look at the trap region (right).

small aperture provides access to inject the trap with low-energy positrons. Other devices may be centered on the trap axis by an X-Y translation stage which moves the window flange. The current flange includes a large-diameter ultraviolet window, a photoelectron-loading gold foil, and a phosphor imaging screen, while the addition of a microwave horn is being pursued.

The trap region contains a stack of 39 cylindrical electrodes which generate the electric potentials of the Penning trap (Fig. 2.3). Each electrode is connected to low and high frequency signal leads which are joined with filters mounted on the lower vacuum enclosure. A full wiring diagram is shown in Ref. [52]. The trap electrodes, lower enclosure, and electrical feedthroughs in Fig. 2.3 are all connected to the 1-K pot with superfluid-helium cooling lines, resulting in a typical operating temperature of 1.3 K. This structure is isolated from the 4.2-K Ioffe trap, which encloses the upper trap region, by insulating edge-welded bellows and support rods.

### 2.1.1 Penning Trap

An ideal Penning trap consists of a quadrupole electric potential  $\phi \propto z^2 - \rho^2/2$  and uniform axial magnetic field  $\vec{B} = B_0 \hat{z}$ . The electric potential provides axial confinement (along  $\hat{z}$ ) of either positively or negatively charged particles, while the magnetic field provides for radial confinement.

Within our apparatus, a trap potential may be generated anywhere along the stack of electrodes shown in Fig. 2.3. For example, the potential produced by applying 100 V to a single radius-length electrode (e.g. UTR3) with respect to the others is shown in Fig. 2.4a-b. Near the trap center, the generated potential (solid line) is well

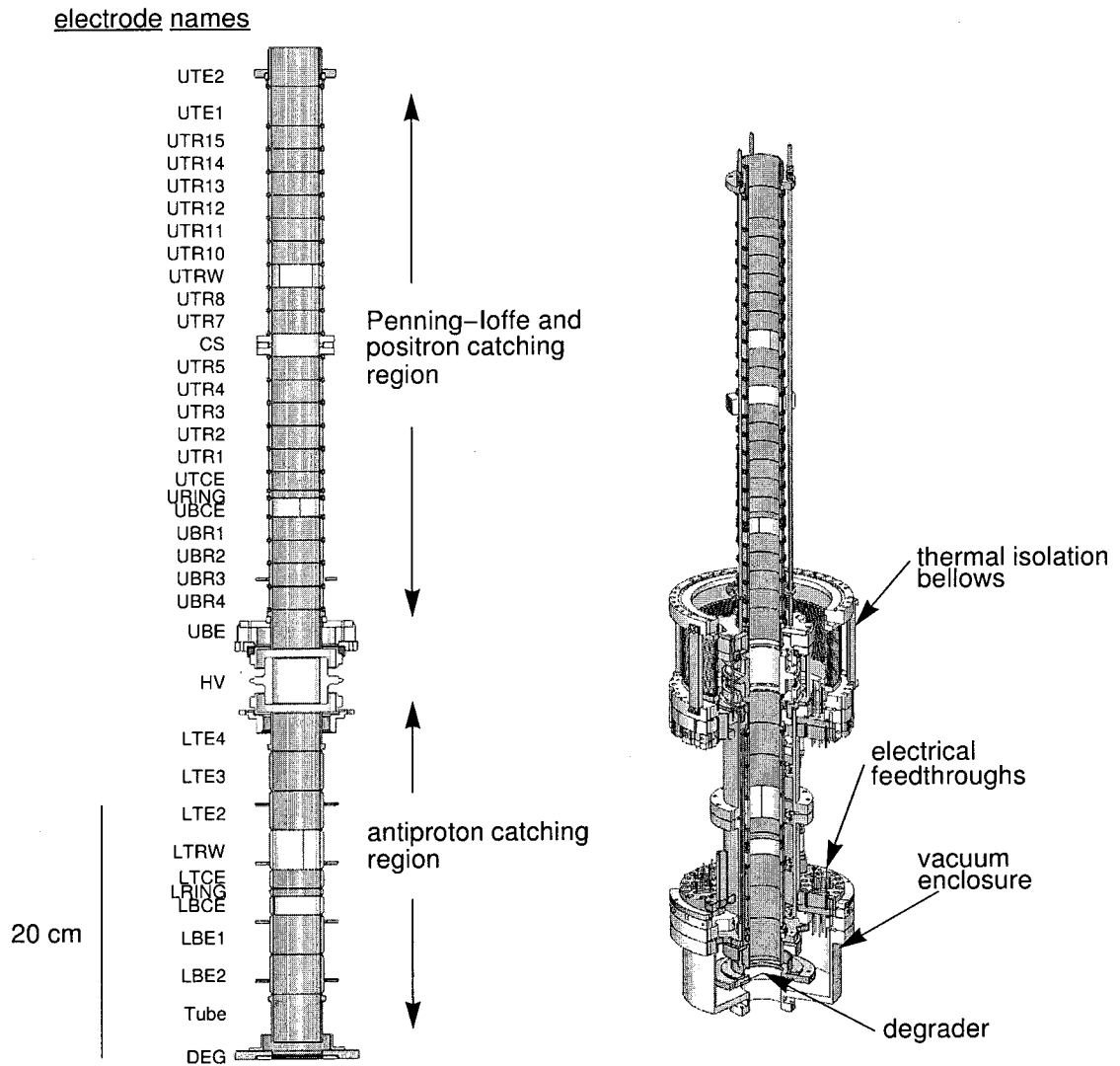


Figure 2.3: The stack of cylindrical electrodes that comprise the Penning trap.

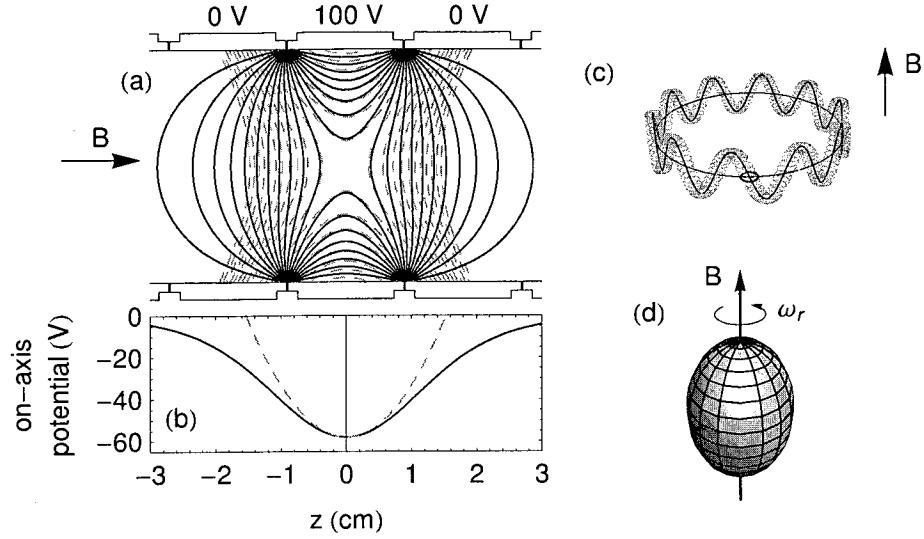


Figure 2.4: (a) Electrostatic equipotentials generated by applying 100 V to the central radius-length electrode shown. The trap potential (solid), shown at 10 V spacings, is well-approximated by a quadratic potential (dashed) near the trap center. (b) The corresponding on-axis potentials. (c) A single-particle trajectory and (d) a spheroidal plasma of charge particles in a Penning trap.

approximated by a quadrupole potential (dashed line). The degree to which a trap minimum is approximated by a quadrupole potential can be improved by a judicious choice of electrode lengths and voltages. Our stack of many electrodes has regions to generate highly harmonic trap potentials (e.g. LTCE to LBCE), which have been used for single-particle studies [52], as well as a region of short, identical electrodes (UBR3 to UTR15) which provide flexibility to design complex potential structures for antihydrogen experiments. Design of the electrode stack is discussed in Ref. [52].

A single charged particle in a Penning trap undergoes three harmonic motions, illustrated in Fig. 2.4c: a rapid cyclotron orbit, an axial oscillation, and a slow  $\vec{E} \times \vec{B}$  magnetron orbit [54]. In our experiments, the interaction between particles substantially alters the latter of these two motions. In particular, we'll typically work

with plasmas of charged particles within which the axial electric fields are completely screened out. In this case, the single-particle axial oscillation is replaced by an axial thermal motion, confined by a strong electric field at the ends of the plasma. Additionally, the space-charge electric fields increase the frequency of the  $\vec{E} \times \vec{B}$  orbit. The equilibrium distribution of plasma in a Penning trap, illustrated in Fig. 2.4d, is a uniform density spheroid that undergoes shear-free rotation about the  $z$ -axis [55]. The properties of these trapped plasmas are discussed in Chapter 4.

### 2.1.2 Ioffe Trap

A magnetic trap confines neutral atoms with a magnetic moment  $\vec{\mu}$  anti-parallel to the local magnetic field  $\vec{B}$ , i.e.  $\vec{\mu} \cdot \vec{B} < 0$ . For these so-called low-field-seeking atoms, the trap potential  $U = -\vec{\mu} \cdot \vec{B}$  is confining about a magnetic field minimum. We define the trap depth as the difference in the trap potential on the maximum equipotential surface that exists within the electrode inner surfaces and that of the local minimum it surrounds. We will typically specify trap depths in terms of low-field-seeking anti-hydrogen with the lowest principle quantum number, for which a magnetic moment of approximately one Bohr magneton  $\mu_B$  results in the trap potential  $U = \mu_B |\vec{B}|$ . The substantial challenge of trapping atoms is apparent in that a large field differential of 1 T results in a confining potential (in temperature units) of only 700 mK.

We use a Ioffe-type magnetic trap [56], which is a geometry potentially compatible with the axial field of the Penning trap (charged-particle confinement in this non-uniform magnetic field is discussed in Section 3.1). Radial confinement in a multipole-Ioffe trap is provided by a transverse multipole coil of order  $n$  which generates a

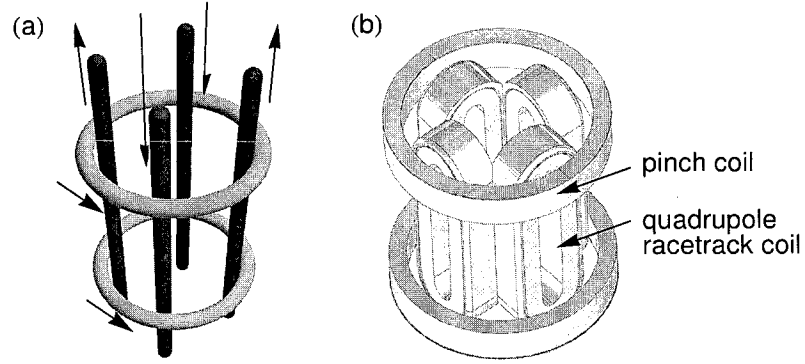


Figure 2.5: (a) Schematic of the Ioffe trap coils with current directions labeled and (b) the actual coil geometries.

magnetic field

$$\vec{B}(\rho, \phi) = B_r \left( \frac{\rho}{R_e} \right)^{n-1} \left( \cos(n\phi) \hat{\rho} - \sin(n\phi) \hat{\phi} \right) \quad (2.1)$$

where we specify the field strength by its magnitude  $B_r$  at the electrode inner radius  $R_e$ . The corresponding trap potential for low-field-seeking ground-state antihydrogen is thus

$$U(\rho) = \mu_B B_r \left( \frac{\rho}{R_e} \right)^{n-1} \quad (2.2)$$

A standard quadrupole-Ioffe magnet, for which  $n = 2$ , generates a trap potential linear in radius,  $U_{\text{quad}} \propto \rho$ . For the octupole-Ioffe magnet described in Chapter 9,  $n = 4$  and  $U_{\text{oct}} \propto \rho^3$ .

Axial confinement in a Ioffe trap is provided by two solenoidal coils, referred to as pinch coils, that increase the axial magnetic field at the ends of the trap. In practice the radial gradient caused by these coils near the trap center is too small to significantly alter the radial trapping fields described in Eq. 2.1. It should be noted that an additional axial field of 1 T from the primary Penning-trap solenoid is present throughout this thesis when the Ioffe trap is used.

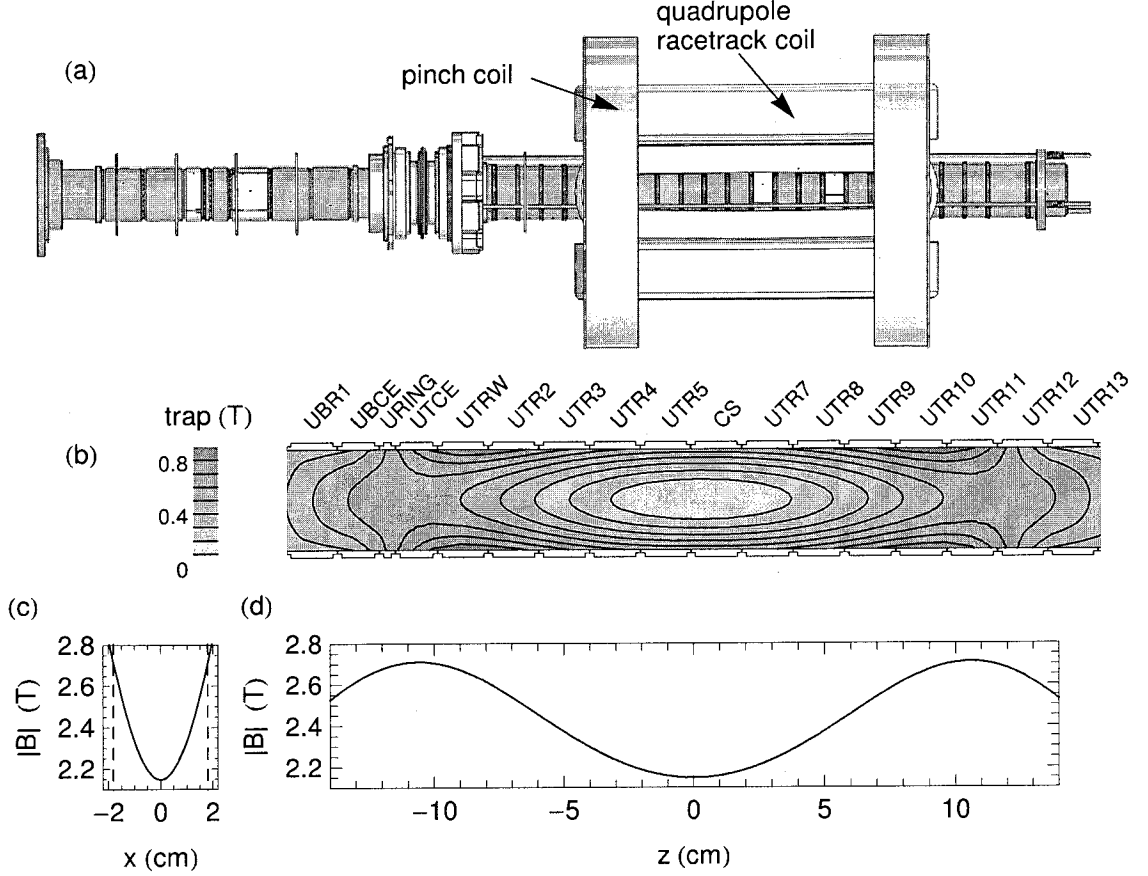


Figure 2.6: (a) The Ioffe trap coils positioned outside of the upper electrodes generate (b) trap contours shown within a cross-section of the electrodes. The magnetic field magnitude, including a uniform 1-T axial Penning-trap field, is shown (c) transverse to the trap axis at the axial center and (d) along the trap axis.

The coils of the quadrupole-Ioffe trap used in this thesis are shown in Fig. 2.5. A full trap is created when 80 A are supplied to each pinch coil and 68 A to the four race-track coils, which are connected in series. The resulting magnetic field superimposed with 1 T from the Penning trap solenoid provides a trap depth of 0.56 T (Fig. 2.6), corresponding to 380 mK for ground-state antihydrogen.

A radial port runs through the center of each racetrack coil providing access to



the trap center (as seen in Fig. 2.2). These ports currently house a Rydberg Cs beam source used for charge-exchange experiments [48] and a small resistive heater used to induce a quench to rapidly discharge the magnet (used in Section 3.3). For future experiments with trapped antihydrogen, this access is foreseen to be critical for efficient use of ultraviolet laser light.

## 2.2 Particle Loading

In this thesis, we undertake experiments with three types of trapped particles: electrons, antiprotons, and positrons. An overview of the method used to load each of these into the Penning trap is discussed below, while further details are provided in Refs. [49, 52].

### 2.2.1 Electron Loading

Electrons are injected into the trap via the photoelectric effect [57]. An 18-mJ, 10-ns pulse of 248-nm light from an excimer laser (GAM Laser EX5/250) is directed down the trap axis from above the hat, travels through the window flange aperture, and strikes the beryllium foil below the electrode stack. The 5.0-eV photons have sufficient energy to eject electrons, which are guided by the magnetic field and accelerated by the electrode potentials towards the trap.

The resulting pulse of electrons is caught in-flight by the electric potentials shown in Fig. 2.7a. A blocking potential on electrode LBE1 is lifted for  $2\mu\text{s}$  to accept the pulse originating from the foil, DEG. The electrons are then trapped between electrodes LBE1 and LTE3 and cool until they are confined within electrode LTE2.

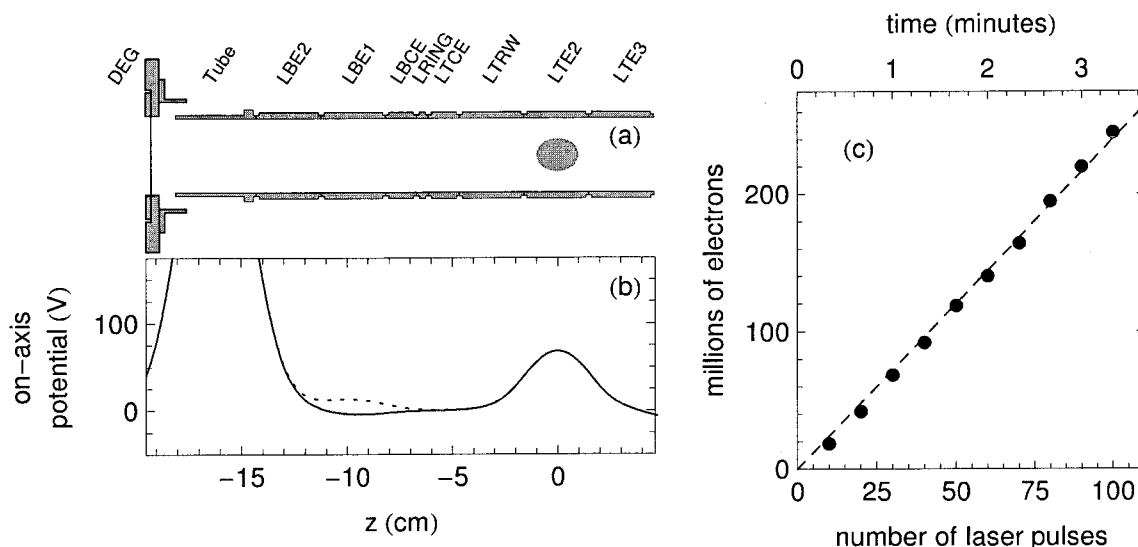


Figure 2.7: (a) An electron plasma located within a cross-section of the trap electrodes. (b) In the electron loading procedure, the on-axis potential (solid) is briefly lowered (dashed) to accept a pulse of photo-electrons originating from the foil DEG. (c) Electrons may continue to be loaded from additional laser pulses.

The cooling occurs by synchrotron radiation from the cyclotron motion while collisions thermalize the cyclotron and axial motions.

This loading procedure can be repeated to stack multiple injections of electrons. A laser repetition rate of 0.5 Hz and load rate of  $2.5 \times 10^6$  electrons per pulse, results in  $7.5 \times 10^7$  electrons loaded per minute. Linear loading of 250 million electrons in just over 3 min is shown in Fig. 2.7c. Our photo-electron loading method is described in detail in Ref. [57].

## 2.2.2 Antiproton Loading

Antiprotons are injected into the trap from the Antiproton Decelerator (Fig. 2.8) in bunches of approximately 30 million particles every 110 seconds. These 5.3-MeV

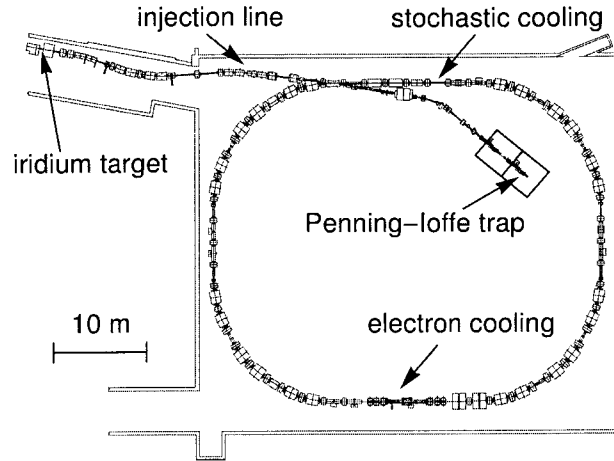


Figure 2.8: Location of the ATRAP Penning-Ioffe trap within the Antiproton Decelerator ring.

antiprotons lose most of their energy as they pass through the 125-  $\mu\text{m}$ -thick beryllium degrader. As in electron loading, the antiprotons are then caught in-flight with a pulsed potential. Since the synchrotron radiation rate for the antiprotons is much too long, however, they do not cool on their own. Instead, electrons are first loaded to cool the antiprotons via collisions. The achieved cooling rate is sufficient for the stacking of sequential antiproton injections.

The methods used to slow [32], catch [33], electron-cool [34], and stack [36] antiprotons in the apparatus used in this thesis are reviewed in Ref. [49]. In Chapter 7, improvements are discussed that lead to the accumulation of 10.5 million antiprotons from 50 injections. The observed linear accumulation at an efficiency of  $6 \times 10^{-3}$  results in a loading rate of  $1.2 \times 10^5$  antiprotons per minute.

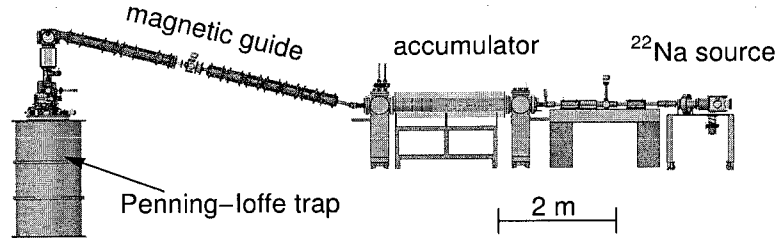


Figure 2.9: Positrons from a  $^{22}\text{Na}$  source are continuously accumulated in a separate room-temperature Penning trap and occasionally transferred to the Penning-Ioffe along a magnetic guide.

### 2.2.3 Positron Loading

The positron source used in this work, based on the apparatus presented in Ref. [37], is the primary responsibility of the ATRAP team from York University. Positrons emitted by the radioactive decay of a  $^{22}\text{Na}$  source first slow in a frozen neon moderator. Subsequent collisional cooling occurs in a series of room-temperature Penning traps with a progressively lower pressure of a buffer gas of nitrogen. After a typical accumulation time of 30-50 seconds, the positrons are injected into the cryogenic Penning-Ioffe trap via a long magnetic transfer guide (Fig. 2.9). This magnetic guide contains nearly one hundred independent coils to steer the positrons to the central axis of the Penning-Ioffe trap. The large magnetic field of the Penning-Ioffe trap then serves to radially compress the positron bunch and guide it through the small aperture on the window flange (Fig. 2.2). As in the other loading methods, the positrons are caught in-flight with a pulsed potential in the cryogenic Penning trap.

The accumulation and transfer of positrons is described in further detail in Ref. [49]. An improvement to this procedure in Chapter 7 is the use of the rotating-wall technique to compress the positron plasma as multiple positron transfers are stacked. With this technique, we demonstrate the loading of 4 billion positrons at a constant

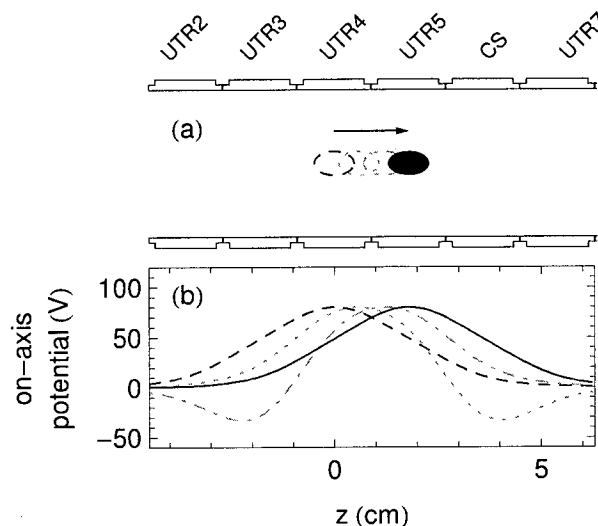


Figure 2.10: (a) An electron plasma is transferred from its position within electrode UTR4 (dashed) to UTR5 (solid) by continuously adjusting the (b) trap potentials with the voltages of electrodes UTR3 through CS.

rate of  $8 \times 10^5$  positrons per second, corresponding to an efficiency of approximately  $1 \times 10^{-3}$  per radioactive decay.

## 2.3 Particle Transfer and Detection

In this final section, we review the standard techniques to move and count trapped particles that are used throughout this thesis.

### 2.3.1 Particle Transfer

Moving trapped particles from one region of the Penning-Ioffe trap to another is often desired. In the antihydrogen experiments of Chapter 3, for example, antiprotons and positrons are simultaneously loaded in separate regions of the trap and then moved to adjacent potential wells for the atom formation procedure. To achieve this,

trap wells are smoothly translated along the stack of electrodes. Figure 2.10 shows the trap potential at four times during such a translation. In this case, four electrodes are used to maintain a constant quadratic component of the potential during the transfer from a well centered on electrode UTR4 to an identical well on electrode UTR5. The move procedure is adiabatic since the changes in electrode voltages occur over many milliseconds, a time much longer than the timescale for relevant particle oscillations. This smooth many-electrode translation will be described further in a future thesis [50] and is compared to a previous two-electrode approach in Ref. [48].

### 2.3.2 Charge Counting

The number of trapped electrons or positrons can be determined by ejecting the particles out of the trap and collecting them on the degrader foil, which serves as a Faraday cup electrode. A charge-sensitive preamplifier connected to the degrader produces an output voltage proportional to the net charge deposited and an absolute calibration is determined with test pulses of known charge [58]. Care must be taken to bias the degrader voltage to prevent the emission of secondary charges, which would change the net charge deposited and cause counting inaccuracy. As has been previously discussed [49], this problem is well understood for electrons. The situation for positrons is more complicated, since annihilations can cause processes such as the ejection of high-energy Auger electrons, however it is found that appropriate blocking voltages result in accurate counting [49].

The counting procedure for a typical electron plasma is shown in Fig. 2.11. The plasma is held in a well centered on electrode LTE3. A pulsed voltage on electrode

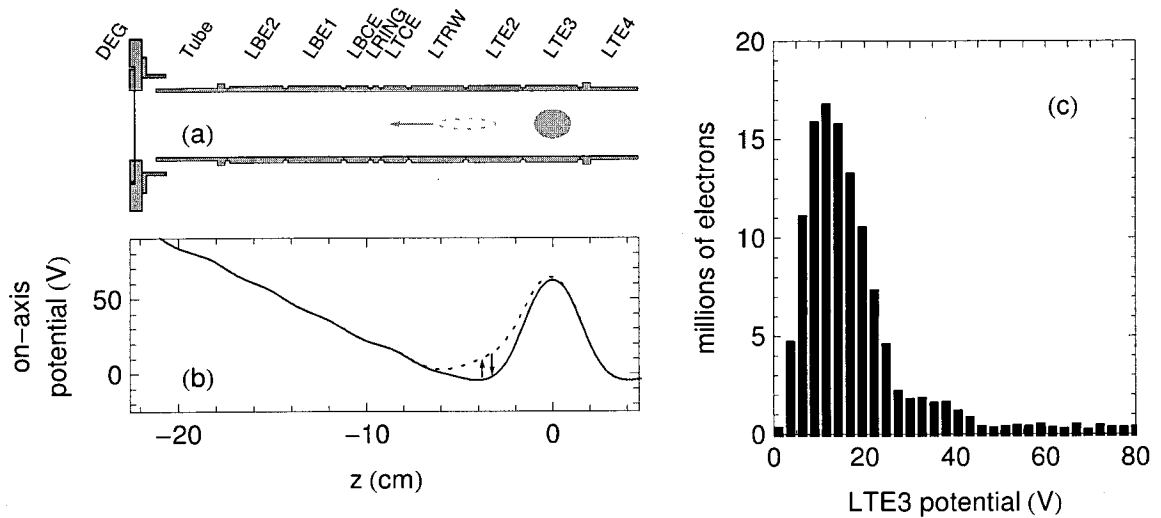


Figure 2.11: (a) Electron plasma location and (b) on-axis trap potentials during the charge-counting procedure. Electrons that escape when the potentials (solid) are briefly lowered (dashed) are counted. (c) Repeating this process as the voltage applied to electrode LTE3 is decreased allows all of the particles to be ejected and counted.

LTE2 reduces one side of the well, and electrons that are ejected accelerate to the degrader DEG. To prevent saturation of the preamplifier, the ejection procedure is repeated in small steps while the voltage on electrode LTE3 is reduced. The charge count for each step is shown in Fig. 2.11c for a total of  $190 \pm 10$  million electrons. The typical error of 5 to 10% is acceptable for the measurements in this thesis, but it should be mentioned that this uncertainty may likely be reduced with careful calibration and optimal choice of pulse amplitudes.

### 2.3.3 Antiproton Annihilation Detection

To count antiprotons, they are ejected from the trap and the resulting annihilation products are detected. The annihilation of an antiproton and proton produces on

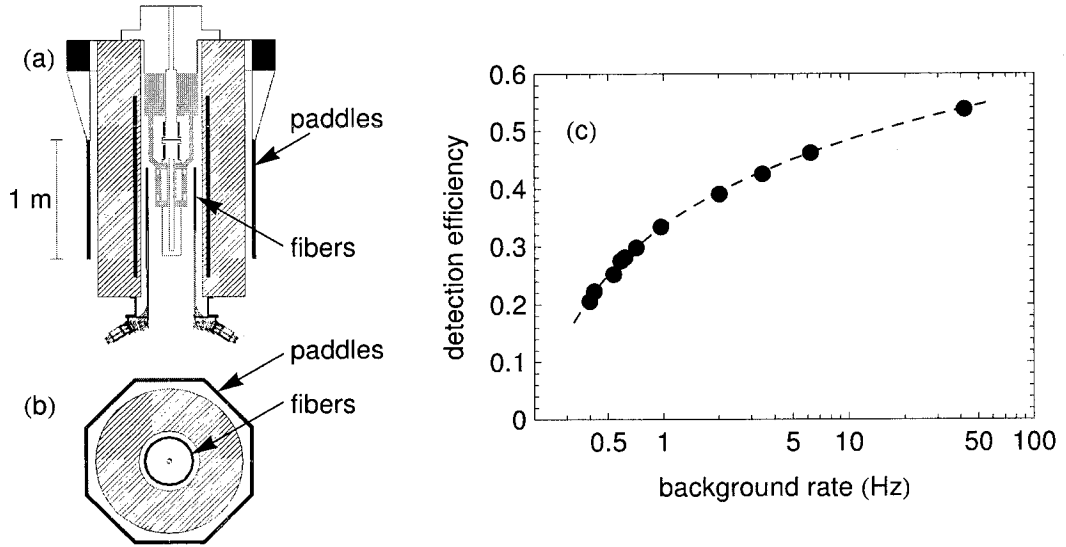


Figure 2.12: (a) Side and (b) cross-section views of the ATRAP annihilation detector geometry. (c) Annihilation detection efficiency as a function of background rate for various detector cuts.

average 3.0 charged pions [59], and these products are observed as they pass through nearby scintillating detectors (Fig. 2.12). This detector system is the primary responsibility of the ATRAP team from Forschungszentrum Jülich. The first detector group, located between the cryostat and large solenoid, consists of 448 straight and 336 helical 3.8-mm diameter optical fibers. The second detector group is comprised of 16 inner-layer and 8 outer-layer large-area plastic paddles. Each detector is coupled to a photomultiplier tube which detects luminescence caused by the interaction of the scintillating material with the high-energy charged pions.

Annihilation detection achieves a high signal-to-noise by discriminating between antiproton annihilations that typically produce multiple ionizing particles and background events from single cosmic rays. To do so, detection events are conditioned on signals arising from multiple detectors in a geometry that is unlikely to be triggered



by a cosmic ray. This approach is limited primarily by the solid angle subtended by the scintillators, which restricts the pion detection efficiency. More stringent detection conditions result in fewer counts from antiproton annihilations as well as cosmic rays. This trade-off between antiproton detection efficiency and background rate is shown by the range of cuts in Fig. 2.12c, which are developed in Ref. [48].

For the detection of a few trapped antihydrogen atoms (investigated in Chapter 3), the signal-to-noise for annihilation detection is critical. In these experiments, the data from each detector is recorded so that event determination can be made afterwards in software. For typical antiproton counting throughout this thesis, however, the full detection record is unnecessary and would generate an unwieldy amount of data. Instead, hardware coincidence logic and counters are used. The typical cut used throughout this thesis is a coincidence of at least one each of the straight fibers, helical fibers, inner paddles, and outer paddles. For annihilations of antiprotons ejected to the degrader foil, this cut results in antiproton detection efficiency of 48% and a background rate of 30 Hz. This detection efficiency was determined by Monte Carlo simulation [60], and further discussion of the detector geometry and cuts can be found in Refs. [49, 48].

## Chapter 3

# Search for Trapped Antihydrogen

Antihydrogen ( $\bar{\text{H}}$ ) has now been synthesized by two methods [19] that appear compatible with our long-term goal of the precise spectroscopy of trapped  $\bar{\text{H}}$  [4]. In this chapter, we take the next step toward this goal: a Ioffe trap to confine neutral atoms is superimposed on a Penning trap used to produce  $\bar{\text{H}}$  for the first time. The primary challenge of this combined Penning-Ioffe trap is that the addition of the magnetic field gradients required to trap low-field-seeking  $\bar{\text{H}}$  atoms ruins the cylindrical symmetry that guarantees stable confinement of charged particles in a Penning trap [61, 62]. We nonetheless demonstrate confinement of  $\bar{\text{p}}$  and  $\text{e}^-$  (a temporary substitute for  $\text{e}^+$ ) that appears to be sufficient for typical  $\bar{\text{H}}$  formation methods [5]. We proceed by demonstrating  $\bar{\text{H}}$  synthesis in the combined Penning-Ioffe trap [6]. The chapter concludes with search for trapped  $\bar{\text{H}}$ , in which a limit of fewer than 12 captured atoms is set by the annihilation detection sensitivity. The experiments presented here have been published in Refs. [5, 6] and are the principle focus of a previous thesis [49].

### 3.1 Charged Particles Confined in a Penning-Ioffe Trap

We begin by investigating the confinement of charged particles in a Penning trap when the magnetic field of a Ioffe trap is added. As introduced in Section 2.1, a Penning trap consists of a uniform magnetic field  $B_0\hat{z}$  and a quadrupole electric potential  $\phi_t \propto z^2 - \rho^2/2$ . The axial confinement of charged particles is provided by  $\phi_t$ , and radial confinement is a consequence of the conservation of angular momentum about the trap axis,  $P_\theta$ . As discussed further in Section 4.1, to a good approximation  $P_\theta \propto B_0\langle\rho^2\rangle$ , providing a constraint on the mean square radius of trapped particles.

With the addition of the radial-trapping field of a quadrupole Ioffe trap, cylindrical symmetry of the trap fields (and thus conservation of  $P_\theta$ ) is lost, and charged-particle confinement is no longer guaranteed. The magnetic field of the Penning-Ioffe trap is approximately  $\vec{B} = B_0\hat{z} + \beta(x\hat{x} - y\hat{y})$  where  $\beta$  specifies the strength of the magnetic trap gradient and we have neglected the axially-symmetric gradient from the pinch coils. This field is illustrated in Fig. 3.1a, where field lines that extend from a circle form the shape of a twisted bow tie. Traveling in the  $\hat{z}$ -direction, field lines diverge maximally in the  $x$ - $z$  plane. In this case, a line that starts at a position  $x_0$  bends outwards to  $x(z) = x_0 \exp(\beta z/B_0)$ . Some representative maximally divergent field lines are illustrated in Fig. 3.1b.

The first theoretical study of charged-particle confinement in a Penning-Ioffe trap, presented in Ref. [61] investigated single-particle trajectories. For small radii  $\rho$ , where the quadrupole-Ioffe field is much smaller than the axial field,  $\beta\rho \ll B_0$ , stable

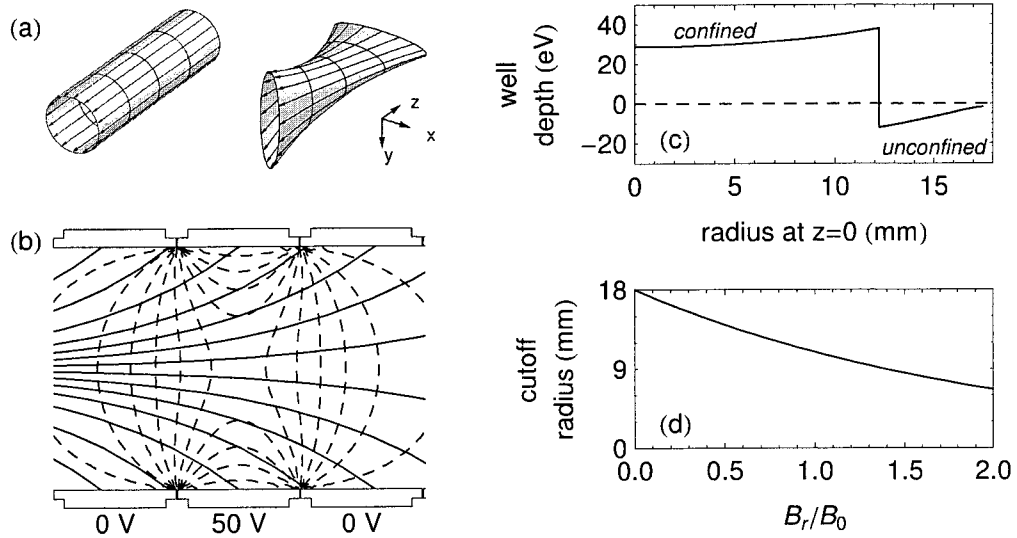


Figure 3.1: (a) Representative magnetic field lines of the Penning trap (left) and Penning-Ioffe trap (right). (b) Representative magnetic field lines for  $B_r/B_0 = 0.8$  (solid) and electrostatic equipotentials in 5 V intervals (dashed) within of a Penning-Ioffe trap shown inside of a cross-section of the trap electrodes. (c) Electrostatic well depth along the field lines shown in part b originating from the axial center of the trap at the specified radius. Field lines beyond the apparent cutoff radius  $\rho = 12$  mm are no longer confining. (d) Cutoff radius as a function of the relative quadrupole field strength,  $B_r/B_0$ . Adapted from Ref. [6].

trajectories are found by associating adiabatic invariants with each of the three well-known Penning-trap orbits [63], the shapes and frequencies of which are modified due to the Ioffe field. Even though stable single-particle trajectories exist, this report brings up two potential challenges to confining many particles, as is desired for  $\bar{\text{H}}$  experiments. First, a maximum possible radius in a stable orbit is given  $\rho_{\text{max}} = B_0/\beta$ . At  $\rho_{\text{max}}$ , the radius at which the Ioffe field strength is equal to the axial field strength, the electric potential is no longer confining along the maximally divergent magnetic field lines. Second, unstable trajectories exist for narrow resonances corresponding to certain integer ratios of trap frequencies. For example, a particle trajectory that

rotates about the trap axis (an  $\vec{E} \times \vec{B}$  drift) at twice the frequency of its oscillation parallel to the magnetic field will rapidly increase its position beyond stable radii. Furthermore, increasing the particle density can introduce collisions and space-charge fields that broaden resonances [61]. Therefore we expect the addition of the Ioffe trap fields will cause an initial immediate loss of particles at large radii followed by possible continuous loss as particles gradually increase their radial position.

Before moving on to experimental tests of these potential limitations, we should note that since the trap electric potential differs substantially from an ideal quadrupole at large radii, the actual maximum stable radius differs from  $\rho_{\max}$ . This cutoff radius in a realistic trap generated by finite-length electrodes has a simple explanation, illustrated in Fig. 3.1b-d. Consider the electrostatic well depth of a particle traveling along each magnetic field line shown. Each line that terminates to the right at a grounded electrode has a well depth equal to the magnitude of the potential at the axial center of the trap. A line that starts at a large enough radius, on the other hand, terminates at the central electrode and provides no confinement. Figure 3.1c shows the effective well depth along field lines that start at the specified radius, with a sharp transition from confined to unconfined occurring at the effective cutoff radius. In Fig. 3.1d, the cutoff radius is shown as a function of magnetic field strength parameterized by the ratio  $B_r/B_0$ , where  $B_r$  is the quadrupole field at the electrode inner radius  $R_e = 18$  mm, i.e.  $B_r = \beta R_e$ .

We begin experiments by loading either  $9 \times 10^4$  or  $2.8 \times 10^5$   $\bar{p}$  in a uniform magnetic field ( $B_0 = 1$  T,  $\beta = 0$ ) in a Penning-trap well centered in the Ioffe trap (methods in Section 2.2.2). Briefly,  $4 \times 10^8$   $e^-$  are used to stack  $\bar{p}$  from 3 or 10 consecutive  $\bar{p}$

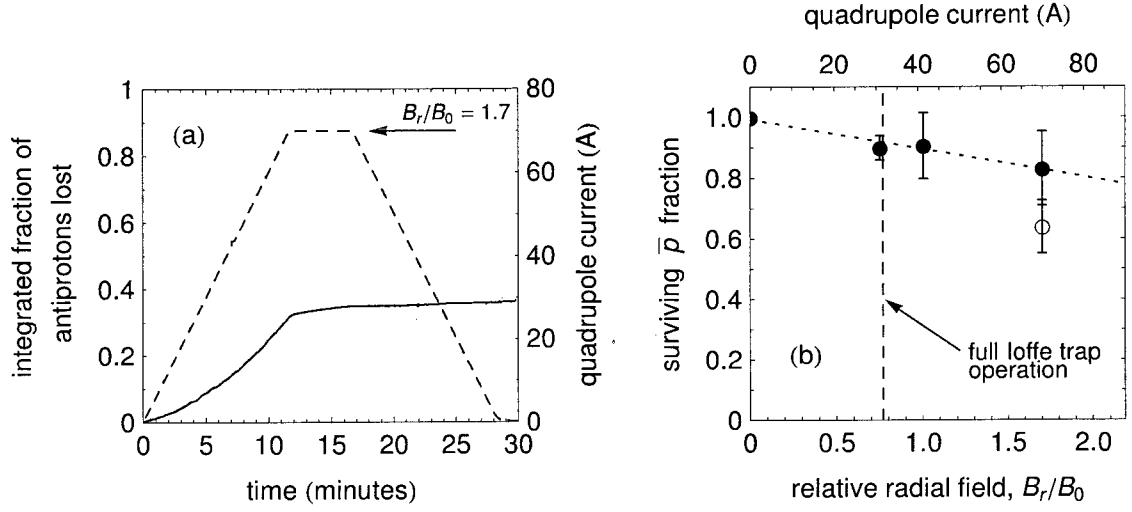


Figure 3.2: (a) Integrated fractional loss (solid) for  $2.5 \times 10^5$   $\bar{p}$  as the quadrupole current (dashed) is increased to generate a relative peak field of  $B_r/B_0 = 1.7$ , held for 300s, and returned to 0. (b) Total fraction remaining in trials of  $9 \times 10^4$  (filled) and  $2.5 \times 10^5$  (open)  $\bar{p}$  with the relative peak field  $B_r/B_0$  specified. Adapted from Ref. [6].

injections. After the  $e^-$  are removed by pulsed ejection, the  $\bar{p}$  are transferred to a well created by applying 50 V to a standard radius-length electrode in the position of electrode CS (shown in Fig. 2.2).

Figure 3.2a shows the fraction of  $2.8 \times 10^5$   $\bar{p}$  lost as the Ioffe quadrupole coil is increased to 69 A (corresponding to  $B_r/B_0 = 1.7$ ) at 0.1 A/s, held for 300s, and returned to 0 A (the corresponding field strength is discussed below). Antiproton loss is determined by annihilation detection (Section 2.3.3). The  $\bar{p}$  loss rate increases until the maximum field is reached, after which losses are marginal. This observation is consistent with the immediate loss of particles beyond a maximum stable radius and little continuous expansion and loss due to multi-particle effects.

Figure 3.2b shows the fraction of  $9 \times 10^4$  and  $2.8 \times 10^5$   $\bar{p}$  that survive this procedure for various maximal magnetic fields. Note that this test has been undertaken without

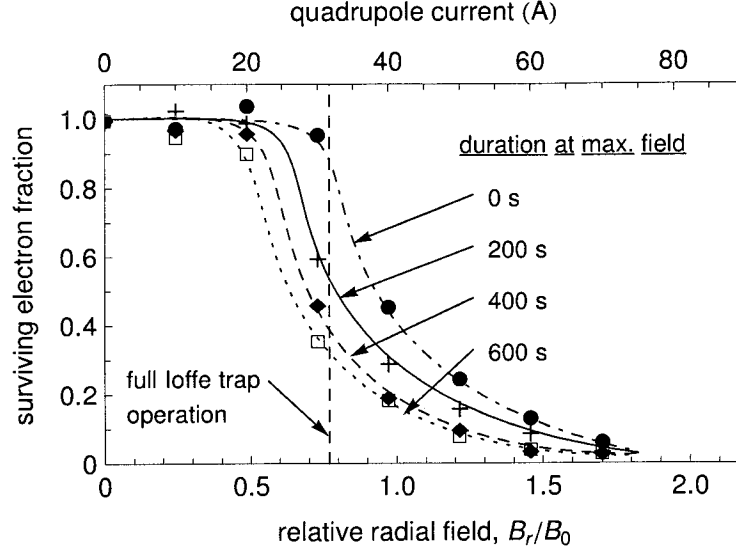


Figure 3.3: Fraction of  $e^-$  remaining after the radial trap field is increased to the relative field strength  $B_r/B_0$ , held 0 to 600 s as specified, and returned to  $B_r = 0$ . Smooth curves are added to guide the eye. Adapted from Ref. [6].

the solenoidal pinch coils that provide axial confinement (see Fig. 2.5), since this allows us to probe larger relative field strengths  $B_r/B_0$ . When the full Ioffe trap is energized, the pinch coils increase  $B_0$  to 2.1 T, resulting in  $B_r/B_0 = 0.78$ . We conclude from these studies that  $\bar{p}$  confinement appears sufficient for  $\bar{H}$  production.

For the second ingredient required to make  $\bar{H}$ , Fig. 3.3 shows an analogous measurement undertaken with  $e^-$ , as a convenient substitute for  $e^+$ . In this study,  $4 \times 10^7$   $e^-$  were used. The first particle loss is observed for  $B_r/B_0 \approx 0.5$ , corresponding to an initial maximum electron radius of approximately 14 mm inferred from the cutoff radius. In contrast to the  $\bar{p}$  study, appreciable constant-field loss is observed in these trials. Without sophisticated models of this loss it is not feasible to differentiate the immediate and continuous loss mechanisms from these data, since the magnetic field changes occur over a relatively long time scale. Nonetheless, it is apparent that

confinement is sufficient for  $\bar{\text{H}}$  formation with procedures that take on the order of 100s.

Here we have only presented a proof-of-concept demonstration of stability in a Penning-Ioffe trap. While further results are presented in Ref. [49], detailed studies, enabled by the plasma diagnostics developed in Chapters 4 and 5, are left for future study if they become necessary to optimize  $\bar{\text{H}}$  experiments.

Our measurements were preceded by a series of experiments that prompted a much different outlook for the prospects of the Penning-Ioffe trap [62, 64]. In a study closely related to ours, loss of roughly 80% of  $\text{e}^-$  within 20s at  $B_r/B_0 = 0.8$  led the authors to conclude that antihydrogen could not be produced within a substantial quadrupole-Ioffe trap [64]. In their experiment, the temperature, length, and density of the plasmas each differed from our studies by at least a factor of 10, and  $B_0 = 0.4 \text{ T}$ . Reference [49] offers some speculation on these differences, although it is difficult to say much without more data. A diffusive model for radial transport presented in Ref. [65] is a start to understanding these experiments, but the model has only mixed success describing measurements near the resonance [66] and has yet to be studied for rotation frequencies significantly less than the axial bounce frequency, as is the case in our plasmas. Moreover, to apply to our  $\text{e}^-$  and  $\text{e}^+$  plasmas, the collisions dynamics used in the model must be altered to accommodate strong magnetic fields [67].

## 3.2 Antihydrogen Produced in a Penning-Ioffe Trap

Since charged-particle confinement appears sufficient, we move on to a proof-of-principle demonstration of  $\bar{\text{H}}$  synthesis in a Penning-Ioffe trap. To begin,  $1 \times 10^5 \bar{\text{p}}$



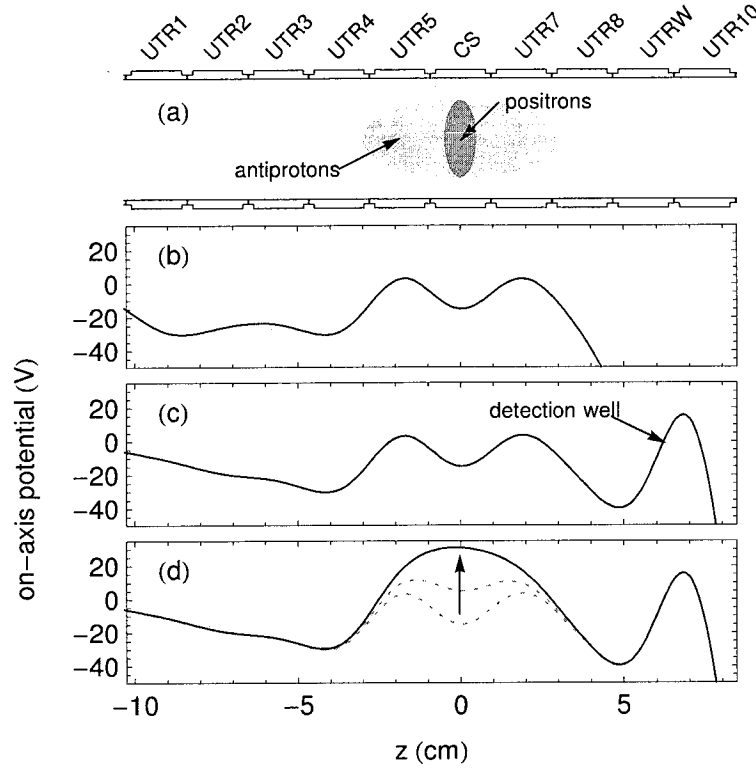


Figure 3.4: Trap potentials during the  $\bar{\text{H}}$  formation in a nested well. (a) The  $\bar{\text{p}}$  cloud and  $\text{e}^+$  plasma, schematically shown within a cross-section of the trap electrodes, are held in the (b) initial nested-well trap potentials. (c) After the Ioffe trap field is increased to the desired strength, a detection well is created with electrode UTR10. (d)  $\bar{\text{H}}$  formation occurs as the  $\text{e}^+$  well (dashed) is decreased until it is eventually inverted (solid).

and  $6 \times 10^7 \text{ e}^+$  are loaded into a nested Penning trap [41] as shown in Fig. 3.4a-b. The  $\bar{\text{p}}$  are loaded by injection from a well with large potential energy on electrode UTR3. Collisions with  $\text{e}^+$  cool the  $\bar{\text{p}}$  to their positions shown, with axial energy on the order of the well depth, 10 eV. The  $\text{e}^+$ , meanwhile, cool via synchrotron radiation to equilibrate with blackbody radiation from the 4 K trap electrodes.

As in the stability studies above, the Ioffe trap current is then increased at 0.1 A/s to the desired field. The deepest trap is produced by 69 A in the quadruple coil and

80 A in the solenoidal pinch coils. As discussed in Section 2.1.2, this corresponds to a trap depth of 380 mK for low-field-seeking ground-state  $\bar{\text{H}}$ . Once the magnets have been energized, a deep  $\bar{\text{p}}$  well is created on electrode UTR10 (Fig. 3.4c) which will be used to detect  $\bar{\text{H}}$ .

Antihydrogen is formed as the  $\text{e}^+$  confinement is decreased over 11 min, as shown in Fig. 3.4d. Once the potential barrier is just low enough, a  $\bar{\text{p}}$  enters the  $\text{e}^+$  plasma with relatively little kinetic energy. Atoms are formed by three-body recombination, when a  $\bar{\text{p}}\text{-e}^+$  bound state is formed as a second  $\text{e}^+$  carries away excess energy. At the end of this procedure, the remaining positrons escape since they are no longer confined by the trap potential (solid line in Fig. 3.4d).

Antihydrogen atoms are detected by a Stark-ionization technique [2]. Atoms that travel to the detection well on electrode UTR10 and are stripped in an electric field of 20-120 V/cm leave their  $\bar{\text{p}}$  trapped within this well. These electric fields correspond to detection of guiding center atoms with a radius of 0.2 to 0.4  $\mu\text{m}$  [49]. After  $\bar{\text{H}}$  formation, the Ioffe trap fields are removed over 1 min and the  $\bar{\text{p}}$  remaining in the  $\bar{\text{H}}$  formation region are ejected. In the final step, the  $\bar{\text{p}}$  delivered to the detection well by  $\bar{\text{H}}$  are ejected and counted (methods in Section 2.3.3).

Figure 3.5 shows the number of  $\bar{\text{H}}$  detected by this method. The key demonstration is a count of 200  $\bar{\text{H}}$  atoms produced within the full Ioffe trap field. Interestingly, this is an increase from the roughly 100 atoms detected when no Ioffe field is applied. For comparison, trials are also shown for which only the solenoidal pinch coils were energized. These trials also generally show an enhancement with 500 atoms detected at full field, although there are some outlying, yet reproducible, counts at intermediate

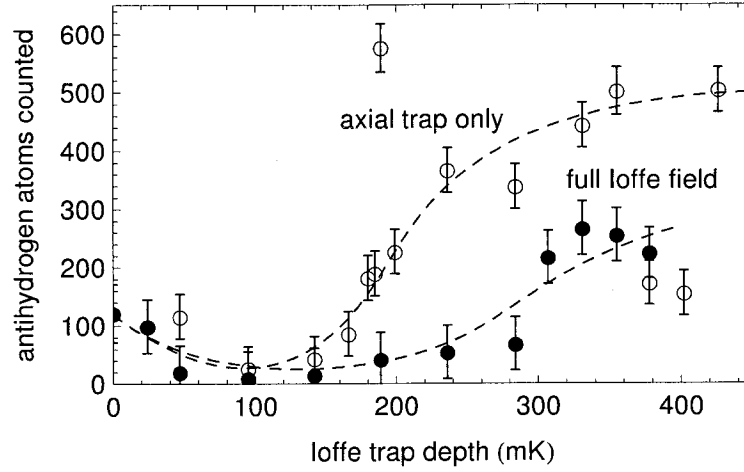


Figure 3.5: Antihydrogen atoms detected by counting  $\bar{p}$  collected by Stark ionization. Trials are conducted in varying Ioffe trap strengths with (filled) and without (open) the radial trapping field. Smooth curves are added to guide the eye. Adapted from Ref. [6].

fields. Speculatively, the enhancement may be due to increased plasma densities at higher magnetic fields (see Section 4.2.2). This enhancement is then partially offset by the deleterious effects of the radial quadrupole field. Although these trials conjure many questions, as a proof-of-concept the data are clear. Many  $\bar{H}$  atoms have been formed within a Ioffe trap. This is an important milestone toward the goal to loading a magnetic trap with  $\bar{H}$  for spectroscopy.

### 3.3 Search for Trapped Antihydrogen

To search for trapped  $\bar{H}$ , we detect  $\bar{p}$  annihilations while the Ioffe trap is turning off. In these trials, no Stark-ionizing detection well is used, and after the atom formation procedure, all charged particles are ejected from the Penning trap with an electric field on the order of 1 V/cm along the entire trap axis. The trap is opened by

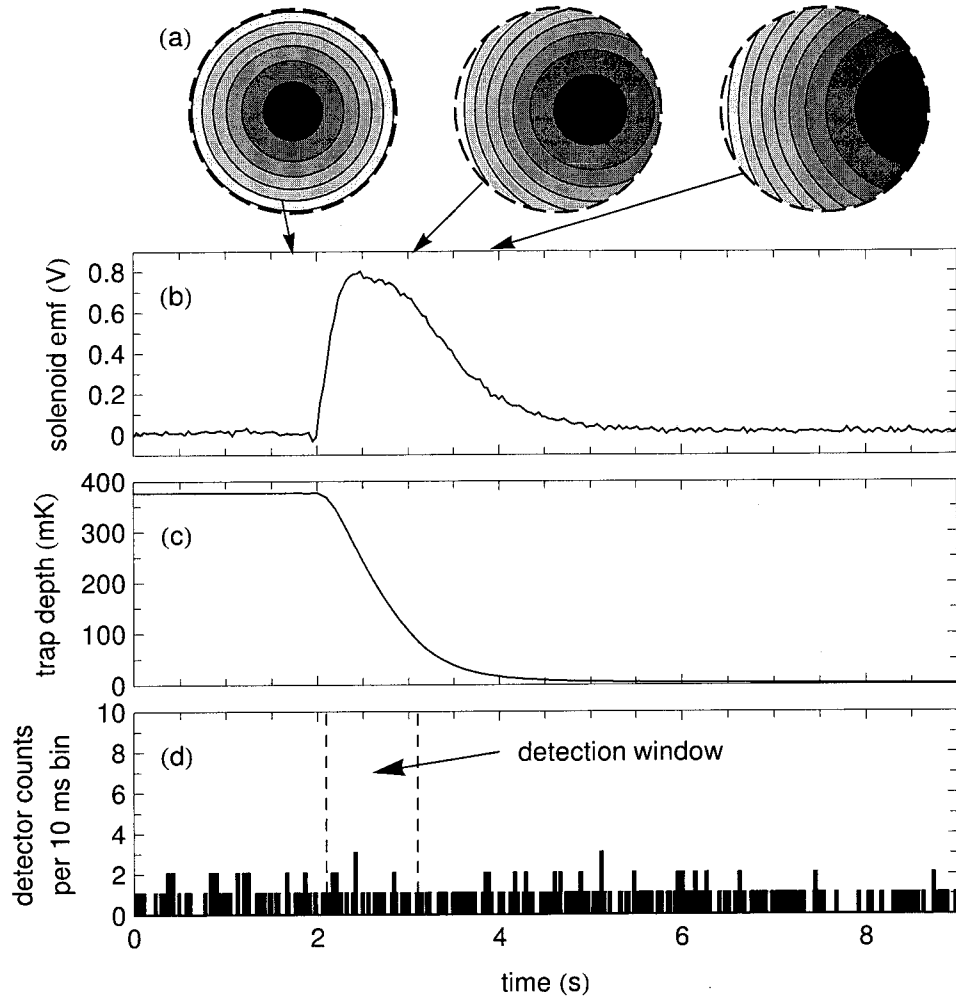


Figure 3.6: Opening the Ioffe trap to look for captured  $\bar{\text{H}}$  by quenching a radial racetrack coil. (a) Cross-section of trap contours in the axial center of the trap during the quench. The trap boundary, a Penning-trap electrode surface is shown (dashed). (b) The rapid change in field induces a voltage on a nearby solenoid which is used to determine (c) the diminishing trap depth. (d) Trapped  $\bar{\text{H}}$  would appear as detector counts above background while the trap is opening.

quenching one of the four racetrack coils of the quadrupole magnet with a resistive heater. This approach is used to turn off the trap in a time shorter than that which is otherwise limited by internal protection diodes [52].

This quench procedure is illustrated in Fig. 3.6. Here, the quench is observed by the voltage induced on a nearby magnet, the antiproton-loading solenoid. The mutual inductance of the quenched racetrack coil and solenoid is used to determine the coil current, and thus trap depth, during the quench. This measurement has also been verified with a magnetometer located outside of the cryostat. Figure 3.6c shows that approximately 80% of the trap is removed in 1 s, and the corresponding detection window is shown in Fig. 3.6d on real-time data collected for a particular detector channel. As discussed in Section 2.3.3, the detector performance may be improved by considering certain combinations of detectors that distinguish antiproton annihilations from cosmic rays. A nearly optimal combination with our current detectors proposed in Ref. [48] corresponds to an efficiency of 25% with a background rate of 0.5 Hz. Detection of  $\bar{\text{H}}$  with 99% confidence in one trial requires three counts with this detector scheme, corresponding to roughly 12 atoms. This trial therefore sets a limit on the number of  $\bar{\text{H}}$  atoms that are trapped. A slightly worse detection scheme was used in the first atom-trapping trials, resulting in our report of fewer than 20 trapped  $\bar{\text{H}}$  per trial [6]. It should be noted that over the last two years, trapped-antihydrogen experiments have been conducted by ATRAP for various particle numbers and nested-well mixing schemes in our apparatus, although these measurements are not a focus of this thesis. Last year trapped atoms were detected by the ALPHA collaboration in an apparatus that is optimized for detecting small numbers of  $\bar{\text{H}}$  atoms. A first

report demonstrated an average of 0.1 atoms captured per trial [68], and a recent update announces roughly 1 atom per trial [45]. While consistent with our experiments, these important studies quantify the challenge remaining to substantially increase the number of trapped atoms, as desired for precise spectroscopy.

### 3.4 Discussion

This chapter presents a key milestone toward our goal of the spectroscopy of  $\bar{\text{H}}$  in a magnetic trap. In our first experiments in a combined Penning-Ioffe trap, we find that although the confinement of  $\bar{\text{p}}$  and  $\text{e}^+$  is worsened by the asymmetric magnetic field, it appears sufficient for  $\bar{\text{H}}$  formation. The following proof-of-principle  $\bar{\text{H}}$  synthesis in a Penning-Ioffe trap succeeds, and a first attempt to trap  $\bar{\text{H}}$  atoms sets a limit of fewer than 12 trapped atoms.

Moving beyond this first demonstration, the experimental goal is clear. We seek to substantially increase the number of  $\bar{\text{H}}$  atoms that can be loaded into a magnetic trap. The optimal procedure and plasma parameters for doing so are much less certain.

The parameters of the nested-well scheme that we may be able to control, for example, include the density, size, and temperature of the  $\text{e}^+$  plasma, the number of  $\bar{\text{p}}$  and the kinetic energy and radial position with which they enter the  $\text{e}^+$  plasma. The optimal  $\bar{\text{p}}$  parameters are most apparent. Since many fewer  $\bar{\text{p}}$  than  $\text{e}^+$  are available for experiments, the number of atoms produced should scale linearly with the number of  $\bar{\text{p}}$ . The importance of the initial  $\bar{\text{p}}$  velocity depends on the effectiveness of cooling in the  $\text{e}^+$  plasma, yet small velocities are likely advantageous. (It should be noted that the number of  $\bar{\text{p}}$  used may effect the initial  $\bar{\text{p}}$  velocity since an increased collision

rate in the side of the nested well acts to thermalize the  $\bar{p}$  cyclotron and axial motions and evaporate  $\bar{p}$  into the  $e^+$  plasma at relatively large axial velocities.) Additionally, the  $\bar{p}$  are best kept near the trap axis for both stability in the Penning-Ioffe trap and more importantly, to reduce the rotational velocity acquired due to the radial electric field within the  $e^+$  plasma. A low  $e^+$  density reduces this effect at the cost of diminished atom-formation and cooling rates.

A considerable experimental challenge is the lack of diagnostics available to measure the properties of  $\bar{H}$  that is produced. An innovative use of Stark-ionizing filters has previously allowed for measurement of the velocity and internal states of a subset of  $\bar{H}$  produced [2, 44], but this technique is not sensitive to slow, deeply-bound atoms in which we are most interested. Without other methods available, we first seek to increase the number of trapped  $\bar{H}$  until measurements with these atoms provide further diagnostics. The following chapters constitute a substantial step toward this goal.

## Chapter 4

# Controlling the Geometry of Trapped Plasmas

To optimize the production of antihydrogen that may be confined in a magnetic trap, we first seek to characterize and control the trapped antiproton and positron plasmas from which it is synthesized. In the present chapter, we consider the geometry and density of these plasmas.

Following a brief review of the macroscopic properties of trapped plasmas, the oscillation frequencies of these plasmas are shown to provide an experimentally convenient approach to determine their geometry. Instrumentation used to measure these oscillations is described, along with a demonstration in which the shape of a plasma is controlled by varying trap fields. In the final section, a rotating electric field is used to apply torque to radially compress plasmas. Plasma radii as small as 2 mm are achieved, and the possibility for further compression is discussed. For plasmas with a known number of particles, provided by the loading and counting methods of Sections



2.2 and 2.3, the techniques in this chapter allow for control of their size, density, and rotation frequency. These parameters are foreseen to be critical to optimizing the formation of cold, trappable antihydrogen.

## 4.1 Theory

The properties of trapped nonneutral plasmas have been extensively reviewed elsewhere [55]. A brief summary is presented here.

Radial confinement of a plasma in a Penning trap can be viewed as a consequence of angular momentum conservation. The canonical angular momentum of a plasma with  $N$  particles, each with charge  $q$ , mass  $m$ , azimuthal velocity  $v_\theta$ , and radial position  $\rho$  is

$$P_\theta = \sum_{j=1}^N m v_{\theta,j} \rho_j + \frac{q}{2} B \rho_j^2 \approx \frac{q}{2} B \langle \rho^2 \rangle \quad (4.1)$$

where  $B$  is the strength of the uniform, axial magnetic field. For plasmas considered in this work, the mechanical angular momentum, the first term on the right, is typically five orders of magnitude smaller than the contribution due to the magnetic field, the second term. Therefore, to a very good approximation the cylindrical symmetry of the trap, which implies conservation of  $P_\theta$ , results in a constraint on the mean square radius of the plasma. In real-life traps, slight asymmetries are unavoidable and the resulting torques cause radial expansion of a trapped plasma. In practice, we find that these torques are small enough to achieve plasma confinement times of many days.

The thermodynamic equilibrium state of a trapped nonneutral plasma has a uniform density  $n$  and undergoes rigid-body rotation at frequency  $\omega_r$ . The uniform den-

sity is a consequence of the particles moving to shield out the external trap potential, as viewed in the rest frame of the plasma. The length scale over which external fields are shielded is the Debye length  $\lambda_D \equiv \sqrt{\epsilon_0 kT/nq^2}$ , so at the outer edge of a plasma, the density falls to zero over a length  $\lambda_D$ . The rotation results from the crossed electric and magnetic fields. The density of a plasma is related to the rotation frequency by

$$n = \frac{2\epsilon_0 m \omega_r (\omega_c - \omega_r)}{q^2} \approx \frac{2\epsilon_0 m \omega_r \omega_c}{q^2} \quad (4.2)$$

where the  $\omega_c = qB/m$  is the familiar cyclotron frequency which is typically three orders of magnitude larger than  $\omega_r$ , so to a good approximation  $\omega_r \propto n$ .

In the case of an ideal Penning trap, the trap potential is a quadrupole and the resulting plasma shape has been shown to be a spheroid [69, 70]. It is convenient to characterize the trap potential in terms of an axial frequency  $\omega_z$ , i.e.  $\phi_t = (m\omega_z^2/2q)(z^2 - \frac{1}{2}\rho^2)$ , and the spheroidal plasma shape may be characterized by its axes in the radial and axial directions,  $r_p$  and  $z_p$ . The relative shape of a plasma, given by its aspect ratio  $\alpha \equiv z_p/r_p$ , is related to its density and the trap strength by

$$\frac{\omega_z^2}{\omega_p^2} = \frac{Q_1(\alpha/\sqrt{\alpha^2 - 1})}{\alpha^2 - 1} \quad (4.3)$$

where  $\omega_p \equiv \sqrt{q^2 n / (\epsilon_0 m)}$  is the plasma frequency and  $Q_1$  is the Legendre function of the second kind [70]. A second equation relates  $N$  to  $n$  by the absolute size of the plasma

$$N = \frac{4}{3} \pi \alpha r_p^3 n \quad (4.4)$$

Finally, by calculating the mean square radius of a spheroid, Eq. 4.1 gives the angular

momentum of a spheroidal plasma in terms of its radius

$$P_\theta \approx \frac{1}{5} N q B r_p^2 \quad (4.5)$$

in the our typical limit that  $\omega_r \ll \omega_c$ .

Equations 4.3 and 4.4 reveal that only two parameters are needed to specify the geometry of a plasma in known trap fields. In particular, any two of  $n$ ,  $\alpha$ ,  $r_p$ , and  $N$  are sufficient, except for the pair  $n$  and  $\alpha$  which are directly related by Eq. 4.3. The two additional parameters  $\omega_r$  and  $P_\theta$  are each given by their own bivariate relationship: Eq. 4.2 relates  $\omega_r$  to  $n$  and Eq. 4.5 relates  $P_\theta$  to  $r_p$ . The latter relationship is particularly useful in understanding how a plasma evolves when the trap fields are gradually changed, provided undesired torques can be neglected. When  $\omega_z$  is gradually decreased, for example,  $r_p$  remains unchanged since  $P_\theta \propto r_p^2$ . The plasma expands axially according to Eqs. 4.3 and 4.4. A decrease in  $B$  results in an increase in  $r_p$ , since  $B \propto r_p^{-2}$ . An accompanying slight decrease in  $z_p$  is predicted, a result of the decrease in the space-charge potential. These relationships are confirmed by experiments in Section 4.2.2.

In typical experiments, the number of particles  $N$  is determined by reproducible loading methods (Section 2.2). Furthermore, it is often possible to determine  $N$  at the end of an experiment by a final destructive counting method (Section 2.3). For the second parameter needed to specify the geometry,  $r_p$  can be determined from this same count if a detector with spatial resolution is used [71]. A previous ATRAP apparatus, for example, employed a Faraday cup aperture that clipped the plasma at a particular radius [72]. The following section summarizes an alternate method to be used throughout this work to determine a second plasma parameter: the frequency

of an internal oscillation of a plasma gives an independent relationship between the  $n$  and  $\alpha$  [73].

Before moving on, we should note that a plasma does not have the shape of a spheroid if the electrostatic trap potential deviates substantially from an ideal quadrupole. In this case, the plasma shape may be calculated iteratively with the computer code *equilsor2* [74] that has been implemented in previous ATRAP research [58, 49]. This code determines the equilibrium geometry of a plasma by self-consistently solving Poisson's equation and the plasma density distribution by finite difference methods. Such a calculation was needed, for example, to interpret measurements of a plasma with a radius that was a substantial fraction of the electrode radius [75]. Since the development of the rotating-wall technique, discussed below, it is typically desirable to work with near-spheroidal plasmas of relatively small radii which avoid this complication. However, for experiments that require axial particle loss from a well, such as the antihydrogen experiments in Chapter 3 and antiproton temperature measurements in Chapter 5, the plasmas deviates substantially from a spheroidal geometry and numerical calculations of the plasma shape are needed.

## 4.2 Plasma Modes of Oscillation

A deformation of the density distribution of a trapped plasma results in oscillations about the equilibrium distribution. For small displacements, this motion can be described in terms of linear normal modes of oscillation. For the case of a magnetized ( $\omega_c \gg \omega_p$ ) zero-temperature spheroidal plasma, the eigenmodes are known analytically [73]. By convention, the modes are classified by two integers  $(l, m)$  with axial

mode number satisfying  $l \geq 0$  and azimuthal mode number satisfying  $l \leq m \leq 0$ . The azimuthal mode number  $m$  describes variations along the azimuth, and the axial mode number  $l$  corresponds to variations along the spheroid surface perpendicular to the azimuth. In general, there are many modes for a given  $(l, m)$ . In the case of axially symmetric modes in which  $m = 0$ , for example, there are  $2l$  modes with indices  $(l, 0)$  [73].

The eigenfrequency  $\omega_l$  of the axisymmetric mode  $(l, 0)$  is given by

$$1 - \frac{\omega_p^2}{\omega_l^2} = \frac{k_2}{k_1} \frac{P_l(k_1)Q'_l(k_2)}{P'_l(k_1)Q_l(k_2)} \quad (4.6a)$$

where  $P_l$  and  $Q_l$  are Legendre functions of the first and second kind respectively,  $P'_l$  and  $Q'_l$  are their derivatives, and we define

$$k_1 = \frac{\alpha}{\sqrt{\alpha^2 - 1 + \frac{\omega_p^2}{\omega_l^2}}} \quad k_2 = \frac{\alpha}{\sqrt{\alpha^2 - 1}} \quad (4.6b)$$

This is a generalization of Eq. 4.3, which considered just the  $(1, 0)$  center-of-mass frequency  $\omega_1 = \omega_z$ . Relative frequency corrections to this expression due to finite temperature [76] are on the scale of  $10^{-5}/K$  for the low-order modes of plasmas measured in this work. Although this shift is negligible in the determination of plasma geometry, its application as a temperature diagnostic is considered in Section 5.2. Equation 4.6 introduces an independent relationship between  $n$  and  $\alpha$  for each mode frequency  $\omega_l$  measured. Below we will use this to fully specify a plasma of known  $N$  by measuring the  $(2, 0)$  quadrupole mode frequency  $\omega_2$ . The axial frequency  $\omega_z$  is measured as well, since this gives a more precise determination of the trap potential than is known otherwise.

Modes of spheroidal plasmas were first measured with  ${}^9\text{Be}^+$  ions by detecting a

change in fluorescence due to Doppler shifts resulting from a resonant radio-frequency drive applied to the trap electrodes [77]. In addition, eigenfunctions have been directly imaged by this technique [78]. For plasmas that cannot be optically imaged, modes may be detected by oscillating image currents induced on trap electrodes. Modes of spheroidal electron plasmas, for example, were first measured as peaks in the noise spectrum of a cryogenic tuned circuit [79]. In these studies, plasmas of very low aspect ratio were used so that many mode frequencies fit within the resonance of the tuned circuit.

For antihydrogen experiments, electron and positron plasma mode frequencies have been measured by applying a radio-frequency drive to a trap electrode and measuring the signal transmitted to a neighboring electrode [80, 75, 58]. Plasma modes are indicated by an increase in transmission due to the resonant excitation of the plasma. In an important study, this technique was used to show that the geometry of a plasma determined by mode measurements agrees with that subsequently measured by a segmented particle-counting detector [75]. It should be noted that for a plasma in a non-equilibrium distribution, it is difficult to determine the geometry from mode frequencies. In recent experiments by the ALPHA collaboration, this has motivated the use of an alternate destructive measurement scheme [81].

### 4.2.1 Instrumentation and an Example Measurement

For the work presented in this thesis, a pulsed-drive ring-down-detection measurement scheme has been implemented, as shown in Fig. 4.1. A drive signal of 10 to 100 MHz is generated (Programmed Test Sources PTS 250) and gated by

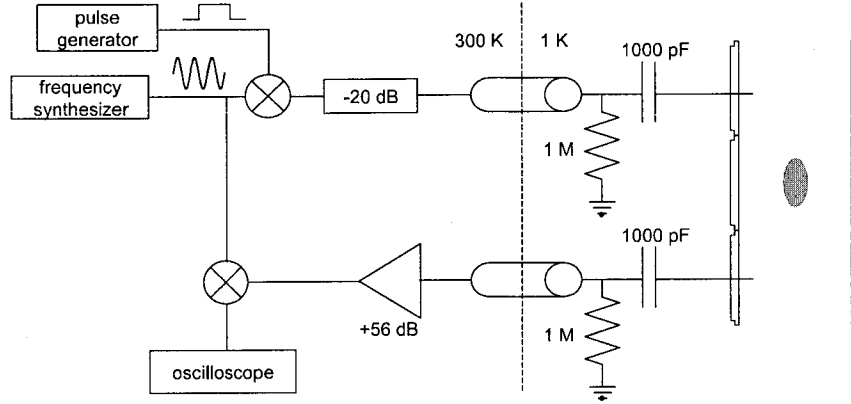


Figure 4.1: Schematic of apparatus used to excite and detect plasma modes.

a pulse with a typical duration of  $1 \mu\text{s}$  (Stanford Research System DG535, Mini-circuits ZYSWA-2-50DR). The resulting pulsed drive has a spectrum approximated by a sinc function centered at the drive frequency with a full-width-half-maximum equal to the reciprocal of the pulse duration. This drive is applied to a trap electrode adjacent to the plasma. The resulting plasma motion induces an oscillating current on the opposite trap electrode which corresponds to a voltage generated across a resistor in that electrode's cryogenic electrical filter (see Section 2.1). This signal is amplified by room-temperature broadband amplifiers, heterodyned with the initial drive frequency, passed through an anti-alias filter, and recorded by an oscilloscope (Cleverscope CS328A-4).

This measurement scheme has a few advantages over the tuned-receiver approach used previously. In that case, the sweep time is constrained by the resolution bandwidth and precludes the resolution of a mode spectrum in a single transient ring down. As a result, the modes must be measured during continuous excitation. Alternately, operating the analyzer in zero-span mode allows for detection during the ring

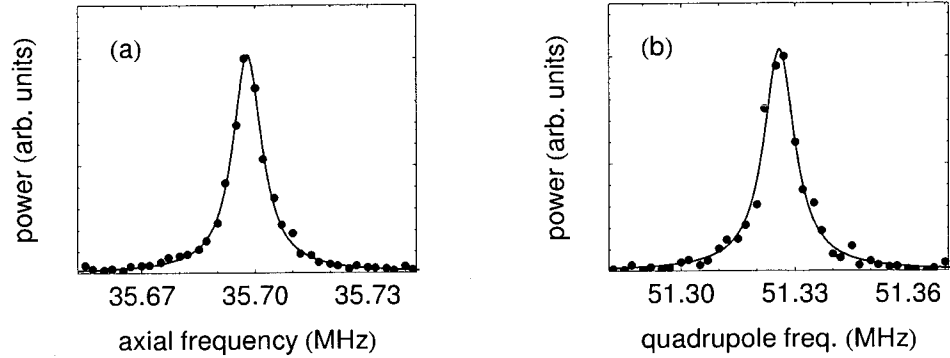


Figure 4.2: Measured ring-down spectra of (a) axial and (b) quadrupole mode resonances. The plasma parameters and fit results are discussed in the text.

down while using a pulsed drive, but requires multiple measurements as the drive and receiver frequencies are swept across the resonance [49]. In contrast, the ring-down detection scheme above can determine the mode frequency to a few kHz within in a range of a few MHz in a single measurement. This reduction of scan time was sought for development of the rotating wall discussed below, which can result in shifts of tens of MHz in mode frequencies. Even after modes are identified, this scheme provides for an improved measurement rate due to instrument data transfer rates. Averaging multiple measurements improves the signal-to-noise ratio to achieve a measurement uncertainty of 100 Hz within a minute, which enables the resolution of slight temperature shifts, as discussed in Section 5.2. Further improvement in the measurement rate by two orders of magnitude, made possible by removing downtime due to data transfer with multiplexed oscilloscopes, would further increase the signal-to-noise achieved within this measurement time.

Figure 4.2 shows typical center-of-mass and quadrupole ring-down spectra. These data result from the fast Fourier transform of recorded voltages starting 3  $\mu$ s af-



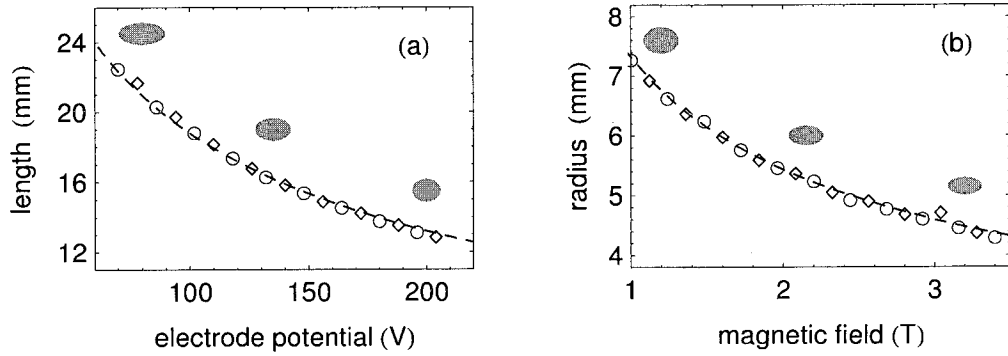


Figure 4.3: The length and radius of a plasma determined by mode frequency measurements as the (a) trap potential and (b) magnetic field are first increased (circles) and then decreased (diamonds). The shape at a few representative points is shown in gray. The prediction of Eq. 4.3-4.5 are shown (dashed).

ter the end of the excitation drive. For this example, the measured frequencies  $\omega_z/2\pi = 35.6980 \pm 0.0005$  MHz and  $\omega_2/2\pi = 51.326 \pm 0.001$  MHz and particle number  $N = (96 \pm 2) \times 10^6$  correspond to a plasma with radius  $r_p = 5.12 \pm 0.04$  mm and density  $n = (8.800 \pm 0.002) \times 10^6$  cm<sup>-3</sup>. The reported uncertainties in the mode frequencies are estimated from typical trial-to-trial fluctuations, while the Lorentzian fits in Fig. 4.2 estimate parameter errors approximately five times smaller. The dominant error in the calculated radius comes from the uncertainty in  $N$ , which was determined at the end of the trial. The resonance widths of 9.4 kHz and 9.8 kHz, for the axial and quadrupole modes respectively, correspond to exponential damping times of approximately 20  $\mu$ s. The measured spectra are independent of the delay between the drive and measurement as well as of the drive power (checked over a range of 20 dB).

### 4.2.2 Controlling the Geometry of a Plasma with Trap Fields

One application of the non-destructive determination of geometry from mode frequencies, is to investigate the manipulation of the shape of a plasma with trap fields. For this example, a plasma of electrons with  $N = 90 \times 10^6$  and  $r_p = 7.2$  mm is loaded with  $B = 1$  T in a trap produced by applying 98 V to electrode LTE3 (Fig. 2.3) with respect to the the other electrodes. The length  $2z_p$  and radius  $r_p$  of the plasma are determined from a measurement of  $\omega_z$  and  $\omega_2$  as the applied voltage and magnetic field are varied. Figure 4.3a shows  $z_p$  as the potential is varied from 70 to 204 V with  $B = 2.2$  T. The plasma shortens with increasing trap potential while the radius remains constant. Next,  $r_p$  is varied by changing the magnetic field from 1 to 3.4 T while the potential is held at 98 V, as shown in Fig. 4.3b. These measurements agree with the prediction of Eqs. 4.3-4.5 (dashed lines) Again, the measured geometry is in agreement with the predictions. For both tests, data is shown for increasing (circles) and decreasing (diamonds) trap fields, demonstrating that the manipulations are reversible.

## 4.3 Compression of a Plasma by a Rotating Electric Field

For control of the geometry of trapped plasmas beyond what is possible by varying trap fields, we need another method to change the angular momentum of the plasma. According to Eq. 4.5, an applied torque results in either radial compression or expansion. This has been achieved, for example, by off-axis resonant laser beams

directed perpendicular to the trap axis [69, 77]. For trapped particles without optical transitions, as for our trapped particles, a torque may be applied by breaking the cylindrical trap symmetry with an azimuthally asymmetric rotating electric field. This method is commonly referred to as a rotating wall [82].

In the first demonstration of the rotating-wall technique, it was found that the applied torque is greatest when the rotating wall frequency  $\omega_{\text{RW}}$  is resonant with plasma modes of non-zero angular momentum [82, 83, 84]. As the excited modes damp through collisions, their angular momentum is transferred to the bulk distribution of the plasma. As a consequence, exciting modes that rotate faster than the plasma causes radial compression. In principal, the plasma can compress until its rotation frequency  $\omega_r$  equals the plasma mode resonant with  $\omega_{\text{RW}}$ . However, typically the background drag due to trap asymmetries increases with density, resulting in a torque-balanced state with  $\omega_r < \omega_{\text{RW}}$ . Further complications arise from heating due to the rotating-wall drive, which results in frequency shifts of the plasma modes [84].

Recently, a qualitatively different rotating-wall regime was observed with a sufficiently strong rotating-wall drive, plasmas with high aspect ratios, and a large magnetic field [85, 86, 87]. In this strong-drive regime, a large torque is achieved over a broad range of  $\omega_{\text{RW}}$  without tuning to plasma modes. Furthermore, the resulting plasma rotation frequency nearly matches the drive frequency  $\omega_r \approx \omega_{\text{RW}}$ . Neither the torque mechanism nor the parameters for which the strong-drive regime is achieved are yet clear. Preliminary experiments point towards a coincidence in the emergence of these results with the onset of a new density-independent transport regime [85]. Speculatively, this suggests that a large particle cooling rate may be important

to reduce the plasma temperature during the rotating-wall drive. A low temperature corresponds to large collision rates that enable reduced transport. A second experiment that demonstrated  $\omega_r \approx \omega_{\text{RW}}$  studied a crystallized spheroidal plasma of  ${}^9\text{Be}^+$  ions [88, 89]. Notably, in these experiments the rotating-wall drive was applied over the entire length of the plasma, which is in contrast to Ref. [85] in which good compression was only achieved if the drive was applied over less than half of the plasma length.

Despite these unresolved theoretical issues, the rotating wall technique has been used in a number of experiments to achieve high-density plasmas and improve storage times by mitigating radial expansion. A rotating wall operated during buffer-gas cooling of positrons, for example, has been used to enhance the brightness of positron beams [90]. Control of positron plasmas by a rotating wall has previously been implemented in antihydrogen experiments [91, 92].

### 4.3.1 Demonstration

The ATRAP apparatus (Fig. 2.3) contains electrodes that can be used to apply rotating-wall fields in both the positron and antiproton loading regions. As illustrated in Fig. 4.4d, these rotating wall electrodes consist of four azimuthal segments with independent radio-frequency electrical connections. For this study, the segments are driven at  $\omega_{\text{RW}}$ , each with a unique phase that differs from its neighboring segments by  $\pi/2$ . These drive signals are generated with a Harvard-built multichannel synthesizer using single-chip direct digital synthesizers (Analog AD9954). The resulting rotating-wall field near the trap center corresponds to a rotating dipole potential  $\phi_{\text{RW}} \propto$

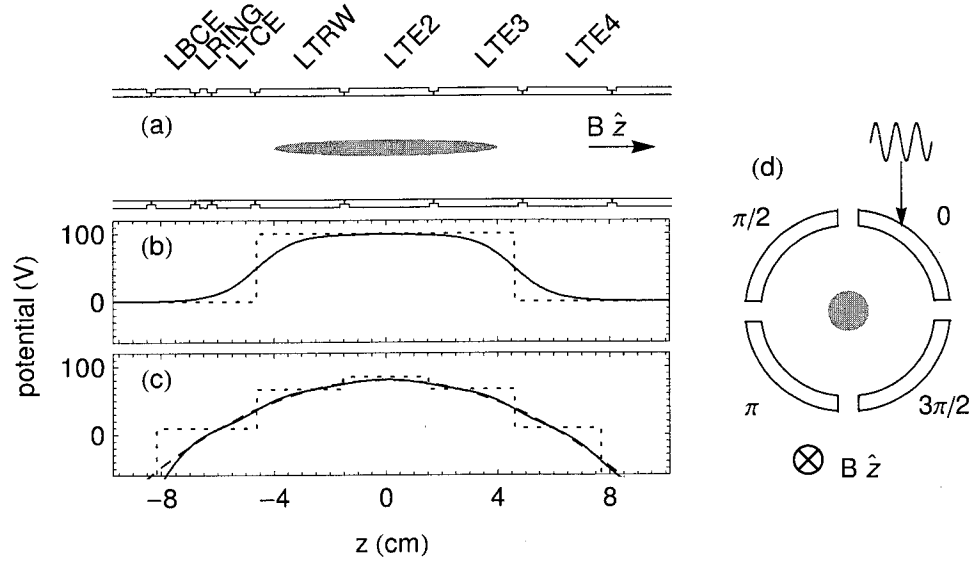


Figure 4.4: (a) An electron plasma positioned within the trap electrodes during a rotating-wall procedure in a (b) flat or (c) harmonic ( $\omega_z/2\pi = 13$  MHz as shown) trap. Potentials along the trap axis (solid) and at the electrode surface (dotted) are shown. The quadratic potential (dashed) is well-approximated by the harmonic trap. (d) Schematic top view of the segmented electrode LTRW with drive phases.

$$y \sin(\omega_{RW}t) - x \cos(\omega_{RW}t).$$

Figures 4.4b-c show two examples of trap potentials used during application of the rotating wall in the antiproton-loading region of the trap. In Fig. 4.4b, a flat Penning-Malmberg potential is created by applying a uniform voltage to three diameter-length electrodes. In Fig. 4.4c, an approximate quadrupole potential is created with seven adjacent electrodes. In this latter case, a least-squares routine is used to find the electrode voltages that best approximate a harmonic potential with specified  $\omega_z$  over the region of the plasma. Although flat potentials allow for closer comparison with previous work, particle loss is typically observed during both the formation of these wells from single-electrode wells and at the start of the rotating-wall drive. As seen

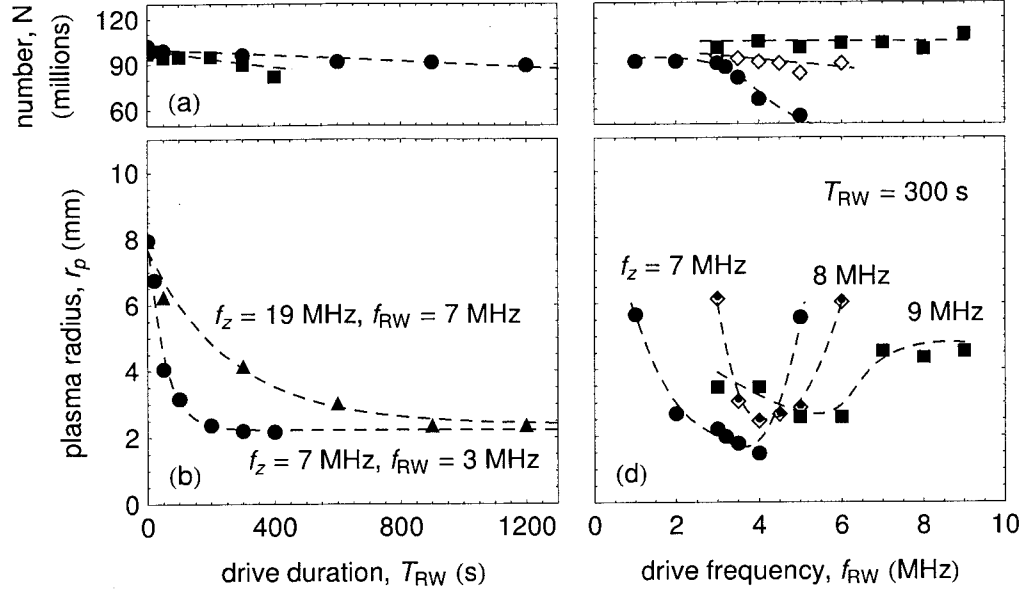


Figure 4.5: (b) Rotating-wall compression of the plasma radius as a function of drive duration. (d) Compression achieved in 300 s as a function of drive frequency  $f_{RW} = \omega_{RW}/2\pi$ . The harmonic rotating-wall potential is varied according to the specified  $f_z = \omega_z/2\pi$ . (a,c) The number of particles remaining at the end of each corresponding trial. Smooth curves are added to guide the eye.

below, these losses are avoided with the use of harmonic potentials.

A demonstration of radial compression due to a rotating wall is presented in Fig. 4.5. Each trial begins with an electron plasma of  $N = (100 \pm 5) \times 10^6$  and  $r_p = 8.0$  mm loaded in a single-electrode well formed by electrode LTE3 with magnetic field  $B = 1$  T. The initial number of particles is estimated from the measured reproducibility of the loading procedure. The plasma is moved to electrode LTE2 (per method in Section 2.3.1) and a seven-electrode harmonic well, as in Fig. 4.4, with specified  $\omega_z$  is formed by smoothly change the electrode voltages over 10 s. A rotating-wall drive with peak-to-peak amplitude of 9 V, duration  $T_{RW}$ , and frequency  $\omega_{RW}$  is applied to the filter network for the segmented electrode LTRW (schematic

in Ref. [52]). The resulting drive amplitude at the electrode vary from 0.7 to 3.5 V for  $\omega_{\text{rw}}/2\pi$  of 1 to 8 MHz. After the drive, a wait of 60 s allows the plasma to rethermalize. The plasma is then returned to electrode LTE3 by the reverse of the initial move procedure, the modes are measured, and the plasma is ejected to determine the number of particles remaining (see Section 2.3.2). No change in plasma geometry was found if the adiabatic move from the rotating-wall well to the mode-measurement well was repeated many times or the cooling time was varied.

Figure 4.5b displays the plasma radius as a function of rotating-wall drive duration. The observed compression times, determined by fits to an exponential function, are 50 s and 300 s for rotating-wall potentials corresponding to  $\omega_z/2\pi = 7$  MHz and 19 MHz, respectively. The drive frequencies  $\omega_{\text{RW}}$  chosen were those that were found to achieve maximal compression for the corresponding  $\omega_z$ . The higher compression rate for lower  $\omega_z$  may be due to a higher torque achieved as a consequence of the proximity of the longer plasma to the segmented electrode. It is unexpected, however, that different torques result in similar steady-state compression. Speculatively, this may be a consequence of increased plasma heating in the case of the higher-torque drive in which the difference between  $\omega_{\text{RW}}$  and  $\omega_r$  is greater, but further studies are needed to explore this hypothesis. The number of particles remaining for each trial is shown in Figure 4.5a. Typically, 95-100% of the initial particles remain at the end of the trial.

The frequency dependence of the compression achieved in  $T_{\text{RW}} = 300$  s is shown in Fig. 4.5d. Note that the rotation frequency of the maximally compressed plasmas,  $\omega_r/2\pi \approx 100$  to 200 kHz, is substantially lower than the drive frequency ( $\omega_{\text{RW}}/\omega_r >$

10). As discussed above, this suggests that we are not in the strong-drive regime [85]. On the other hand, the relatively smooth frequency-dependence observed is not consistent with sharp mode resonances [84]. It is possible that these rotating-wall parameters correspond to a transition region between these two regimes. Alternatively, it may be that the high-frequency drive interacts with closely spaced high-order modes which are substantially broadened by an elevated plasma temperature.

### 4.3.2 Suggestions for Further Rotating-Wall Studies

The rotating-wall method demonstrated in Fig. 4.5 allows for reliable control of electron and positron plasma geometries, enabling the studies presented in the following four chapters. As discussed above, however, there remain outstanding questions concerning the technique (for example, see Ref. [86]). To further motivate future studies in the ATRAP apparatus, it appears that compression of the radius by another order of magnitude, as has been achieved in similar experiments, is possible [85, 84, 91].

If we decide to improve the compression achieved in the ATRAP apparatus, the transition between weak and strong rotating-wall regimes should be further investigated [86]. In particular, studies of compression as a function of drive frequency, as in Fig. 4.5d, should show a qualitative change from mode-resonant to a frequency-independent compression as the drive amplitude is increased. These studies should also be extended to drive frequencies as low as the initial rotation frequency,  $\omega_{\text{RW}} \approx \omega_r$ . The importance of particle cooling may be investigated by the magnetic-field dependence of the drive amplitude needed to achieve strong-drive compression. Addition-



ally, plasma expansion rates may be measured as a function of plasma density to test whether a density-independent rate coincides with the strong-drive regime, as has been previously noted [85]. Lastly, monitoring the frequency shifts of plasma modes (see Section 5.2) during and immediately after the rotating-wall process might enable direct measurement of the plasma heating, provided the plasma remains in a near-equilibrium state throughout the process.

## 4.4 Summary

In this chapter, we described the measurement and control of the geometries of trapped plasmas used in the production of antihydrogen. A non-destructive measurement of the frequency of two plasma modes, the center-of-mass and quadrupole modes, is used along with the number of particles, estimated from reproducible loading methods, to completely specify the geometry of trapped plasmas. Two methods were then used to control this geometry. A plasma was expanded and compressed within a limited range by varying the strength of the trap potential and magnetic field. A rotating electric field is used to apply a torque to a trapped plasma, resulting in radial compression. This so-called rotating-wall method allows ATRAP to realize plasmas with radii as small as 2 mm. This technique results in control over a number of related plasma parameters critical to antihydrogen experiments, including density and rotation frequency. Furthermore, the methods developed in this chapter enable the experiments in the following four chapters, in which we will investigate the temperature of trapped plasmas, develop techniques to cool antiprotons, demonstrate an improved antiproton loading method, and investigate the nature of two-component

electron-antiproton plasmas.

## Chapter 5

# Measuring the Temperature of Trapped Plasmas

We have previously seen how the number of particles (Section 2.2) and geometry (Chapter 4) of a plasma may be determined. The present chapter considers the remaining parameter required to specify a trapped plasma in an equilibrium state, its temperature. Two methods to determine the temperature of a plasma are investigated: measuring the axial energy distribution and measuring pressure-dependent plasma mode oscillation frequencies.

The temperatures of positron and antiproton plasmas are key parameters in the formation of cold, trappable antihydrogen. For antihydrogen formation schemes in which the antiproton plasma is stationary, such as charge-exchange with a Rydberg positronium beam [93, 48], the kinetic energy of the antiprotons will directly determine that of the antihydrogen produced. For schemes in which the antiprotons are injected into the positron plasma, such as three-body recombination in a nested well

[41] (see also Chapter 3), the relationship is more complicated. The initial antiproton temperature along with the mixing method will determine the velocity distribution of antiprotons introduced into the positron plasma. From there, the positron temperature plays a role in collisions that slow antiprotons and the complicated dynamics that produces more deeply bound, low-energy, low-field seeking antihydrogen atoms [19, 94].

## 5.1 Axial Energy Distribution

In this section, we use a direct measurement of the axial energy distribution to determine the temperature of a trapped plasma. This is achieved by counting the number of particles that are sufficiently energetic to escape past a known potential barrier. This technique was first demonstrated with electron plasmas with temperatures on the order of  $10^4$  K [95]. In this work, the method is extended to much lower temperatures with antiproton plasmas temperatures as low as 3.5 K.

Consider a trapped antiproton plasma centered in electrode LTE2, as shown in Fig. 5.1a. The well depth  $W$  is defined as the maximum potential energy gained by an antiproton as it travels along a magnetic field line, parallel to the trap axis, from inside the plasma to escape over the confining barrier. Initially, the plasma is held in a deep well in which  $W$  is much larger than the thermal energy,  $W \gg kT$ . The plasma is then in thermal equilibrium with a distribution of axial energies  $E_z$  well approximated by a Boltzmann distribution

$$f(E_z) = \sqrt{\frac{1}{\pi E_z kT}} \exp\left(\frac{-E_z}{kT}\right) \quad (5.1)$$

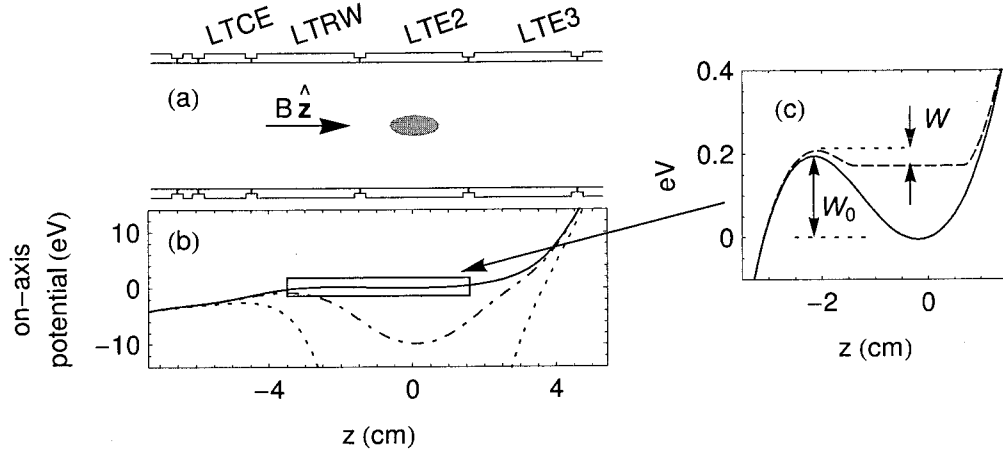


Figure 5.1: (a) A plasma with  $5 \times 10^5$  antiprotons shown in a cross-section of the trap electrodes. (b) The diminishing on-axis trap potential at three times during the measurement. (c) Expanded view of a shallow trap potential (solid) and corresponding total potential, which includes the plasma space-charge (dashed).

since truncation due to finite well depth is negligible. In general, a plasma may be in a quasi-equilibrium state with two temperatures  $T_{\parallel} = T_z$  and  $T_{\perp}$ , corresponding to motion parallel and perpendicular to the magnetic field. This is possible since the time scale to couple energy between these motions may be much longer than the time required for each to independently thermalize [96].

To measure the plasma temperature  $T_{\parallel}$ , the potential applied to electrode LTE2, and hence  $W$ , is continuously reduced, and the corresponding antiproton loss is recorded by standard annihilation detection (see Section 2.3.3). The temperature is deduced from the number lost as a function of  $W$ . We will limit the analysis to the first fraction of the losses, typically 0.1 to 1%, which simplifies the calculation of the space-charge potential, discussed below.

Neglecting collisions that redistribute energy between particles during the brief measurement duration, the number of particles that escape  $dN_{\text{esc}}$  when the well depth

$W$  is reduced by  $dW$  is determined from the axial energy distribution

$$\begin{aligned}
 dN_{\text{esc}} &= N \int_W^{W+dW} f(E_z) dE_z \\
 &= \text{erf}(\sqrt{W+dW}) - \text{erf}(\sqrt{W}) \\
 &\approx \frac{NdW}{W} \sqrt{\frac{W}{\pi kT}} \exp\left(\frac{-W}{kT}\right)
 \end{aligned} \tag{5.2}$$

The approximation in the last line simplifies the data analysis and is valid when  $dW$  is small compared to  $W$  and  $kT$ . This validity is easily checked by calculating the exact result in terms of error functions, and for the measurements presented in this thesis, the approximation is good to better than 5%.

Equation 5.2 assumes a static energy distribution, as would be the case if the measurement was brief compared to the collision time. If this assumption is not met, collisions can cause additional loss. A particle that initially has insufficient energy to escape can acquire this energy in a collision while the measurement is underway. This process is known as evaporation (for example, see Ref. [97]) and has been studied for ions held in an electron beam ion trap [98]. The resulting loss is

$$dN_{\text{ev}} = -\frac{Ndt}{\tau_{\text{ev}}} = -\frac{Ndt}{\tau_{\text{col}}} \frac{3kT}{\sqrt{2}W} \exp\left(\frac{-W}{kT}\right) \tag{5.3}$$

where the evaporation time  $\tau_{\text{ev}}$  has been rewritten in terms of the collision time  $\tau_{\text{col}}$ , which is discussed further below.

If the well depth  $W$  is reduced linearly in time, the total loss  $dN$  is easily analyzed. In particular, due to the common exponential term in the direct escape and evaporation processes, the plasma temperature can be extracted from a linear fit to a logarithm of the loss data

$$\ln\left(\frac{dN}{dW}\right) = -\frac{W}{kT} + a \ln W + b \approx -\frac{W}{kT} + c \tag{5.4}$$

where the constants  $a$ ,  $b$ , and  $c$  are introduced for simplicity and to a good approximation  $\ln W$  does not vary significantly throughout the measurement.

To estimate the relative contributions of  $dN_{\text{esc}}$  and  $dN_{\text{ev}}$ , we must calculate  $\tau_{\text{col}}$ . A classic calculation of collision and transport properties of plasmas in no magnetic field is presented in Ref. [99]. These calculations are performed by integrating over all possible binary collisions, characterized by the impact parameter. If we define  $\tau_{\text{col}}(B = 0)$  as the time required for collisions to redistribute  $kT$  of energy from an initial direction of motion to one in a perpendicular direction, the well-known result is  $\tau_{\text{col}}(B = 0) = (4\pi b_c^2 n v_{\text{th}} \ln \Lambda)^{-1}$  for average thermal velocity  $v_{\text{th}} = \sqrt{2kT/m}$  and classical distance of closest approach  $b_c = q^2/(4\pi\epsilon_0 kT)$ . The Coulomb logarithm  $\ln \Lambda = \ln(\lambda_D/b_c)$  results from the limits of relevant impact parameters,  $b_c$  and the Debye length  $\lambda_D$ .

In a magnetic field strong enough that the average cyclotron radius  $r_c = \sqrt{2mkT}/(eB)$  is smaller than  $\lambda_D$ , the collision kinetics are substantially altered. In particular, the dynamics are no longer isotropic and processes parallel and perpendicular to the magnetic field may occur at much different rates. Reference [100] shows that the influence of the magnetic field on processes parallel to the magnetic field can encapsulated in a generalized Coulomb logarithm,  $\ln \Lambda_B$ . For so-called strongly-magnetized plasmas where  $r_c < b_c$ , it is approximated by  $\ln \Lambda_B \approx r_c^2/2b_c^2$ . For typical antiproton plasmas studied in this section, the calculated collision time  $\tau_{\text{col}} \approx 1$  ms correspond to evaporation times  $\tau_{\text{ev}} \approx 100$  s. Note that the magnetic field is estimated to have increased these times by  $\ln \Lambda_B/\ln \Lambda \approx 300$ . This factor should be taken with some caution, since plasma dynamics in strong magnetic fields is an ongoing area of study,

and these results have yet to be verified experimentally. Nonetheless, for our typical measurement duration of 1 ms,  $dN_{\text{ev}}$  is found to be insignificant compared to  $dN_{\text{esc}}$ .

In addition to causing evaporative loss, collisions also act to reestablish a new thermal energy distribution. In the case of substantial particle loss the new distribution has a lower temperature, a result commonly called evaporative cooling. Since we will analyze fewer than the first 1% of losses, the average energy per particle, and thus temperature, would not change significantly during the measurement even if the collision rate was sufficiently large.

Finally, it should be noted that the above discussion glosses over the radial dependence of the trap potential by characterizing the confinement by the on-axis well depth  $W = W(0)$ . Instead, the analysis can be separated for particles at each radius  $\rho$ , with corresponding well depth  $W(\rho)$ . The well depth  $W(\rho)$  increases with  $\rho$  since the magnitude of the external potential  $W_0(\rho)$  increases with  $\rho$  while the repulsive space-charge potential decreases with  $\rho$ . To make this explicit, Eqs. 5.2 and 5.3 can be written in terms of  $dN(\rho)$ ,  $N(\rho)$ , and  $W(\rho)$ . The total loss is then determined by integrating over  $\rho$ . The simplified Eq. 5.4 is valid as long as the off-axis well depths are proportional to that on-axis throughout the measurement. This assumption has been verified with the space-charge model discussed below. As a check, a full calculation that includes radial dependencies has been found to agree with the on-axis analysis for the measurements presented in this chapter.



### 5.1.1 Space-Charge Potential Model

As shown in Fig. 5.1c, the well depth  $W$  differs from the external potential  $W_0$  due to the plasma space-charge potential. The Coulomb repulsion of particles substantially reduces the kinetic energy required to escape. Moreover, we will see that it is a poor approximation to take the space-charge effect as constant throughout the measurement. This complicates the analysis, since unlike  $W_0$  which is determined only by the electrode voltages,  $W$  requires a model of the plasma.

The geometry of the plasma throughout the temperature measurement is calculated with the computer code *equil2* [74], discussed in Section 4.1. An equilibrium geometry is preserved throughout the measurement since the axial expansion of the plasma occurs at a time scale much slower than the relevant internal plasma dynamics. The geometry is uniquely determined by the external potential, particle number  $N$ , and total angular momentum  $P_\theta$  (see Section 4.1), so the ramp-out is modeled by a series of calculations with specified  $N$  and  $P_\theta$  for the trap potential at various times throughout the measurement. A continuous model is constructed by interpolation. The angular momentum is related to the initial spheroid radius  $r_p$  by Equation 4.5. Since we consider fewer than the first 1% of losses,  $N$  and  $P_\theta$  are approximately conserved in so far as they affect the plasma geometry. Extending the analysis further would require including the effects of loss, which creates a non-equilibrium state with its density preferentially diminished near the trap axis. Moreover, this distribution would result in possible radial transport on the time scale of the measurement [101].

The on-axis potentials calculated at three times during the temperature measurement of a 3-mm-radius plasma are shown in Fig. 5.2a along with the corresponding

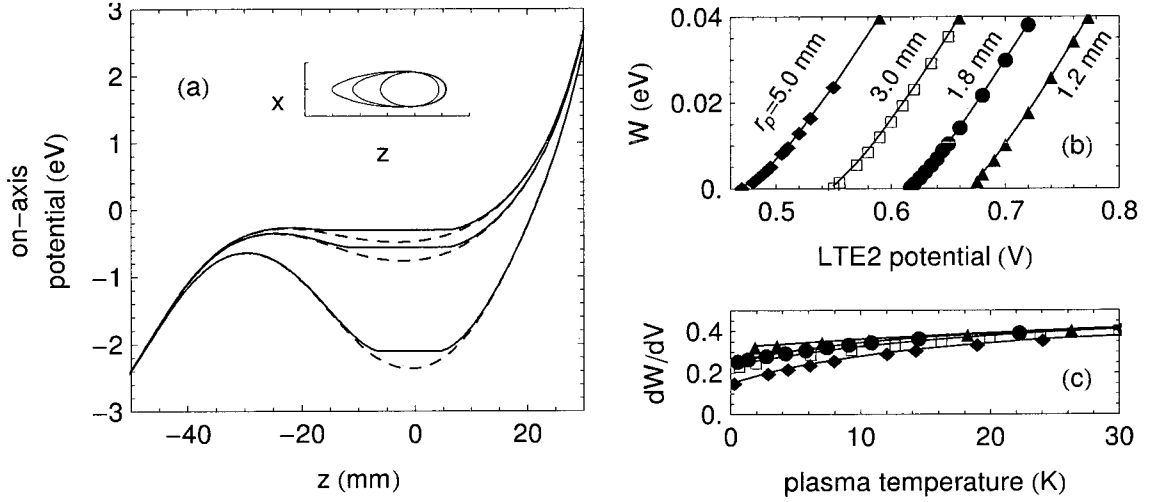


Figure 5.2: (a) On-axis trap (dashed) and total (solid) potentials calculated at three times during a simulated measurement, with corresponding plasma outlines (inset). (b) Calculated well depth  $W$  as a function of voltage  $V$  applied to electrode LTE2 for measurements of plasmas with radii  $r_p$ . (c)  $dW/dV$  as a function of plasma temperature for each simulated plasma.

plasma shape (inset). For each of these curves, which corresponds to voltage  $V$  applied to electrode LTE2, the axial well depth  $W$  is determined. The calculated mappings  $W(V)$  for plasmas with 1.2, 1.8, 3.0, and 5.0 mm radii are shown in Fig. 5.2b. These curves differ primarily due to an increased on-axis space-charge potential caused by radial compression.

To extract the temperature from particle loss data, Eq. 5.2 can now be expressed in terms of  $V$  instead of  $W$ . To do this, a linear approximation of  $W(V)$  is taken over the range of the measurement, near  $V = V_0$

$$W(V - V_0) \approx W(V_0) + \left. \frac{dW}{dV} \right|_{V_0} (V - V_0) \quad (5.5)$$

Equation 5.4 can now be expressed in terms of  $V$

$$\ln \left( \frac{dN}{dV} \right) \approx -\frac{V}{kT} \left. \frac{dW}{dV} \right|_{V_0} + \text{const.} \quad (5.6)$$

An appropriate  $V_0$  is determined by the value of  $W(V_0)$  for which the total loss  $dN/dW$  calculated by Eqs. 5.2 and 5.3 corresponds to the observed loss during the measurement (typically 10 to 100 per meV). The resulting  $dW/dV$  calculated for plasmas of varying radius and temperature are shown in Fig. 5.2c. The slight temperature-dependence of  $dW/dV$  is included when extracting the temperature from a fit to Equation 5.6. Figures 5.2b and 5.2c show that although  $V_0$  depends strongly on the plasma radius,  $dW/dV$  during the measurement does not. Interestingly, data such as those shown in Fig. 5.2b and the measured voltage at which losses start provides a direct measurement of the plasma radius. For example, determining this voltage to within 10 mV corresponds to an uncertainty in radius of approximately 0.1 mm for the smaller plasmas considered. The accuracy of this approach, however, requires a careful consideration of patch effects on electrode surfaces and other limitations to controlling the trap potentials. In practice, we find agreement with the  $r_p$  inferred from electron mode measurements to within 0.4 mm.

Accounting for the space-charge potential is necessary since the space-charge potential changes significantly throughout the measurement. The expansion of the plasma increases the space-charge contribution to the total potential at the barrier maximum. The space-charge potential inside of the plasma also diminishes slightly. Neglecting this effect, corresponding to  $dW/dW_0 = 1$ , would be an error of factor of 1.3 to 2. This is in contrast to the original axial energy distribution measurements of hot electron plasmas, which considered only very high aspect-ratio plasma for which the change in space-charge potential was appropriately neglected [95]. It should be noted that our analysis does agree with work on lower-aspect-ratio electron plasmas,

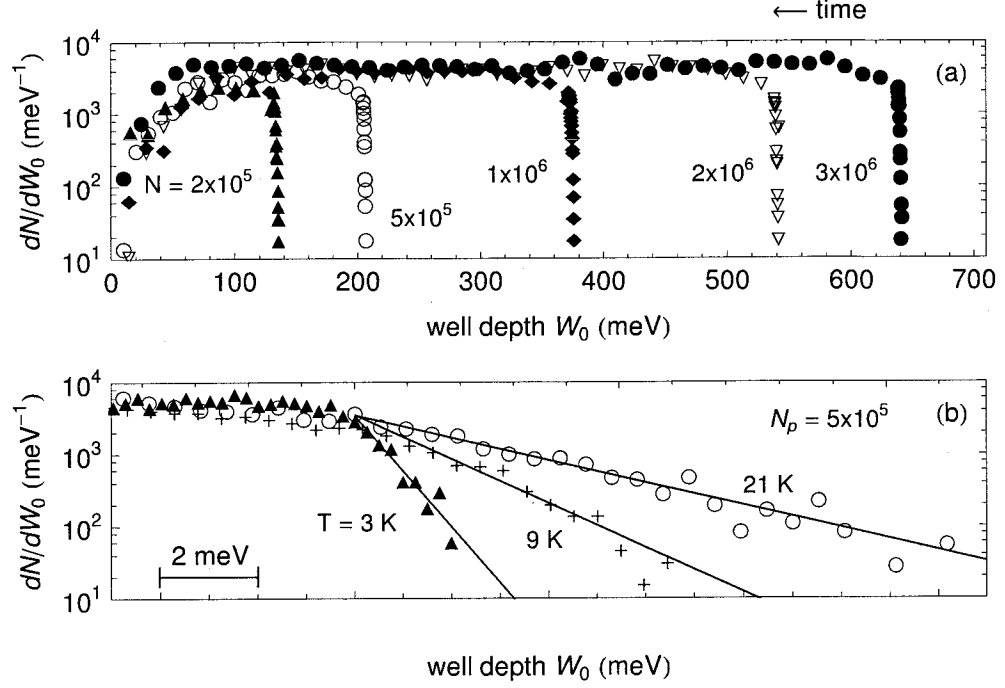


Figure 5.3: (a) Antiproton loss recorded as  $W_0$  is reduced linearly in time for five trials with plasmas containing the number of particles indicated. (b) The measurement region of loss data for three plasmas of varying temperature. The data are aligned by an offset in  $W_0$  chosen so that the slopes, which reveal the temperature, may be easily compared. Adapted from Ref. [103].

that we learned about during the writing of this thesis [102].

### 5.1.2 Measurement Example

Data from typical temperature measurements are shown in Fig. 5.3. Antiproton plasmas are prepared with a 2-mm radius in a 3.7-T magnetic field and transferred to the potential scheme in Fig. 5.1 with methods described in Chapters 2 and 4. The voltage applied to electrode LTE2 is then reduced linearly in time, resulting in a decrease in  $W_0$  of 2.2 eV/s. The antiprotons counted per unit change in well depth is recorded as a function of the decreasing well depth.

Five trials in which the number of antiprotons is varied from  $2 \times 10^5$  to  $3 \times 10^6$  are shown in Fig. 5.3a. As a consequence of larger space-charge potentials, plasmas with more particles show loss starting at a larger  $W_0$ . The nearly-vertical onset of particle loss contains the first few thousand counts used to determine the temperature. This fit region is shown for three trials with  $5 \times 10^5$  antiprotons in Fig. 5.3b. These plasmas were prepared at different temperatures by a varied amount of adiabatic cooling, as discussed in Chapter 6. The temperatures are determined by a fit to Eq. 5.6 to be  $2.9 \pm 0.3$ ,  $9.4 \pm 0.7$ , and  $21 \pm 3$  K, where the error estimated from the fit is due to the error in counting small numbers of antiprotons. A better indicator of the uncertainty in the temperature measurement is reproducibility with which plasmas of a certain temperature can be prepared and measured, since this sets a practical limitation on tests for systematic errors. In Section 6.2, for example, eighteen identically prepared plasmas are cooled to mean temperature of 3.5 K. The standard deviation of 0.7 K in these repeated trials is a reasonable estimate of the precision of low-temperature measurements. Within this reproducibility, identical temperatures are determined when the measurement rate is varied from 1.1 to 4.3 eV/s.

### 5.1.3 Discussion

In the first demonstration of electron-cooling of antiprotons, an upper limit on the resulting temperature was estimated by the total width of loss curves such as Fig. 5.3a [34]. The method presented in this chapter improves upon this work by calculating the space-charge potential and deducing the temperature from the high-energy tail of the energy distribution revealed in the onset of losses. As a result,

for the first time the temperature of antiproton plasmas are measured to a precision greater than the space-charge energy, which is an energy on the order of 1000 K for  $10^6$  particles. In Chapter 6, this measurement method is used to study two techniques to cool antiprotons: sympathetic cooling of antiprotons by a small number of electrons embedded in an antiproton plasma, and cooling by adiabatic expansion. Concurrent with this work, a closely related measurement was developed and used to demonstrate evaporative cooling of antiprotons [104].

A lower limit on the temperatures amenable to this measurement is likely set by fluctuations in the trap potentials. In particular, fluctuations on the order of a few  $kT$  that occur on the time-scale of the measurement will completely obscure the data. It is not clear what this limit is in our apparatus, since we have yet to produce antiproton plasmas cold enough to create anomalous loss data. It is possible higher-frequency fluctuations will heat plasmas during the measurement process so that such a limit cannot be reached.

Lastly, we should note that although the analysis presented is applicable to positron and electron plasmas, these measurements are hampered in our current apparatus by less efficient counting techniques. Since positron detection efficiency is less than 1%, reproducing measurements in this chapter based on only a few thousand particles is not possible. To accommodate larger losses, the space-charge model developed in Section 5.1.1 must be extended beyond the constant- $N$  approximation. Alternately, a high-efficiency detector such as a micro-channel plate may be used if it can be practically incorporated into the complex apparatus.

## 5.2 Measurement of Plasma Oscillation Frequencies

An alternate determination of plasma temperatures uses measurement of the frequencies of internal oscillations of a trapped plasma (introduced in Chapter 4). In contrast to the axial energy measurements discussed above, this method does not require destructive counting of small numbers of particles. This approach appears well-suited to the continuous monitoring of plasma temperatures, a diagnostic that could, for example, lead to precise control of the temperature of positrons during antihydrogen synthesis.

### 5.2.1 Background and Theory

A temperature-dependent correction to the zero-temperature expression for mode frequencies (Eq. 4.6a) arises from a finite plasma pressure [76, 105, 106]. While pressure does not alter the (1,0) center-of-mass oscillation frequency, higher-order internal oscillations increase in frequency with temperature. In this study, we measure the temperature-dependent (2,0) quadrupole frequency  $\omega_2(T)$ , which is predicted [76] to differ from its zero-temperature value  $\omega_2(0)$  according to

$$[\omega_2(T)]^2 = [\omega_2(0)]^2 + \frac{5kT}{mz_p^2} \left( 3 - \frac{\alpha^2}{2} \frac{\omega_p^2}{[\omega_2(0)]^2} \frac{\partial^2}{\partial \alpha^2} \left[ \frac{2Q_1(k_2)}{\alpha^2 - 1} \right] \right) \quad (5.7)$$

where  $Q_1$  is the Legendre function of the second kind and  $k_2 = \alpha/\sqrt{\alpha^2 - 1}$  as introduced in Eq. 4.6a. For a small change in temperature  $\Delta T$ , the corresponding change in quadrupole frequency  $\Delta\omega_2$  is approximately linear in  $\Delta T$

$$\Delta\omega_2 \approx \frac{5k\Delta T}{2\omega_2 m z_p^2} \left( 3 - \frac{\alpha^2}{2} \frac{\omega_p^2}{\omega_2^2} \frac{\partial^2}{\partial \alpha^2} \left[ \frac{2Q_1(k_2)}{\alpha^2 - 1} \right] \right) \quad (5.8)$$

which is valid for  $\Delta\omega_2/\omega_2 \ll 1$ . This criterion is satisfied for plasmas in this study, for which a temperature change of 1 K results in  $\Delta\omega_2/\omega_2 \approx 10^{-5}$ .

The first measurements of the temperature dependence of spheroidal-plasma modes were undertaken using electron plasmas in the temperature range of 30-150 meV [76]. More recently, this technique has been applied as a diagnostic of positron plasmas heated by 50-500 meV [107] and electron plasmas at temperatures of 500-3000 meV during the electron-cooling of high-energy protons [108]. In a related approach, the temperature-dependent resonance widths of electron-plasma modes in a Penning-Malmberg trap have been measured for temperatures of 50-5000 meV [109, 110]. Below we study substantially colder plasmas than those in these previous studies. In particular, we investigate temperature changes of 0.1-0.3 meV (1-3 K) in cryogenic plasmas.

### 5.2.2 Measurements

A temperature variation  $\Delta T = 2.6$  K in a spheroidal electron plasma is shown in Fig. 5.4. In this example, the plasma parameters are  $N = 104$  million,  $\omega_z/2\pi = 35.5$  MHz,  $\alpha = 2.21$ , and  $r_p = 4.82$  mm. To produce this modulation in temperature, the surrounding trap electrodes are varied between 1.5 and 4.5 K by altering the pressure in the pumped helium cryostat [53] (see also Section 2.1). The electron cyclotron motion couples to the electrode via blackbody radiation with a characteristic time of  $(\gamma_e)^{-1} = 3\pi\epsilon_0 m_e c^3 / q^2 \omega_c^2 = 2$  s in the 1-T magnetic field used throughout these studies. The equilibration of motion parallel to the magnetic field with the cyclotron motion occurs at a rate strongly dependent on the plasma temperature [96, 111]. For



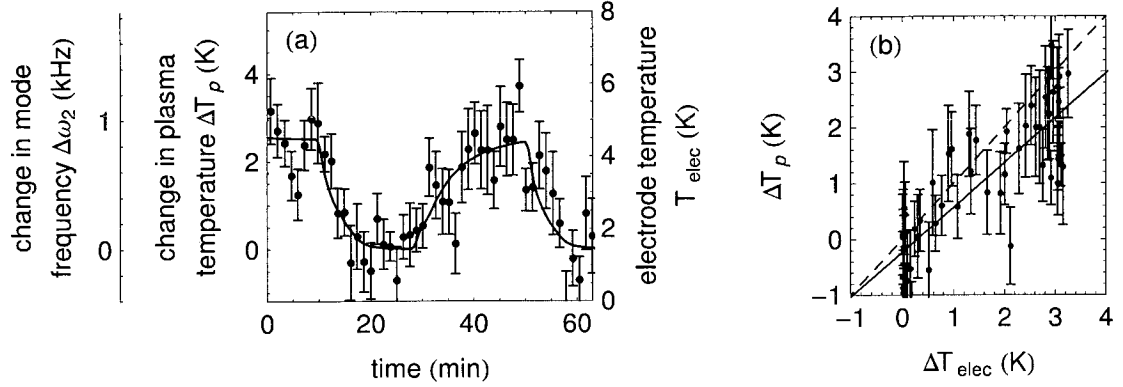


Figure 5.4: Relative quadrupole mode frequency  $\Delta\omega_2$  and temperature  $\Delta T_p$  of a spheroidal electron plasma (parameters specified in the text) in response to a varied electrode temperature  $T_{elec}$ . (a) Plasma mode (points) and  $T_{elec}$  (line) measurements. (b) Explicit time dependence is removed and coinciding temperatures are shown with a best-fit line (solid) and  $\Delta T_p = \Delta T_{elec}$  (dashed).

the plasma described here, the equilibration time is predicted to vary from 0.01 to 40 s for temperatures of 4.0 to 1.7 K.

Figure 5.4a shows the relative quadrupole frequency and plasma temperature, per Eq. 5.8, as the electrode temperature (solid line) is modulated. The mode frequencies are measured at a repetition of approximately 1 Hz by the methods discussed in Section 4.2, alternating between  $\omega_z$  and  $\omega_2$ . For clarity, the data points shown are averages of 75 consecutive measurements, and a linear drift of the quadrupole frequency in time of 9 kHz over the measurement duration has been removed. This drift is likely due to gradual radial expansion of the plasma, corresponding to a rate of 7  $\mu\text{m/hr}$ .

In Fig. 5.4b, the explicit time dependence of these data is removed and the relative plasma temperature  $\Delta T_p$  is displayed as a function of relative electrode temperature  $\Delta T_{elec}$ . The data are consistent with a linear dependence on electrode temperature.

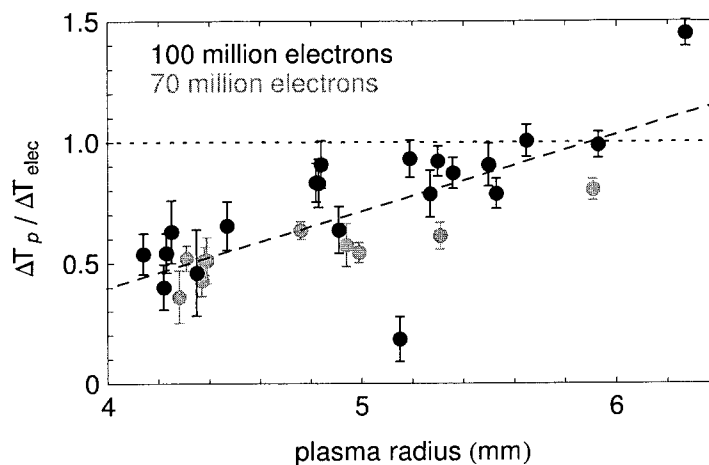


Figure 5.5: Relative temperature shift measured for plasmas with varying radius and number of particles.

For this example, the best fit line gives  $\Delta T_p / \Delta T_{elec} = 0.83 \pm 0.09$ . In contrast, the dashed line corresponds to the plasma temperature changes equaling those of the electrode,  $\Delta T_p / \Delta T_{elec} = 1$ .

Figure 5.5 summarizes multiple trials following this procedure with plasmas of varying  $r_p$  and  $N$  as specified. The observed fractional temperature change of less than unity and its dependence on the plasma geometry is not yet understood. As displayed, trials with different numbers of particles are roughly consistent, suggesting the simplest explanation involves the plasma radius, rather than for example, aspect ratio, plasma length, or density. It should be noted that neither improving the well harmonicity by biasing three adjacent diameter-length electrodes, instead of just one, nor decreasing the mode drive amplitude has a measurable effect.

A fractional temperature shift less than unity is predicted by a simple thermal model in which the plasma is coupled to a second thermal reservoir at a temperature

higher than that of the electrodes. The observed variation in Fig. 5.5 could then correspond to a geometry-dependent coupling strength. However, a possible heat source has not been identified. The time constant for coupling to room-temperature resistors, for example, is prohibitively long. This is, in fact, why resistive cooling was originally rejected as an undesirable approach to cooling high-energy antiprotons [35]. It should be noted that an undesirable heating of electrons embedded in antiproton plasmas is observed in Chapter 6, and may be related to these results. Lastly, it is possible that Eq. 5.7 is inadequate for a more fundamental reason, as  $\omega_2(T)$  has not previously been investigated in the few-Kelvin regime, but possible heat sources in our apparatus must be better characterized to make this experimental claim.

### 5.2.3 Discussion

Precise plasma mode frequency measurements have been demonstrated to resolve changes in the plasma temperature on the order of 100 mK. The method is non-destructive and can be used to continuously monitor the temperature of a plasma, provided that any changes in geometry or particle number are independently determined. As a first application, this measurement was used to study the use of the trap temperature to vary the plasma temperature via blackbody radiation. A few other applications and suggestions for future studies are discussed below.

Monitoring the plasma temperature allows for controllable heating with weak oscillating electric fields that excite plasma modes. For example, in preliminary studies we have shown reliable heating of 10-100 K by varying the strength of a 400-kHz-bandwidth noise drive with a central frequency tuned to the quadrupole mode. The

temperature of positron plasmas has previously been varied by similar methods to study antihydrogen formation mechanisms [107] and will likely be a useful parameter in understanding the production rate of trapped antihydrogen. Heated positron plasmas may also be amenable to the axial-energy measurements discussed in Section 5.1, providing experimental corroboration of the two methods, as well as possibly connecting the relative mode temperature to an absolute value. Heating electrons in an electron-antiproton plasma may allow for an investigation of the centrifugal separation temperature discussed in Chapter 8.

A second application of this temperature measurement is to study possible temperature anisotropization [96, 112, 111]. As mentioned above, the rate at which collisions equilibrate particle motions perpendicular and parallel to the magnetic field is strongly suppressed for sufficiently low temperature and strong magnetic field. Parameters predicted to result in substantial anisotropization are within reach of our experiments. For example, the equilibration time for the plasma studied in Fig. 5.4 decreases from 0.01 to 40 s for a temperature decrease from 4 to 1.7 K. If the magnetic field is increased from 1.0 to 1.7 T, however, the rate is predicted to drop from 0.4 to  $10^4$  s for this same change in temperature. This predicted decoupling between cyclotron cooling and axial motion would result in a drastic change from the linearity shown in Fig. 5.4b, unless an additional cooling mechanism is significant [113]. The equilibration rates at these low temperatures has important implications for the cooling of antiprotons by embedded electrons, studied in Section 6.1.

Finally, there is the important possibility of using plasma mode measurements for an absolute, rather than relative, measurement of temperature. One approach is to

measure an additional plasma mode frequency with a different temperature dependence. For example, the temperature-dependence of the upper (3,0) mode frequency  $\omega_{3,0}^{(1)}$  is roughly four times larger than that of  $\omega_{2,0}$  for a plasma with  $\alpha = 1$  [106]. For the example measurement shown in Fig. 5.4,  $\omega_{2,0}$  was measured to a fractional precision  $\Delta\omega/\omega = 2 \times 10^{-6}$ . If  $\omega_{3,0}^{(1)}$  were measured to the same precision, the absolute temperature would be determined with an uncertainty of 0.3 K. Preliminary measurements failed to detect  $\omega_{3,0}^{(1)}$ , so it remains to be seen what level of precision is achievable. An alternate approach to determining an absolute temperature may consider the damping time of an excited mode [110].

## Chapter 6

# Embedded-Electron and Adiabatic Cooling of Antiprotons to 4 K

A central challenge to efficiently trapping a large number of antihydrogen ( $\bar{\text{H}}$ ) atoms is producing atoms with sufficiently low kinetic energy to be captured in a magnetic trap. As was noted when trapping  $\bar{\text{H}}$  was first proposed [4], a state-of-the-art Ioffe trap can only confine ground-state  $\bar{\text{H}}$  with less than 0.1 meV (1 K) of energy. Since the initial kinetic energy of a  $\bar{\text{H}}$  is determined by that of the antiproton ( $\bar{\text{p}}$ ) from which it formed, a substantial increase in trapping efficiency may be achieved by reducing this  $\bar{\text{p}}$  energy to lower than Ioffe trap depth. The present chapter works towards this goal by studying methods to reduce the temperature of  $\bar{\text{p}}$  available for  $\bar{\text{H}}$  experiments.

We investigate two methods to cool antiprotons: sympathetic cooling by embedded electrons and cooling by adiabatic expansion. First, cooling by a small number of electrons ( $\text{e}^-$ ) co-trapped with  $\bar{\text{p}}$  is studied. These so-called embedded  $\text{e}^-$  are found to

effectively remove heat added to the  $\bar{p}$  during typical trap manipulations. Additionally, we find that the number of embedded  $e^-$  can be reliably determined from measured equilibration rates. Cooling beyond the limit of electron-cooling is achieved by subsequent adiabatic expansion. As the confinement potential is gradually reduced, the plasma expands while doing work on the trap fields. We demonstrate adiabatic cooling with trapped plasmas for the first time, while reducing the  $\bar{p}$  temperature by nearly an order of magnitude.

The combination of these two cooling methods is used to produce plasmas of up to 3 million  $\bar{p}$  at  $3.5 \pm 0.7$  K, many more particles and a lower temperature than has previously been achieved for cryogenic-temperature  $\bar{p}$  plasmas. In a Boltzmann energy distribution for an antiproton temperature  $T_p$  substantially higher than our Ioffe trap depth of 0.4 K, the number of antiprotons with energy less than this trap depth is proportionate to  $T_p^{-3/2}$ . The cooling demonstrated in this chapter, from roughly 30 K to 3.5 K, increases the number of sufficiently low-energy  $\bar{p}$  by a factor of 25, and further improvements seem attainable. Much of the work presented in this chapter has been published in Ref. [103].

## 6.1 Embedded-Electron Cooling

In all  $\bar{p}$  plasma and antihydrogen experiments to date, the energetic  $\bar{p}$  loaded into a trap are sympathetically cooled by simultaneously trapped electrons [34, 114]. During this process, the electron cyclotron energy damps by synchrotron radiation at

a rate given by

$$\gamma_e = \frac{q^2 \omega_c^2}{3\pi \epsilon_0 m_e c^3} \quad (6.1)$$

For the magnetic field  $B = 3.7$  T used in the experiments discussed below, the electron cyclotron frequency  $\omega_c = qB/m$  results in a cooling rate  $\gamma_e = 5$  Hz. For electron motion other than the cyclotron orbit, as well as antiproton motion, acceleration is much too small for a significant radiative cooling rate. Instead, collisions provide the necessary coupling to bring the two-component plasma into equilibrium with the trap environment.

This standard electron-cooling procedure, however, leaves an important challenge in removing the electrons. The typical method is to remove the trap potential for a brief time, during which the electrons accelerate out of the trap while the much more massive  $\bar{p}$  are unable to leave. The sudden removal of the  $10^8$   $e^-$  typically used to load  $\bar{p}$ , however, changes the space-charge potential by tens of volts and results in a substantial heating of the  $\bar{p}$ .

The key idea studied here is that very few  $e^-$  may be left with the  $\bar{p}$  and these  $e^-$  provide for the removal of energy incurred during electron ejection and subsequent trap manipulations, such as transferring the plasma to a different location. In a standard antiproton-electron plasma realized for electron-cooling, the  $e^-$  account for 99% of the plasma and the  $\bar{p}$  reside in a thin shell surrounding a core of  $e^-$  due to centrifugal separation (see Chapter 8). In contrast, the antiproton-electron plasmas investigated below contain only 0.2% to 1%  $e^-$ , which are evenly distributed throughout. To distinguish these qualitatively different plasmas, we describe these relatively few  $e^-$  as embedded in the  $\bar{p}$  plasma.



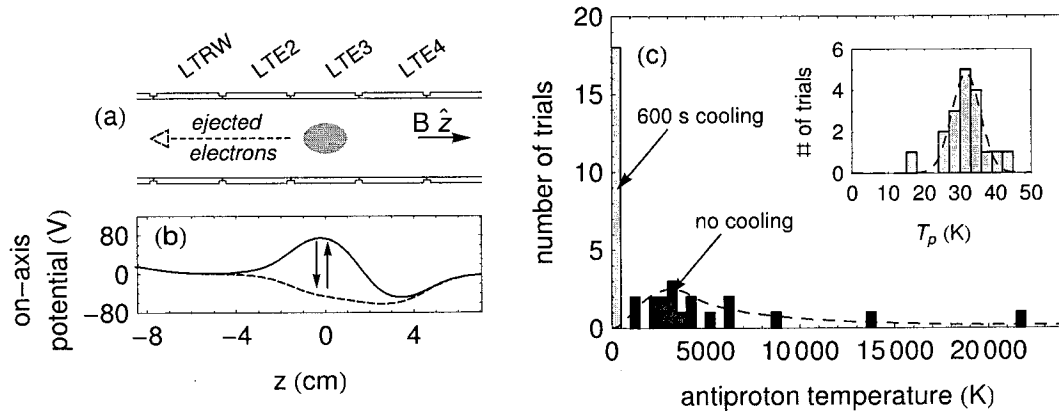


Figure 6.1: (a) Electrons are ejected from an antiprotons plasma shown within the trap electrodes. (b) On-axis trap potentials used to eject electrons. (c) The elevated antiproton temperature immediately after the ejection (black) is greatly reduced after 600 s by embedded-electron cooling (gray, inset).

A first demonstration of embedded-electron cooling begins by loading  $5 \times 10^5 \bar{p}$  with  $1.0 \times 10^8 e^-$  (by methods in Section 2.2). For these studies, the initial loading  $e^-$  are removed as shown in Fig. 6.1a. The antiproton-electron plasma is held in a potential well formed by applying 60 V to electrode LTE3. A sequence of four square-pulses each remove the confining potential for a brief duration of 50 ns, with consecutive pulses separated by approximately 1 s. A quick estimate demonstrates that electrons are ejected much more readily than antiprotons: in 50 ns, an electric field of 1 V/cm will move an electron 2 cm, while a much more massive antiproton will only move  $10 \mu\text{m}$ . For the first two pulses, the number of ejected  $e^-$  that strike the degrader is sufficient to be detected with standard charge-counting methods (see Section 2.3.2).

The  $\bar{p}$  temperature approximately 3 s after the  $e^-$  ejection is thousands of Kelvin, as shown in Fig. 6.1b. The large variance in these initial temperatures, likely due

to fluctuations in the delay between  $e^-$  ejection and the temperature measurement, is not important for this demonstration. If a 600 s delay is introduced before the measurement, however, the  $\bar{p}$  temperature is  $31 \pm 6$  K (see figure inset). Cooling by embedded  $e^-$  has reduced the temperature by two orders of magnitude. We'll take a closer look at this process below.

### 6.1.1 Temperature Rate Equations

During embedded-electron cooling, the temperatures  $T_p$  and  $T_e$  of  $N_p$  antiprotons and  $N_e$  electrons, respectively, are described by the coupled rate equations

$$\frac{d}{dt}T_p = \frac{N_e}{N_p}\gamma_{ep}(T_e - T_p) \quad (6.2a)$$

$$\frac{d}{dt}T_e = -\gamma_{ep}(T_e - T_p) - \gamma_e(T_e - T_t) \quad (6.2b)$$

The effective trap temperature  $T_t$  corresponds to the steady-state temperature reached by the plasma. It is determined by blackbody radiation from the trap electrodes along with any electrical noise that heats the  $e^-$  directly.

While the electrodes are cooled to 1.3 K by a pumped helium system (Section 2.1), we measure  $T_t$  to be substantially higher (31 K above, improved to 17 K below). As discussed below, the more than fifty high-bandwidth electrical lines that allow for versatile use of our Penning trap present a considerable challenge to reducing  $T_t$ .

The electron-antiproton equilibration rate  $\gamma_{ep}$  results from collisions between the two species. Following Ref. [99], we generalize the expression introduced in Section 5.1 for collisions between different species. The predicted rate is

$$\gamma_{ep} = \frac{n_p q^4 \ln \Lambda_B}{3\sqrt{2}\pi^{3/2}\epsilon_0^2 m_p m_e} \left( \frac{kT_p}{m_p} + \frac{kT_e}{m_e} \right)^{-3/2} \quad (6.3)$$

where the generalized Coulomb logarithm  $\ln \Lambda_B$  encapsulates magnetic-field effects [100], as discussed in Section 5.1.

For  $\bar{p}$  plasmas studied in the following section with density  $n_p = 4 \times 10^7 \text{ cm}^{-3}$  and  $T_p = 5$  to 30 K the equilibration rate varies from  $\gamma_{ep} = 2$  to 30 kHz. Since  $\gamma_{ep} \gg \gamma_e$ , the temperature evolution described by Eq. 6.2 simplifies. Within the short time frame of  $(\gamma_{ep})^{-1}$ ,  $T_e$  changes to match  $T_p$ . After that point, the  $\bar{p}$  temperature follows

$$\frac{d}{dt}T_p \approx -\frac{N_e}{N_p}\gamma_e(T_e - T_i) = \gamma_p(T_e - T_i) \quad (6.4)$$

where the effective  $\bar{p}$  damping rate is

$$\gamma_p = \gamma_e N_e / N_p \quad (6.5)$$

The rate  $\gamma_p$  is slower than  $\gamma_e$  due to the large number of  $\bar{p}$  that must be cooled along with the  $e^-$ . Note that this simplification of Eq. 6.2 is not valid at much lower  $\bar{p}$  densities or higher temperatures where  $\gamma_{ep}$  may be less than  $\gamma_e$ .

### 6.1.2 Counting Embedded Electrons

To investigate the thermal equilibration of  $\bar{p}$  described by Eq. 6.4, we prepare  $5 \times 10^5 \bar{p}$  at 4 K by adiabatic cooling (to be discussed in Section 6.2). In Fig. 6.2, the exponential return to the equilibrium temperature  $T_t = 26$  K is found by measuring  $T_p$  after a varied delay. Experiments are performed with three and four of the initial electron-ejection pulses shown in Fig. 6.1a. The resulting number of  $e^-$  for these two procedures is determined to be  $N_e = 6000$  and 900 from the measured  $\gamma_p = 61 \pm 6$  mHz and  $9.7 \pm 0.7$  mHz. Notably, this equilibration rate measurement provides an  $e^-$  count

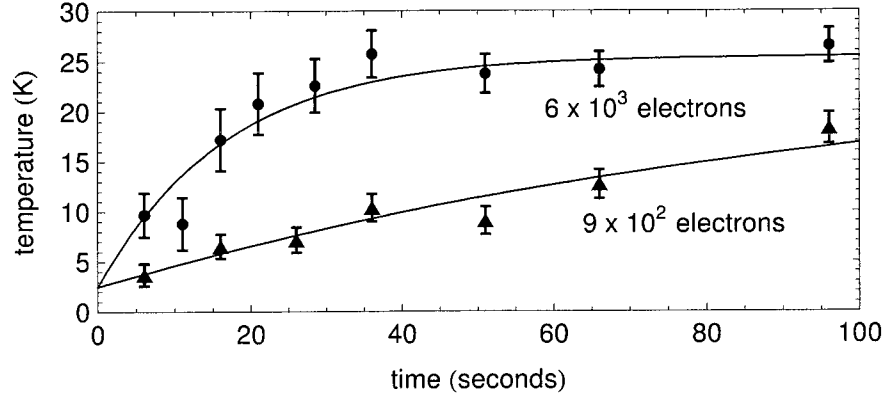


Figure 6.2: The equilibration of antiproton plasmas prepared with three (circles) and four (triangles) electron-ejection pulses. The measured equilibration rate reveals the number of embedded electrons. From Ref. [103].

with much greater sensitivity to small number of particles than is possible with typical charge counting. Using this method, electron-ejection procedures may be developed to prepare plasmas with any desired number of embedded electrons.

## 6.2 Adiabatic Cooling

Adiabatic cooling occurs when the plasma expands axially as the restoring force from the trap potential  $\phi_t \approx (2m_p\pi^2 f^2/q)(z^2 - \rho^2/2)$  is gradually reduced. For simplicity, in this section we will characterize the trap potential by the  $\bar{p}$  axial frequency, denoted  $f$ . Just as an expanding gas does work against a retracting piston, the expanding plasma does work against the diminishing trap restoring force. Adiabatic cooling is observed as a  $\bar{p}$  plasma with initial temperature  $T_i$  with axial frequency  $f_i$  cools to a temperature  $T_f$  when the frequency is gradually reduced to  $f_f$ .

We begin with a plasma with  $N_p = 5 \times 10^5$ ,  $N_e = 6000$ , and  $r_p = 2$  mm loaded into the potential structure used for temperature measurements, shown in Fig. 5.1.

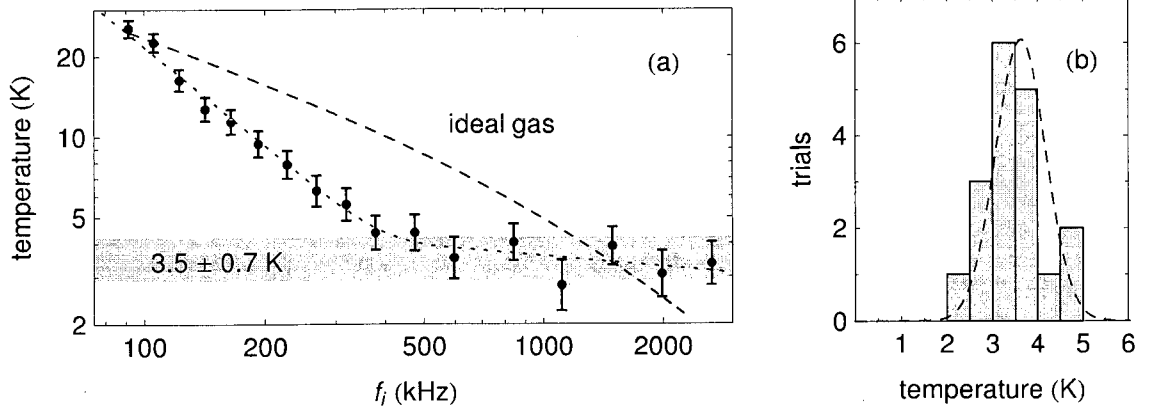


Figure 6.3: (a) Temperature of antiprotons after adiabatic cooling from an initial trap potential given by  $f_i$ . Adapted from Ref.[103]. (b) Repeated trials with  $f_i = 600$  kHz show  $T_p = 3.5 \pm 0.7$ .

The initial frequency  $f_i$  is chosen between 3 MHz and 90 kHz by varying the voltage applied to electrode LTE2 between 1000 and 0.5 V. Thermal equilibrium at  $T_t$  is established as the plasma is left in this initial well for a time much longer than  $(\gamma_{ep})^{-1}$ . The trap frequency is then reduced in hundreds of milliseconds to  $f_f$ , corresponding to a well depth just sufficient to confine the plasma. The plasma temperature is subsequently measured in the standard way by continuing to reduce the well depth and recording particle loss (see Section 5.1). The expansion and measurement occur in a time much shorter than  $(\gamma_{ep})^{-1}$  so embedded-electron cooling has minimal effect during the adiabatic cooling and measurement. Figure 6.3 shows the measured  $T_p$  resulting from expansion determined by the initial trap frequency  $f_i$ . The reported uncertainties arise from the variance observed in repeated trials.

In the low-temperature limit, adiabatic expansion of a weakly correlated plasma is expected to be that of an ideal gas [55]. The resulting temperature is given by

$$T_f = (V_i/V_f)^{2/3} T_i \quad (6.6)$$

where  $V_i$  and  $V_f$  are the initial and final volumes of the plasma. The validity of this approximation relies on two assumptions: the average energy stored in the interaction between neighboring particles can be neglected and the potential energy is constant throughout the plasma, as viewed in the rest frame of the plasma. Inter-particle interactions are characterized by the correlation parameter  $\Gamma = q^2/(4\pi\epsilon_0 akT)$  where the Wigner-Seitz radius  $a$  is the typical particle spacing, with  $4\pi a^3 n/3 = 1$ . The correlation parameter is just the ratio of the typical nearest-neighbor Coulomb energy to the thermal energy. Antiproton plasmas in this study are weakly correlated with  $\Gamma = 0.01$  to  $0.1$ .

The second assumption is valid except within a Debye length  $\lambda_D$  of the plasma edge, where the external potential is not fully screened. For  $\bar{p}$  plasmas considered here, however,  $\lambda_D = 0.05$  to  $0.3$  mm. A relatively large  $\lambda_D$  results from the substantial decrease in density during the expansion, since  $\lambda_D \propto n^{-1/2}$ . Consequently, the boundary region can account for as much as 30% of the plasma volume. As a result, the cooling predicted by Eq. 6.6 does not describe perfectly the cooling observed in Fig. 6.3. For small  $f_i$ , the observed cooling is more effective than predicted for an ideal gas. The gain at larger  $f_i$ , however, diminishes to the extent that the  $T_p$  measured for  $f_i > 500$  kHz are consistent with no additional cooling beyond  $T_p = 3.5$  K. This same limit is reached when the number of  $\bar{p}$  and initial temperature are varied:  $N_p = 2 \times 10^5$  to  $3 \times 10^6$  and  $T_i = 35$  to  $17$  K. It remains to be seen whether a more sophisticated cooling model incorporating the non-ideal boundary layer predicts this behavior or whether a technical limit to the temperature measurement method prevents lower measurements (discussed in Section 5.1).

The observed cooling is unchanged when the expansion rate is reduced by a factor of five, as expected for a process that is both adiabatic and reversible. Thermodynamic adiabaticity is achieved since the expansion time is fast compared to the rate of heat transfer  $\gamma_{ep}$ . Reversibility, which is required for maximal cooling, means that the plasma remains in an equilibrium state. This is achieved since the expansion occurs on a time scale much longer than those associated with relevant internal dynamics of the plasma. For example, since the center-of-mass oscillation frequency changes very little in one period,  $\dot{f}/f^2 \ll 1$ , the change in external potential does not cause non-equilibrium displacements in the center-of-mass.

### 6.3 Discussion

The above studies demonstrate a general two-stage procedure to produce cold  $\bar{p}$  for antihydrogen ( $\bar{H}$ ) experiments. After an electron-ejection procedure leaves a desired number of embedded  $e^-$  in the  $\bar{p}$  plasma, the plasma is moved to a desired location and trapped in a compressed state with a strong trapping potential. The  $\bar{p}$  are held for a sufficient time to come to equilibrium via embedded-electron cooling. In a second cooling stage, adiabatic cooling proceeds by reducing the trap potentials to the minimum required for the desired application. If desired, a third cooling stage employing forced evaporation [97, 104] could follow to reduce the temperature further at the cost of a decrease in the number of  $\bar{p}$ .

Note that any cooling achieved beyond embedded-electron cooling is lost as the plasma re-equilibrates via  $e^-$  synchrotron radiation. Therefore, the number of embedded  $e^-$  must be chosen so that this time is sufficient for the intended application.

One important example is the production of  $\bar{H}$  by charge exchange with Rydberg positronium [93]. The production of trappable  $\bar{H}$  should benefit greatly from cold  $\bar{p}$  since the kinetic energy of the  $\bar{H}$  formed is directly tied to that of the trapped  $\bar{p}$ . The typical duration of a charge exchange experiments so far has been roughly one hour, a time dictated by the optimal operation of the cesium source [48]. For this application, a small fraction of  $e^-$  should be used:  $N_e = 2000$  and  $N_p = 5 \times 10^6$  in  $B = 1$  T gives  $(\gamma_p)^{-1} = 2$  h . Note that as a consequence of this approach, the initial embedded-electron cooling must take longer than the application.

An important finding of these cooling studies is that the effective trap temperature  $T_t$  is higher than that of the 1.3-K trap electrodes. The steady-state temperature is found to be independent of the ratio  $N_e/N_p$ , suggesting that the undesired heating mechanism couples only to  $e^-$ , as modeled in Eq. 6.2. An effort to improve electrical shielding and filtering of the trap reduced  $T_t$  from 31 to 17 K when the high-voltage antiproton-catching electronics were removed. Continued technical improvements should be able to further reduce  $T_t$ , although a substantial challenge is present by the over fifty high-bandwidth electrical lines used to control our versatile stack of electrodes. Furthermore, the space-charge of the antiprotons broadens electron resonances that may be driven by this noise.

A possible limit to embedded-electron cooling may result from the decoupling of  $e^-$  cyclotron and axial energies at low temperatures, discussed in Section 5.2.3. Reference [96], for example, predicts that the equilibration of the cyclotron and axial motions in an  $e^-$  plasma with  $n = 5 \times 10^7 \text{ cm}^{-3}$  and  $B = 3.7$  T to occur at a rate that decreases from 500 Hz at 20 K to 0.01 Hz at 5 K. For embedded-electron cooling, such



a decoupling should effectively decrease  $\gamma_p$  at low temperature. However, this is not apparent in Fig. 6.2 in which the observed heating fits a single exponential. To be cautious, this theoretical calculation has yet to be tested this far into the magnetized regime [112]. Moreover, other mechanisms may contribute to the equilibration rate [113]. Speculatively, however, there may be an advantage to this possible limitation. Consider a  $\bar{p}$  plasma cooled by adiabatic expansion well beyond the limits of embedded-electron cooling, as determined by decoupling of the  $e^-$  cyclotron motion. As a consequence of this decoupling, re-equilibration is impeded, and the  $\bar{p}$  will remain at the low temperature for a very long time.

## Chapter 7

# Improved Particle Accumulation: $10^7$ Antiprotons and $10^9$ Positrons

A central focus of current antihydrogen ( $\bar{\text{H}}$ ) research is to increase the number of atoms that can be loaded into a magnetic trap for laser-cooling and precise spectroscopy. This may be achieved by either increasing the number of antiprotons ( $\bar{\text{p}}$ ) and positrons ( $\text{e}^+$ ) used to form  $\bar{\text{H}}$  or increasing the efficiency with which trappable atoms are produced. In the present chapter, we present progress towards the former approach. With improved methods, we accumulate up to 10 million  $\bar{\text{p}}$  in a 1-T magnetic field. This is a 14-fold increase over our previous methods [49], equaling the largest numbers accumulated with much slower  $\bar{\text{p}}$  from a radio-frequency quadrupole decelerator [115]. Additionally, we trap up to 4 billion  $\text{e}^+$ , a 20-fold increase over our previous methods [49].

These improved loading procedures have already been incorporated in ongoing studies of  $\bar{\text{H}}$  production via two-stage charge exchange, resulting in a factor of 200

increase in  $\bar{\text{H}}$  yield from previous efforts [48, 93]. We are also currently working to incorporate these new methods in  $\bar{\text{H}}$  production by three-body recombination in a nested well [41]. A very recent experiment optimized for detecting small numbers of trapped atoms used this production scheme to achieve an average of 1 atom trapped per trial, demonstrating an efficiency  $6 \times 10^{-5}$  [45] trapped  $\bar{\text{H}}$  per  $\bar{\text{p}}$ . With the number of  $\bar{\text{p}}$  now available in the ATRAP apparatus, this efficiency would correspond to 700 trapped atoms.

## 7.1 Improved Antiproton Accumulation

Following a brief review of the standard techniques used to accumulate antiprotons, we demonstrate a large gain in capture efficiency when the magnetic field is increased by a new solenoid installed for this purpose. To load these antiprotons into a trap at the reduced field of 1 T, as desired for antihydrogen experiments, the rotating-wall technique (Section 4.3) compresses the antiprotons to avoid loss due to their expansion in the decreasing field.

The established methods we use to accumulate low-energy  $\bar{\text{p}}$  in a trap were introduced in Section 2.2.2 and are extensively reviewed in Ref. [114]. In particular, we slow  $\bar{\text{p}}$  in matter [32], catch them by pulsed trap potentials [33], and sympathetically cool them with co-trapped electrons [34]. Multiple injection bunches are accumulated in a process commonly called stacking [116]. Antiproton accumulation in the apparatus used in this work is described further in Ref. [49].

Antiproton accumulation begins by loading a plasma of  $N_e = 10^8$  electrons with radius  $r_p = 6$  mm in a trap potential produced by applying 100 V to electrode LTE3,

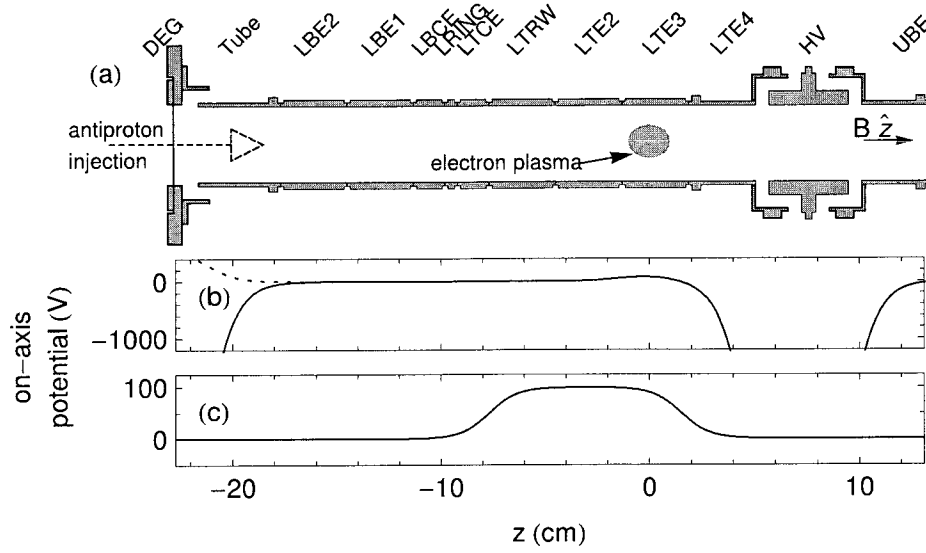


Figure 7.1: (b) Electron-antiproton plasma located within a cross-section of the trap electrodes during the  $\bar{p}$  loading procedure. (b) Trap potentials to accept (dashed) and trap (solid) injected  $\bar{p}$  bunches. (c) Potential applied during the rotating-wall procedure.

as shown in Fig. 7.1a. The ATRAP apparatus receives a 200-ns bunch of 30 million  $\bar{p}$  at 5.3 MeV every 110 seconds from the Antiproton Decelerator. To catch an  $\bar{p}$  injection, -5 kV is applied to the electrode HV, while the degrader foil DEG is held at 600 V (shown dashed in Fig. 7.1b). After the  $\bar{p}$  bunch passes through the foil, the foil voltage is rapidly switched to -5 kV (shown solid) in a time much shorter than required for the  $\bar{p}$  to return and escape. Trapped  $\bar{p}$  cool by collisions with the electrons over many passes through the long catching well. Eventually the resulting electron-antiproton plasma reaches equilibrium. During this process, the electrons cool by synchrotron radiation, as discussed in Section 6.1. The  $\bar{p}$  thermalize before the next bunch of  $\bar{p}$  arrives, so the loading technique may be repeated to stack subsequent  $\bar{p}$  bunches.

An antiproton is captured only if it has sufficiently low energy after it passes

through the degrader foil. In particular, the energy along the magnetic field  $E_z$  must be smaller than the applied potentials,  $E_z < 5 \text{ keV}$ . In addition, the energy perpendicular to the magnetic field  $E_c$  must correspond to a cyclotron orbit with a radius  $r_c = \sqrt{2E_c m_p}/qB$  that fits within the 18-mm-radius trap electrodes.

The initial  $\bar{p}$  energy and alignment is adjusted to optimize the number of  $\bar{p}$  captured, as determined by these requirements. While most of a  $\bar{p}$ 's initial 5.3 MeV of energy is lost as it passes through the degrader, a 125- $\mu\text{m}$ -thick foil of Be, tuning the  $\bar{p}$  energy prior to this foil is made possible by a He-SF<sub>6</sub> gas cell. The difference in the energy lost in 1-atm of SF<sub>6</sub> rather than He results in a tuning range of approximately 600 keV. To align the incoming  $\bar{p}$  with the trap axis, the beam position and focus is adjusted with dipole and quadrupole beam-line magnets. The incident beam waist is found to be smaller than 2 mm by imaging with a parallel plate ionization chamber just below the tuning cell [49].

### 7.1.1 Increased Magnetic Fields

The slowing of  $\bar{p}$  in matter by inelastic collisions with electrons is a stochastic process. Consequently, the  $\bar{p}$  that emerge from the degrader have parallel and perpendicular energy distributions much broader than the range trapped by achievable trap fields, which are limited in practice by superconducting magnet and fast high-voltage switch technology. Moreover, for  $\bar{H}$  trapping experiments, the magnetic field is further restricted by a desire for a deep Ioffe trap potential. As discussed in Chapter 3, the radial magnetic trap is diminished by the uniform axial magnetic field, due to the addition of orthogonal field vectors. Throughout this thesis, we choose

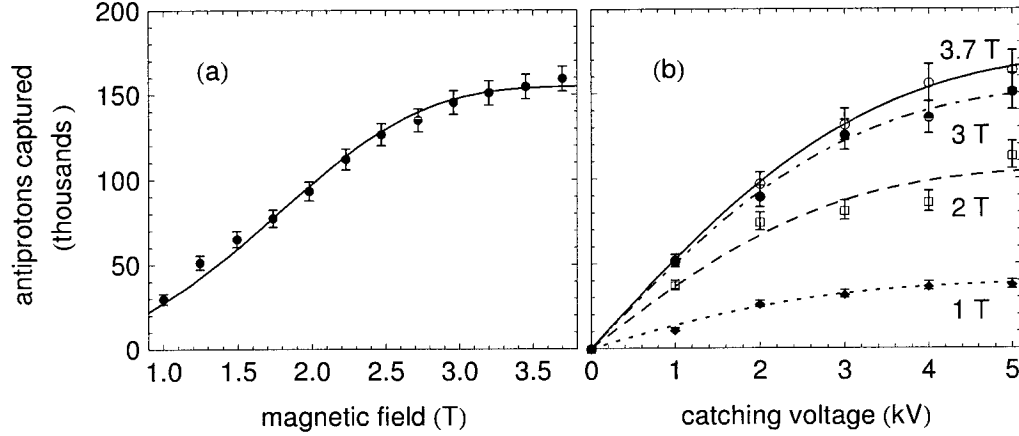


Figure 7.2: Number of antiprotons trapped from one injection as a function of (a) magnetic field with a catching voltage of 5 keV and (b) catching voltage for the specified magnetic fields.

a compromise of a 1-T Penning-trap field which still provides sufficient  $e^-$  and  $e^+$  synchrotron cooling rates.

The substantial gain in  $\bar{p}$  catching at larger magnetic fields is shown in Fig. 7.2. At  $B = 3.7$  T, for example,  $160 \times 10^3$   $\bar{p}$  are caught, whereas at  $B = 1$  T this number is reduced to  $30 \times 10^3$ . For these experiments, a 1-T field is generated by the primary ATRAP solenoid, and additional field over the  $\bar{p}$  catching region is provided by a secondary antiproton-loading solenoid (shown in Fig. 2.2). This new solenoid can generate a greater magnetic field than the primary solenoid, and it is more convenient to adjust due to its relatively small inductance. Further details regarding the design and operation of the antiproton-loading solenoid are provided in Ref. [48].

The challenge presented by loading  $\bar{p}$  with  $B = 3.7$  T and subsequently reducing the field to 1 T, is illustrated in Section 4.2.2. As the magnetic field is reduced, the trapped plasma expands radially so that to a good approximation  $B\langle r^2 \rangle$  is constant, as dictated by angular momentum conservation. In Chapter 8, this effect is used to

study centrifugal separation in electron-antiproton plasmas by recording the magnetic field at which  $\bar{p}$  strike the electrode surface and annihilate. For  $\bar{p}$  loading, however, this effect completely negates the original gains from the increased magnetic field.

Before moving on, we should note an important feature of the data shown in Fig. 7.2. The increase in  $\bar{p}$  yield for additional increases in magnetic field or trap voltages appears marginal, even though the best efficiency demonstrated here traps only 0.5% of the incident  $\bar{p}$ . This is likely a consequence of axial energy  $E_z$  and cyclotron energy  $E_c$  distributions that are not independent. Each curve shown in Fig. 7.2 results from a fit to a Gaussian energy distribution. Correlations between  $E_z$  and  $E_c$  are observed in Fig. 7.2b, where it is found that the width of the parallel energy distribution increases 15% when  $B = 3.7$  T rather than  $B = 1$  T. It is likely, then, that further increases in both the magnetic field and trap voltage, if feasible, would result in gains larger than is at first apparent from these data.

### 7.1.2 Compression of Antiprotons by a Rotating Wall

To compensate for expansion caused by reduction of the magnetic field, the electron-antiproton plasma is compressed by the rotating-wall technique discussed in Section 4.3. As before, we begin with a plasma of  $10^8$  electrons with  $r_p = 6$  mm in  $B = 3.7$  T. A desired number of  $\bar{p}$  bunches is then stacked [116]. Figure 7.3 shows the resulting linear accumulation of up to 10.5 million  $\bar{p}$  in 90 minutes. The rotating-wall procedure begins with a dipole rotating-wall drive with a frequency of 1 MHz and peak-to-peak amplitude of 2.2 V on the nearby segmented electrode LTRW. The plasma is adiabatically moved from electrode LTE3 to LTE2 (method in Section 2.3.1)

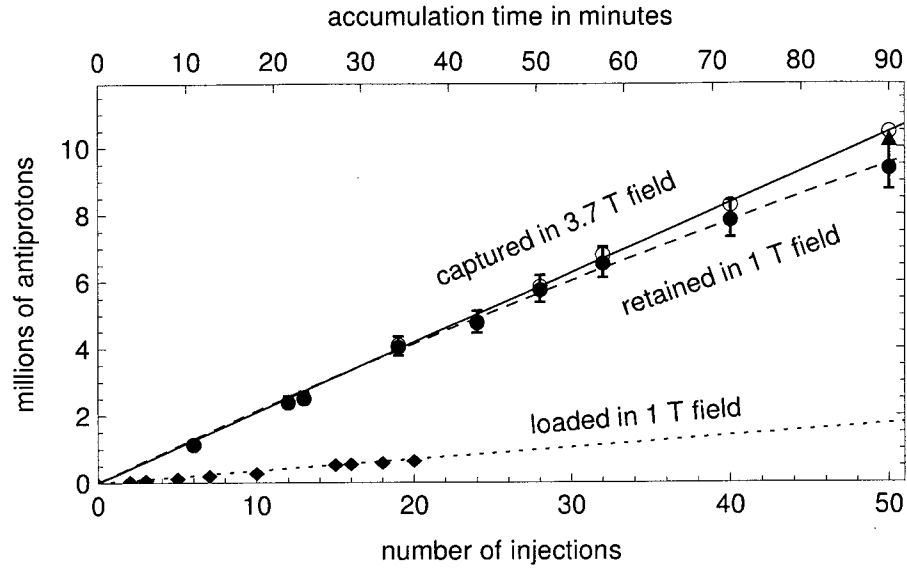


Figure 7.3: Antiprotons captured from the specified number of injections in  $B = 3.7$  T (empty circles) and retained after the field is reduced to  $B = 1$  T (filled circles). A more gradual rotating-wall procedure, discussed in the text, reduces the loss at 1-T observed for the largest load (triangle). Antiprotons captured in  $B = 1$  T (diamonds) are accumulated at a rate 5-times smaller.

and then the trap potential is gradually expanded over 250 s to the three-electrode flat well shown in Fig. 7.1c. The rotating wall drive continues for 1000 s before the plasma is returned to its initial location in 30 s and the rotating wall drive is turned off. The resulting plasma has a radius  $r_p = 2$  mm, as determined by electron mode frequencies (methods in Section 4.2). The electrons are then ejected (by methods in Section 6.1), and the magnetic field is reduced to  $B = 1$  T with minimal losses.

Figure 7.3 shows that the accumulation of up to  $1.0 \times 10^7$   $\bar{p}$  in a 1-T field by this method is nearly linear with the number of  $\bar{p}$  bunches stacked. The loading rate is a factor of 5 higher than that achieved by stacking at  $B = 1$  T, allowing for a much larger number of particle to be accumulated without substantially increasing the duration of



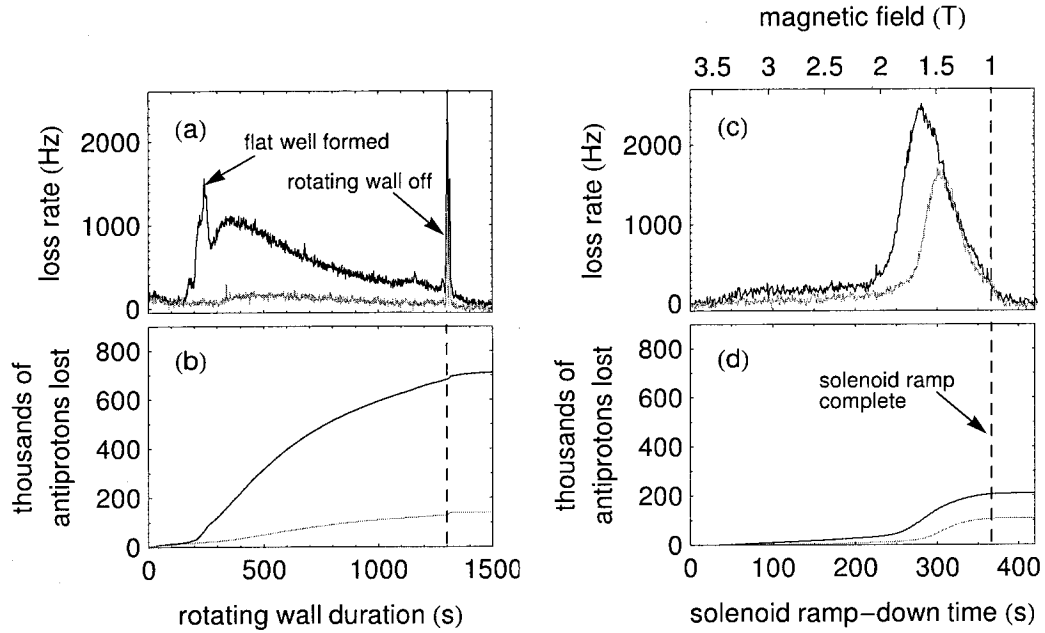


Figure 7.4: Antiproton loss rate and integrated losses for loads of 10 million (black) and 7 million (gray) particles during (a,b) the 1300s rotating-wall procedure and (c,d) the subsequent reduction in magnetic field.

an experiment. For the largest loads of 50 injection, loss-free accumulation is achieved with a reduced drive amplitude of 1.3 V applied for twice the typical duration.

The slight fractional losses due to the rotating wall and field reduction with the 1300s rotating-wall procedure described are shown in Fig. 7.4. These losses increase with the number of  $\bar{p}$ , and for the largest stack of  $10.5 \times 10^6$   $\bar{p}$  in  $B = 3.7$  T, approximately 10% are lost in these steps. Additionally, greater losses are observed for an increase in the rotating-wall drive amplitude or the rate at which the rotating wall trap potential is formed. These losses are not yet understood and are a subject for further study. One promising route to develop a faster and lower-loss procedure is to implement a multi-electrode harmonic well during the rotating wall, as discussed in Section 4.3. It should be noted that in previous demonstrations of compression

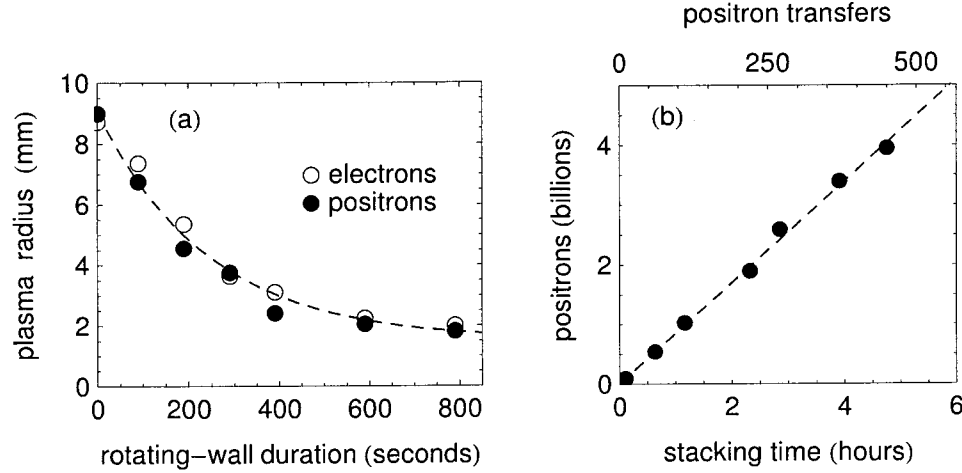


Figure 7.5: (a) Rotating wall demonstration in the positron-loading trap region with positrons (filled circles) and electrons (empty circles). (b) Linear accumulation of  $4 \times 10^9$  positrons with 450 transfers over 5 hours.

of antiproton-electron plasmas with a rotating wall, losses over 50% are reported for experiments with  $3 \times 10^4$  and  $5 \times 10^5$   $\bar{p}$  [117, 118].

Intriguingly, Fig. 7.3c-d shows that even though the magnetic field changes at a constant rate, the  $\bar{p}$  loss rate slows before this process is completed. Since most of the  $\bar{p}$  remain trapped, this suggests that the  $\bar{p}$  are not in a smooth equilibrium distribution. One possible explanation is that the  $\bar{p}$  geometry does not follow that of the electrons if the compression is too rapid, an effect that has been previously noticed [117]. In this case, some  $\bar{p}$  are stranded in a non-equilibrium distribution in which the time scale for radius-changing collisions is too long for re-equilibration.

## 7.2 Improved Positron Accumulation

In this section, we briefly report the use of the rotating-wall technique to load up to  $4 \times 10^9$   $e^+$ , a 20-fold improvement in linear accumulation for our apparatus [49]. The

methods used to load  $e^+$  in the ATRAP apparatus were introduced in Section 2.2.3 and are described in detail in Ref. [49]. Positrons are injected into the trap in short bunches of 5 to 10 million  $e^+$  that are caught by pulsed voltages, an approach similar to catching  $\bar{p}$ . Injections are typically repeated every 30-50 s, which allows sufficient cooling time for consecutive injections to be stacked. In our previous studies, loss-free accumulation has only been achieved for up to  $2 \times 10^8$   $e^+$ , due to radial expansion of the trapped plasmas [49]. Expansion of the plasma is caused by both misalignment of injected  $e^+$  with the trap axis and drag due to trap asymmetries (see discussion in Section 4.3). Notably, Ref. [48] measures an expansion rate as large as 0.01 mm/s for some electron plasmas in the ATRAP apparatus in trap potentials similar to those used during  $e^+$  loading. The expansion rates are expected to depend on the plasma radius and density, however, and a detailed study has not been undertaken. To mitigate radial expansion, a rotating-wall drive is intermittently applied during long  $e^+$  loading procedures. In Fig. 7.5a the compression of  $e^-$  and  $e^+$  plasmas are compared in implementing the methods of Section 4.3 in the positron-loading region of the trap. In Fig. 7.5b, this rotating-wall procedure was used to compress the plasma to approximately 3 mm every 50 transfers. As a result, the linear loading of  $4 \times 10^9$   $e^+$  is achieved, a 20-fold improvement for our apparatus.

This demonstration of trapping 4 billion  $e^+$  marks a substantial increase in the number of  $e^+$  available for  $\bar{H}$  experiments. In contrast to increased  $\bar{p}$  accumulation, which is expected to correspond to a proportionate increase in  $\bar{H}$  production, however, the gains from more  $e^+$  will depend on the application. For the synthesis of  $\bar{H}$  by a two-stage charge-exchange reaction (see Section 1.3), the number of  $\bar{H}$  produced should

be proportionate to the number of  $e^+$  available, since only a very small fraction of the  $\bar{p}$  available undergo charge-exchange collisions. This is true up to a limit at which the  $e^+$  space-charge electric field is large enough to Stark-ionize the incoming Rydberg Cs beam. For recent experiments, this limit was approximately 0.5 billion  $e^+$  [48], although it may possibly be increased by lengthening the  $e^+$  trap region or decreasing the Rydberg energy level.

In the case of  $\bar{H}$  formation by three-body recombination in a nested well (see Section 3.2) an increase in the number of  $e^+$  will beneficially increase the number of antiproton-positron and antihydrogen-positron collisions that thermalize  $\bar{p}$  and  $\bar{H}$  velocities, and form and de-excite  $\bar{H}$  (see for example Ref. [94]). On the other hand, a potential restriction on the number of usable  $e^+$  arises from the fast rotational velocities in large and dense  $e^+$  plasmas [119]. From Eq. 4.2, the  $\vec{E} \times \vec{B}$  drift velocity of a  $\bar{p}$  that enters a  $e^+$  plasma at radius  $\rho$  is  $v_\theta = \rho\omega_r \propto \rho n_{e^+}$ . Note that this velocity is greatly increased from that in an empty trap (the magnetron velocity [63]) due to the  $e^+$  space-charge electric field. For example, a plasma of  $5 \times 10^7$   $e^+$  with a radius of 5 mm would have a rotational frequency  $\omega_r/2\pi \approx 20$  kHz in the nested-well trap potential shown in Fig. 3.4 and a 2-T axial magnetic field. The corresponding rotational kinetic energy of a  $\bar{p}$  is greater than the 400 mK Ioffe trap depth for ground-state  $\bar{H}$  if it has a radial position  $\rho > 0.7$  mm. It therefore seems that profitably increasing the number of  $e^+$  in nested-well experiments requires that antihydrogen-positron collisions are able to slow  $\bar{H}$  atoms before they escape the  $e^+$  plasma.

## Chapter 8

# Centrifugal Separation of Antiprotons and Electrons

Particles in a Penning trap experience a centrifugal force associated with their rotation about the trap axis. As in a centrifuge, where a mixture is separated into components of different densities, a multi-species trapped plasma will separate by mass at sufficiently low temperature [120]. Centrifugal separation in a two-component plasma was first demonstrated when laser-cooled ions were used to sympathetically cool a second ion species [121]. More recent studies with laser-cooled ions have demonstrated complete separation in ion-ion [122, 123] and ion-positron [124] plasmas. This chapter presents the observation of centrifugal separation in antiproton-electron plasmas, the first such demonstration with particles that cannot be laser-cooled or optically imaged [125].

Electron-antiproton plasmas are realized in all cold antiproton experiments, since the collisional cooling of antiprotons by electrons is the only method yet used to cool

antiprotons to cryogenic temperatures [34, 114]. The spatially-separated plasmas shown here are typical plasma geometries after the electron-cooling of antiprotons. This separation is critical to understanding the pulsed ejection of electrons from electron-antiproton plasmas, as is typically done before antihydrogen formation. The initial antiproton geometry dictates the equilibrium radial distribution realized after electrons are removed, which is an important parameter in antihydrogen-trapping experiments (Chapter 3). For example, the geometry of an antiproton plasma affects its confinement in a Penning-Ioffe trap (Section 3.1), and the radius with which an antiproton enters a positron plasma determines the rotational velocity it acquires (Section 7.2). Additionally, the separation provides an alternate, gradual method to remove some electrons by taking advantage of radial dependence of the axial trap potential.

## 8.1 Density Distribution and Separation Temperature

The density distribution of an uncorrelated pure electron plasma

$$n_e(\rho, z) = n_e \exp \left[ -\frac{1}{kT} \left( q\phi(\rho, z) + \frac{qB\omega_r\rho^2}{2c} - \frac{m_e\omega_r^2\rho^2}{2} \right) \right] \quad (8.1)$$

depends upon its central density  $n_e$ , temperature  $T$ , and rotation frequency  $\omega_r$  [55] (see also Section 4.1). The first term in the exponential describes the interaction with the total electric potential  $\phi(\rho, z)$ , which includes both the external trap potential and space-charge potential. The second term is the potential due to rotation through the magnetic field, and the third term is the centrifugal potential.

In an electron-antiproton plasma, each component has a density distribution of this same form, but the space-charge potential includes contributions from both species. In the case of a relatively few antiprotons, however, the total space-charge potential is to a good approximation due to only the electrons. Therefore, the electron distribution is unchanged and the antiproton distribution

$$n_p(\rho, z) \propto n_e(\rho, z) \exp \left[ \frac{1}{kT} \frac{(m_p - m_e) \omega_r^2 \rho^2}{2} \right] \quad (8.2)$$

differs only due to the increased centrifugal potential. Separation of antiprotons from the electrons becomes pronounced when differences in centrifugal potential energy between the two species are larger than the thermal energy. This is expected for temperatures greater than

$$T_{\text{sep}} \equiv \frac{m_p \omega_r^2 r_p^2}{2k} \approx \frac{m_p q^2}{8\epsilon_0^2 k} \left( \frac{n_e r_p}{B} \right)^2 \quad (8.3)$$

where  $r_p$  is the radius of the electron plasma and the rightmost expression uses the good approximation  $\omega_r \approx qn/(2\epsilon_0 B) \ll \omega_c$  (see Eq. 4.2). In a plasma of temperature  $T_{\text{sep}}$ , the maximum rotational velocity  $\omega_r r_p$  equals the antiproton thermal velocity  $v_{\text{th}} = \sqrt{2kT/m_p}$ , and the antiproton density will be a factor of  $e$  higher at  $\rho = r_p$  than in the center  $\rho = 0$ . Correspondingly, we define the characteristic radial length scale

$$d_{\text{sep}} \equiv r_p \frac{\sqrt{2kT/m_p}}{\omega_r r_p} \approx \left( \frac{8kT\epsilon_0^2 B^2}{m_p n^2 q^2} \right) \quad (8.4)$$

which describes the distance over which the density diminishes, i.e.  $n_p(\rho, z) \propto \exp(\rho^2/d_{\text{sep}}^2)$ . Note that  $d_{\text{sep}} = r_p$  for  $T = T_{\text{sep}}$ .

As demonstrated below, electron-antiproton plasmas realized in current antihydrogen experiments cool into the well-separated regime. Previous experiments that first

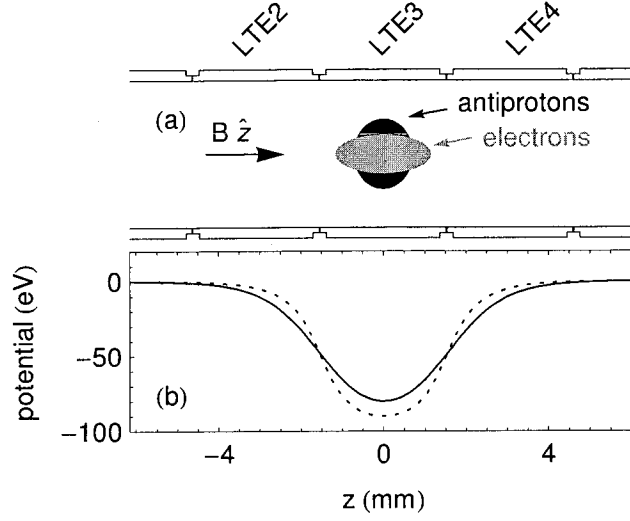


Figure 8.1: (a) Schematic of electron-antiproton plasma showing centrifugal separation within a cross-section of the trap electrodes. (b) 100 V applied to electrode LTE3 produces wells that are nearly harmonic well on axis (solid) and deepen off axis ( $\rho = 12$  mm shown dotted). Adapted from Ref. [125].

demonstrated the electron-cooling of antiprotons, on the other hand, used smaller, less dense electron plasmas in a higher magnetic field [126, 35]. In these experiments, with typical parameters  $n_e = 10^7 \text{ cm}^{-3}$ ,  $r_p = 1 \text{ cm}$ ,  $B = 6 \text{ T}$ , the temperature of 4.2 K was higher than  $T_{\text{sep}} \approx 1 \text{ K}$ .

## 8.2 Measurement by Axial Ejection

In this first demonstration of centrifugal separation, the radial-dependence of the Penning trap axial confinement is used to investigate the radial distribution of antiprotons from their axial escape. We begin by loading a plasma of  $N_e = (100 \pm 5) \times 10^6$  electrons with  $r_p = 5.0 \pm 0.2 \text{ mm}$  in  $B = 3.7 \text{ T}$  (methods in Section 4.3). Approximately  $N_p = 10^6$  antiprotons are then loaded from typically nine injection bunches from CERN's Antiproton Decelerator (methods in Section 2.2.2), and the two-component



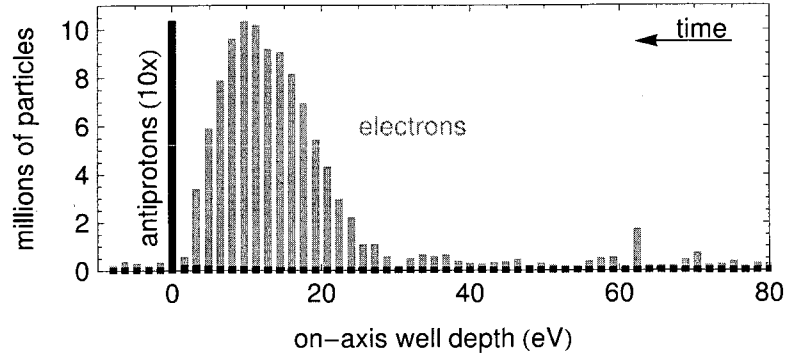


Figure 8.2: Number of antiprotons and electrons ejected from the trap as the applied potential is reduced by sequential, nonadiabatic 2-V steps. Adapted from Ref. [125].

plasma subsequently cools via electron synchrotron radiation to a temperature well below  $T_{\text{sep}} \approx 74$  K (see Section 6.1).

Figure 8.1a represents the resulting electron-antiproton plasma located within a cross-section of the trap electrodes. Axial confinement is created by applying 100 V to electrode LTE3 relative to the other electrodes. As shown in Fig. 8.1b, the resulting trap confinement is shallowest along the trap axis, 80 eV, and increases with radius. Near the electrode surface the potential approximates a rectangular function with an amplitude of 100 eV. As discussed in Section 5.1, the plasma space-charge potential increases the radial-gradient of the axial confinement, since the axial repulsion is greatest along the trap axis and diminishes at larger radii.

Centrifugal separation of antiprotons is observed when the axial confinement is reduced and particles at small radii preferentially leave the trap. As a first measurement (shown in Fig. 8.2), the axial confinement is reduced in a series of 2-V steps, as in typical charge counting (method in Section 2.3.2). After each step, ejected particles accelerate towards the degrader foil. Antiprotons are counted by

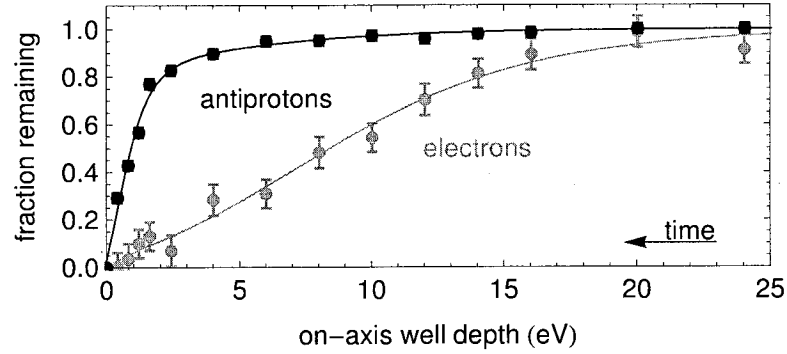


Figure 8.3: Fraction of antiprotons and electrons remaining after the well depth is decreased to the indicated value, with smooth curves to guide the eye. From Ref. [125].

detecting their annihilation products and electrons are counted by integrating the charge deposited on the foil. The difficulty of interpreting the charge deposited by antiprotons is avoided since there are relatively few particles and they are essentially all ejected in one pulse. Figure 8.2 shows the numbers of electrons and antiprotons ejected in each step. The antiprotons, residing in a relatively deep electrostatic well due to their location at a large radius, are nearly all ejected in the last step in which the well is finally inverted. As expected, the measured electron distribution appears unchanged by the addition of the antiprotons (a comparable electron distribution is shown in Fig. 2.11).

In a related experiment, the confining potential is instead decreased at a constant rate over 10 s from 80 eV on-axis to a chosen value, so that a fraction of the particles are lost. The potential is then returned to the initial depth and the remaining particles are counted from a series of ejection pulses identical to those used in Fig. 8.2. As seen in Fig. 8.3, a majority of the electrons are spilled out of the trap before any significant antiproton loss is detected. Once the on-axis trap depth is reduced to 2 eV, only 10%

of the initial electrons remain while 80% of the initial antiprotons are kept. This essential result does not change when the time over which the confining potential is reduced is varied between 0.1 and 10 s, although complete loss curves as in Fig. 8.3 for varying times have not been compared due to limited antiproton availability. This independence from ramp time is consistent with a more recent study that reports radial transport times of less than 100 ms for similar two-component plasmas [127].

### 8.3 Measurement by Magnetic Expansion

A second probe of the radial distribution of the antiprotons is achieved by reducing the magnetic field so that the plasma expands and strikes the trap electrode surface. From Eq. 4.1, the canonical angular momentum  $P_\theta$  of a trapped plasma is to a good approximation proportional to a product of the mean square radius  $\langle r^2 \rangle$  and magnetic field,  $P_\theta \propto B \langle r^2 \rangle$ . Accordingly, as  $B$  is reduced the plasma expands radially, as demonstrated in Section 4.2.2.

These measurements begin with a plasma with  $N_e = (100 \pm 10) \times 10^6$  and  $N_p = (1.0 \pm 0.1) \times 10^6$  in  $B = 3.7$  T with a varied radius  $r_p = 4.8$  to 7.8 mm. Antiproton annihilations are then recorded as the magnetic field is reduced to 1.0 T at a constant rate of  $7 \times 10^{-3}$  T/s. Once the magnetic field has reached 1 T, the remaining particles are counted by the methods used in the previous section. The detection sensitivity for antiproton loss is limited by the cosmic-ray background to approximately  $10^4$  antiprotons, and that for electron loss is limited by the loading reproducibility of  $5 \times 10^6$  electrons. For trials with an initial plasma radius  $r_p < 6$  mm, no particle loss is detected. Centrifugal separation is apparent for trials with an initial  $r_p > 6$  mm

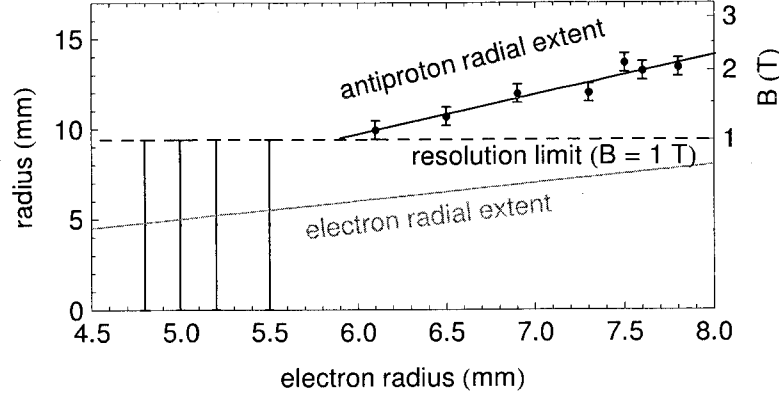


Figure 8.4: Initial antiproton radial extent as a function of the initial electron radius, deduced from the magnetic field at which antiprotons losses are first observed when  $B$  is reduced from 1 to 3.7 T. An assumption that the relative plasma geometry is constant is made, as discussed in the text. No antiproton loss is observed for the four leftmost measurements. The electron radius (gray) is included for comparison. From Ref. [125].

where, in contrast, a majority of the antiprotons are lost while still fewer than  $5 \times 10^6$  electrons are lost. The antiprotons all reside at larger radii than nearly all electrons.

The magnetic field at which antiproton loss is first observed is dictated by the initial distribution, since  $B \propto 1/\langle r^2 \rangle$ . If we assume that the relative plasma geometry does not change during expansion, e.g. the plasma remains a spheroid, the antiproton radial extent  $r_{\max} \propto 1/\sqrt{B}$ . With this assumption, Figure 8.4 shows the initial antiproton radial extent as a function of the initial electron radius  $r_p$ . The magnetic field at which the first antiproton loss is observed is shown on the right axis. The magnetic field could not practically be reduced below 1 T, so a resolution limit is reached corresponding to an initial radial extent of 9 mm.

Figure 8.4 shows that the inferred initial antiproton radial extent is 3 to 5 mm larger than the initial electron radius. This may indicate that a few antiprotons are poorly coupled to the electrons, and thus the antiprotons are in a non-equilibrium

distribution. This is not the case for most antiprotons, however, since the radii of antiproton plasmas determined by axial ejection (Section 5.1) are consistent with the initial electron plasma radii. Alternately, the discrepancy may be due to the assumption that the relative plasma geometry is constant, which is likely poor once the plasma expands beyond the quadratic potential of the central trap region. The geometry of large plasmas that extend to non-quadratic trap potentials have been previously studied in our trap [58, 52]. In particular, Ref. [52] shows that it is possible that  $r_{\max}$  grows faster than  $\langle r^2 \rangle$  as  $r_{\max}$  approaches the electrode radius. This effect could be studied by computing the equilibrium geometry of a series of single-component plasmas that simulate an expansion. A precise determination of the plasma distribution from this expansion technique, however, may be limited by uncertainty in the trap potential close to the electrodes due to, for example, patch effects on electrode surfaces. In addition, such a calculation of equilibrium geometries in non-ideal trap potentials would assume sufficient radial transport rates to maintain an equilibrium distribution throughout the expansion. As mentioned above, a very recent measurement suggest this is achieved [127]. In agreement, we find that the expansion loss results are unchanged when the expansion is slowed by a factor of two.

## 8.4 Discussion and Suggestions for Further Studies

The centrifugal separation of antiprotons and electrons is detected here for the first time by two different methods. This observation provides confirmation that the plasma temperature is below the calculated  $T_{\text{sep}}$  of 50 to 100 K for plasmas with radius of 8 to 4 mm, in agreement with the measurements in Chapter 6. Furthermore,

the separation is important to understanding the evolution of electron-antiprotons plasmas throughout antihydrogen experiments.

For example, in the standard method to remove the initial cooling electrons from antiprotons, the trap potential is pulsed off for a brief duration in which electrons escape but the more massive antiprotons do not. If the antiprotons are evenly distributed throughout an initial spheroidal plasma with radius  $r_p$ , the resulting antiproton plasma also has a radius  $r_p$ . On the other hand, if the antiprotons are initially located in a thin shell with radius  $r_p$ , the antiprotons will not be in an equilibrium distribution once the electrons escape. In this case, the antiprotons re-equilibrate through radius-changing collisions to a spheroid with increased radius  $\sqrt{5/2}r_p$ .

As discussed, the precise determination of the antiproton distribution by the axial ejection and magnetic expansion methods described is complicated by accurately calculating loss in non-ideal trap potentials. A promising route for future studies is to directly image the electron and antiproton distributions by ejecting them onto a phosphor imaging screen that has been installed on the translating window flange (see Fig. 2.2) but not yet used. A similar imaging system was used in very recent measurements of equilibration dynamics in electron-antiproton plasmas [127]. Alternately, the window-flange aperture may be used as a spatial filter in counting ejected plasmas. Measurement of the antiproton distribution width  $d_{\text{sep}}$  will provide an estimate of the plasma temperature, complimenting the temperature measurement methods developed in Section 5.1. Furthermore, measurements of equilibration rates will provide insight into the dynamics of electron-antiproton plasmas used in antihydrogen experiments.

## Chapter 9

# An Improved Penning-Ioffe Trap

Initial studies of charged-particle confinement [5] and antihydrogen production [6] in a Penning-Ioffe trap have been accomplished in our first apparatus to incorporate a magnetic trap for antihydrogen atoms (Chapter 3). The simple coil geometry and traditional construction of this first-generation magnetic trap enabled its timely and reliable fabrication. However, it was recognized early on that substantial gains could result from an improved magnet design [52]. In particular, we desire to improve the atom-detection sensitivity and trap depth which currently limit our trapped-antihydrogen experiments (Section 3.3). The potential benefits of higher-order transverse trapping fields are also compelling, yet less certain (Section 3.1).

This chapter describes the design and construction of a second-generation apparatus motivated by these issues. Central to this upgrade is a unique Ioffe trap with a number of advantages, including a rapid turn-off capability for single-atom detection, a greater trap depth, and the capability to produce both octupole and quadrupole radial trap geometries. The new second-generation Penning-Ioffe trap incorporat-

ing this magnet and the cryostat that supports it are currently being mounted by members of ATRAP at CERN.

The second-generation Ioffe trap is enabled by emerging direct-wind magnet fabrication methods [128, 129] not available to us earlier. By these techniques, transverse-field magnets are constructed by laying wire directly onto an insulating bore tube, while mechanical support is provided by subsequently added fiberglass overlayers. Sequential layers can be constructed by repeating the process, building to larger radii. For our application, this fabrication approach allows for large flexibility in coil design and minimizes the radial space required by the magnet assembly. In one example of direct-wind methods developed at Brookhaven National Lab, a winding layer is initially tacked with adhesive then secured with a tensioned overwrap [129, 130]. This method was recently used to construct an octupole-Ioffe trap used in the antihydrogen apparatus of the ALPHA collaboration [131].

For our trap, we chose wire-in-groove fabrication, an alternate approach developed by the Advanced Magnet Lab (AML) [128]. In this method, wire is laid into closely machined grooves in a G-10 tube, after which the structure is vacuum-impregnated with epoxy. Successive layers are constructed by adding additional G-10 which is then machined down to a minimal support structure. The result is a single, robust composite of G-10, conductor, and epoxy. This method has previously shown excellent performance with planar quadrupole coils, which were shown to operate with nearly ideal superconductor performance after minimal quench training [132, 133].

A conceptual design based on this fabrication method was formulated, and in early 2007 an agreement was made for AML to undertake construction of our



magnet system. The final magnet design resulted from a close collaboration with AML, including prototyping to test the technical limits of fabrication methods. Per our contract, AML agreed to provide a complete and tested magnet system but backed out of this contract when difficulties arose with the planned construction of a liquid helium enclosure. With few options to move forwards, a new contract was made in the summer of 2008 under which AML would only fabricate the magnet coils and forgo other aspects of the project, leaving it to us at Harvard to solve the technical problems that they could not. These magnet windings were delivered to Harvard in 2010, and they have now been integrated into a suitable liquid helium enclosure. Below we describe the design, construction, and expected performance for this new Ioffe trap.

## 9.1 Design Objectives

A principle design requirement of a new Ioffe trap is compatibility with our experimental platform (Section 2.1). A schematic of the Ioffe trap located within the ATRAP apparatus is shown in Fig. 9.1. The radial dimensions of the Ioffe trap are established by the inner radius of the cryogenic insert located just inside of the inner fiber detectors shown. Additionally, the axial dimension is set by our current Ioffe trap to allow for the interchangeability of parts, including the XY-stage and antiproton catching trap. A further requirement is that the magnet includes four radial ports that provide access to the central trap region. This access is currently needed for the creation of a Rydberg atom beam for charge-exchange experiments and is foreseen to be critical for future access of ultraviolet laser light.

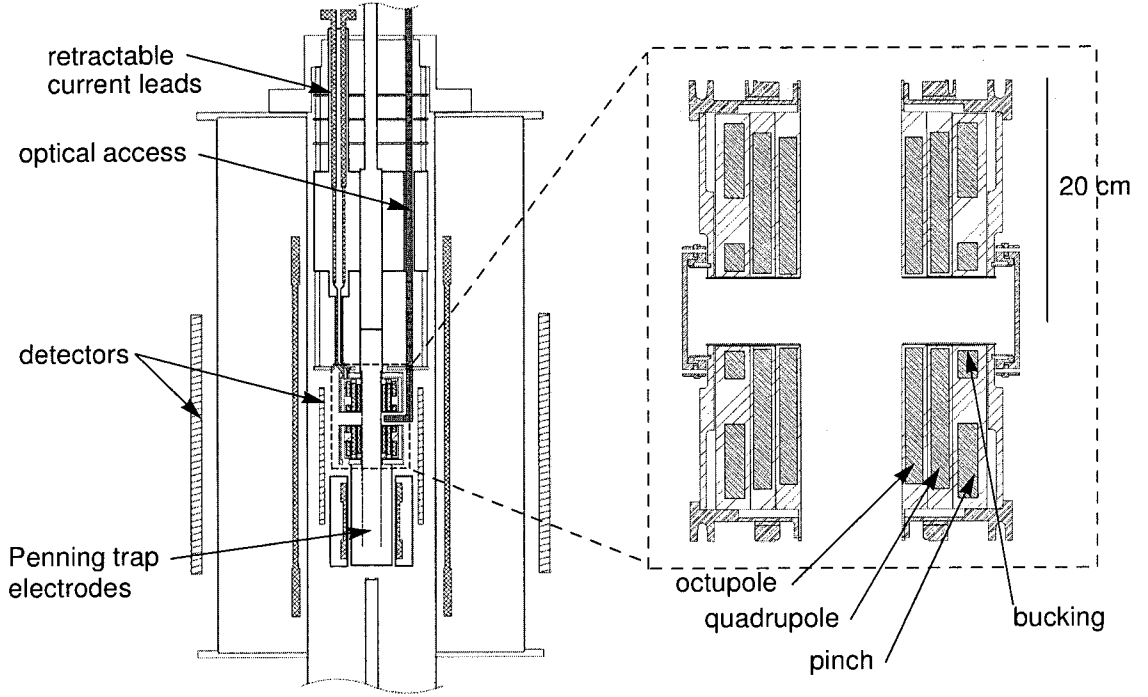


Figure 9.1: Schematic of the Ioffe trap mounted within the Penning-Ioffe apparatus (left) with a closer view of the cross-section of the Ioffe trap, showing the four coils embedded in the winding structure (right).

A second design objective for the Ioffe magnet is a turn-off time sufficiently brief to enable the detection of a single trapped antihydrogen atom (as discussed in Section 3.3). Our current detector system has a background rate of 0.5 Hz due to cosmic rays while detecting antiproton annihilations with an efficiency of 25%. For this performance, a 20-ms trap ejection is required to have less than a 1% probability of a background event during the ejection. (As discussed in Section 2.3.3, this may be adjusted with a trade-off made between antiproton detection efficiency and background rate.) The turn-off time  $\tau$  of a magnet that generates a specified trap field is proportional to the inverse of its operating current  $I$  and the turn-off voltage  $V$ , i.e.  $\tau \propto (VI)^{-1}$ . We thus desire to use the maximum operating currents that are feasible

for our cryostat and achieve a large turn-off voltage, which is ultimately limited by electrical breakdown.

A final design objective concerns the magnetic fields generated. As discussed in Chapter 3, charged-particle confinement in a Penning-Ioffe trap is expected to be improved within an octupole-Ioffe field as compared to a quadrupole-Ioffe field. Since the magnitude of a multipole field is proportionate to  $\rho^{n-1}$  (Eq. 2.1), for equal trap depths an octupole field ( $n = 4$ ) is substantially smaller than a quadrupole field ( $n = 2$ ) near the trap axis. On the other hand, the larger trap gradient of the quadrupole trap improves the compression of trapped atoms resulting in, for example, greatly improved laser cooling rates. Early in the design process, it became apparent that a substantial quadrupole coil could be nested outside of the octupole coil with little detriment to the octupole design. Such nested coils give us the capability to directly compare the two field geometries in antihydrogen experiments, and it may even provide the possibility of transferring atoms initially captured in an octupole trap to a quadrupole trap for laser cooling and spectroscopy.

Within the conceptual arrangement of nested octupole and quadrupole coils, we seek to optimize the trap depths created with each of these two field geometries. As with lowering the kinetic energy of the antihydrogen synthesized (discussed in Chapter 6), increasing the trap depth will enable more atoms to be captured. For atoms with an average thermal energy much greater than the trap depth  $U_{\text{trap}}$ , the number of trapped atoms is proportional to  $(U_{\text{trap}})^{3/2}$ . A critical feature of the second-generation apparatus that enables us to achieve significant trap depths with the nested-coil geometry are novel ultrathin Penning-trap electrodes (Section 9.5), which minimize the

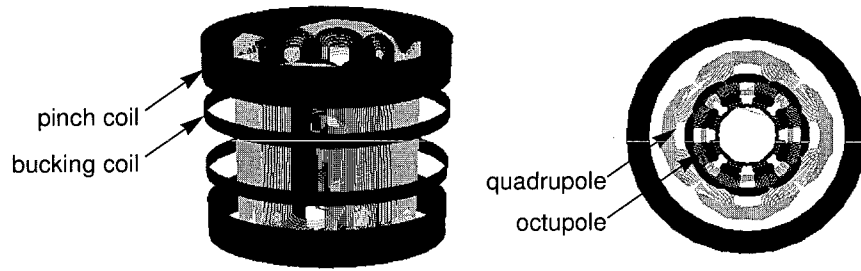


Figure 9.2: Nested coils that comprise the new Ioffe trap. For clarity, only a single layer of each coil is shown.

distance between the coil windings and the trap region.

Before moving on to the design details of our new magnet, we should note the performance of the first-generation magnet with regards to these design objectives. Our current magnet produces a quadrupole trap depth of 380 mK. To detect trapped antihydrogen atoms, the trap depth is reduced by 80% in approximately 1 s with an induced quench of a racetrack coil (Section 3.3). Undesirably, the quench dissipates energy in the magnet coils and appears to cause unreliable magnet performance. As we will see below, the second-generation magnet will produce a quadrupole trap as deep as 790 mK as well as an octupole trap depth of 510 mK. For atom detection, the magnet is minimally disturbed as the coil energy is dissipated in a resistor outside of the cryostat. For the octupole trap, we anticipate a reduction in trap depth by 80% in just over 10 ms.

## 9.2 Winding Design

An overview of the magnet windings is shown in Fig. 9.2. The octupole coil is located as close to the inner bore as possible to maximize its usable field. Outside

	Second generation		First generation
	octupole trap	quadrupole trap	quadrupole trap
octupole coil	680 A	0	-
quadrupole coil	0	500 A	69 A
pinch coil	330 A	390 A	80 A
bucking coil	250 A	340 A	-
trap depth	0.78 T (510 mK)	1.20 T (790 mK )	0.57 T (380 mK)

Table 9.1: Operating currents and trap depths of the new second-generation magnet compared to those of our first-generation magnet. The trap depths are specified as a field magnitude as well as an energy (in temperature units) for ground-state antihydrogen atoms.

of this, a quadrupole coil is positioned with a matching azimuthal orientation to accommodate four radial ports through the nested windings. Lastly, four solenoidal coils are located at the largest radius. The outer two solenoid pinch coils operate with the same sense of current to provide axial confinement, as in those of the current apparatus (Fig. 2.6). Undesirably, these pinch coils generate an appreciable axial field in the center of the trap due to their large radius and relatively small axial separation. The vector addition of this axial field and the multipole field reduces the radial trap depth. To remove this unwanted axial field near the trap center, the two additional bucking coils are added, which operate with an opposite sense current.

The trap depth achieved by these coils is limited by the performance of the multipole windings. For these coils, a large diameter, high superconductor content, multifilament NbTi wire was chosen to maximize the fields generated while operating at a high current. A wire with a copper-to-superconductor ratio of 1:1 is used, which is the minimum copper content that would still provide necessary thermal and current-sharing properties,. A wire diameter of 0.85 mm, the largest readily available,

results in a coil with relatively few turns that operates at a high current, as required for a rapid turn-off time (Section 9.4, below). While multi-wire cable can provide even higher operating currents, it was avoided due to potentially worse mechanical stability. For the wire chosen, we use the minimum wire spacing that could be achieved with the AML wire-in-groove fabrication technique.

To determine the optimal wire configuration, the trap depth is calculated for various coil parameters (number of turns and layers, azimuthal distribution, bore diameter, and spacing at the coil ends). The trap depth is determined by calculating the maximum possible operating current supported by the superconductor given the peak magnetic field on the conductor. This calculation is done iteratively, since the primary contribution to the peak field is the coil's own field, although the field contributions from the pinch coils, bucking coils, and primary Penning-trap solenoid (providing 1 T) are also accounted for. The operating currents and corresponding trap depths for the optimized geometry is shown in Table 9.1. These trap depth calculations account for the thickness required for Penning-trap electrodes. In the constructed apparatus, ultrathin electrodes with an inner radius of 36.0 mm (Section 9.5) fit within the magnet bore with a radius of 49.7 mm. It should be noted that these specifications assume ideal superconducting performance (short sample current), and actual superconducting magnets often perform somewhat worse than this due to, for example, mechanical defects [134]. It is encouraging, however, that previous multipole coils constructed by this wire-in-groove technique have operated at over 90% of the ideal performance [132, 133].

A detailed view of the multipole coil windings is presented in Fig. 9.3. A cross-

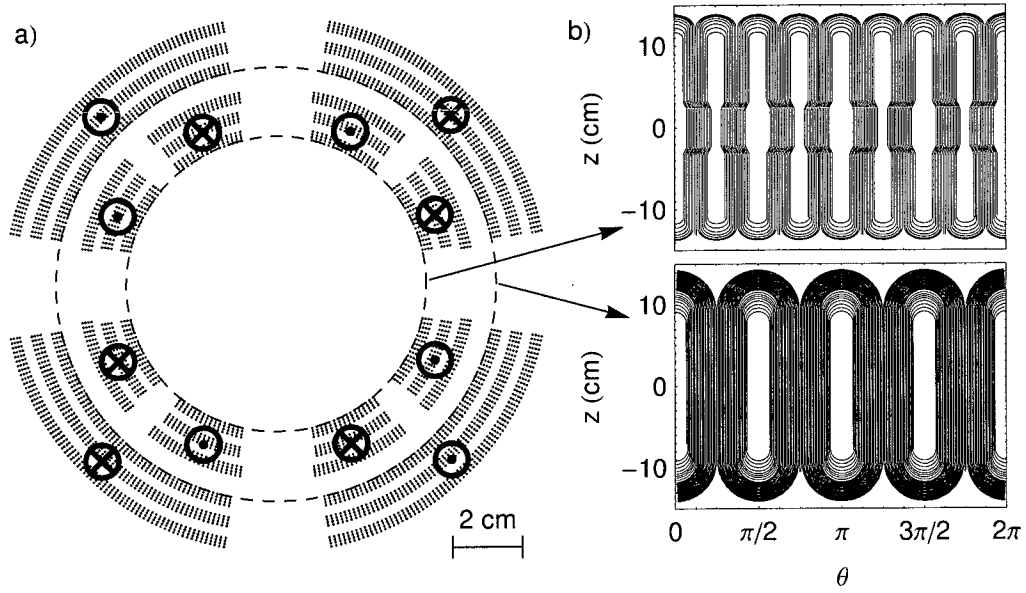


Figure 9.3: Windings of the octupole and quadrupole coils shown in (a) a cross-section at the axial center with current direction for each wire group labeled and (b) rolled-out views for the innermost coil layers.

section of the wires at the axial center of the windings displays the alternating axial currents in the magnet poles. The innermost layers of the octupole and quadrupole coils are shown in a rolled-out view in Fig. 9.3b. To accommodate radial access to the trap center, the octupole wire azimuthal position is altered near the trap center. The high-order transverse-field harmonics generated by this distortion do not significantly penetrate into the trap region, although a slight axial asymmetry is caused by azimuthal currents. Empirically it is found that roughly 100 mK of trap depth is gained with this distortion, in comparison with a straight-wire design of fewer turns that accommodates access ports of the same size.

The pinch and bucking coil cross-sections are shown in Fig. 9.1. These coils are wound with rectangular wire with a cross-sectional area of  $1.48 \text{ mm}^2$  and a copper-

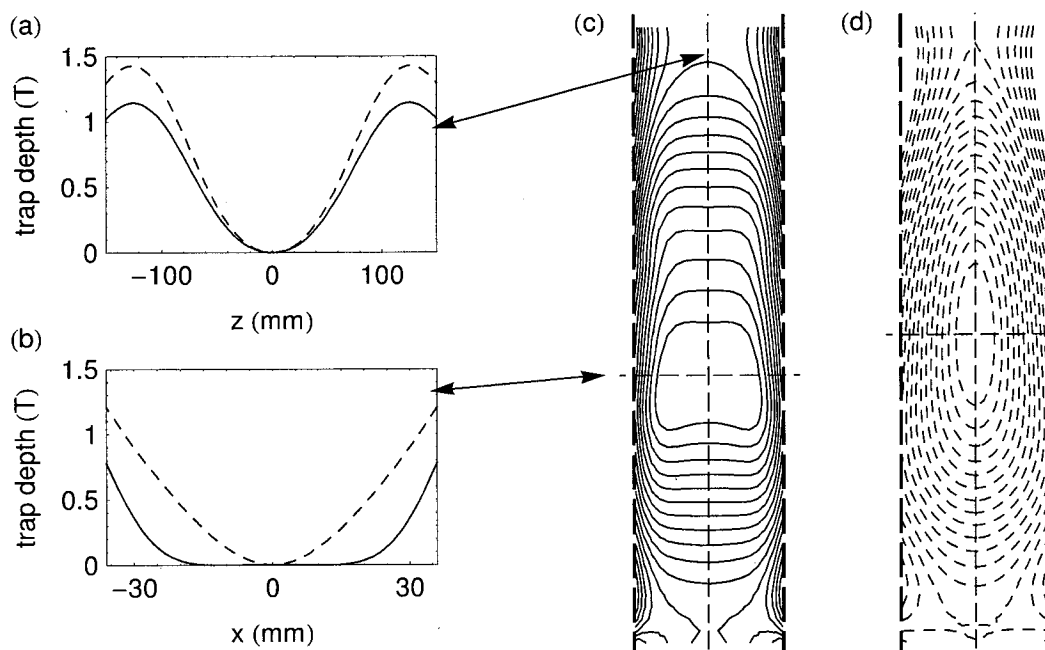


Figure 9.4: Trap depths generated by the octupole (solid) and quadrupole (dashed) traps. The trap depth is shown (a) along the trap axis, (b) along the radius at the trap center, and (c,d) in equipotentials spaced by 0.1 T.

to-superconductor ratio of 2.7. In contrast to the multipole coils, the performance of which will determine the trap depth, these solenoidal coils will be operated at less than 30% of the maximum current determined by the peak field on the conductor. The two pinch coils and two bucking coils are operated independently so that the relative currents in each pair can be optimized for the as-built geometry.

The magnetic fields generated by the octupole and quadrupole traps are compared in Fig. 9.4. As discussed, the octupole trap center is axially shifted from the quadrupole trap center by 1.7 cm due to the side-port adjustment.



### 9.3 Liquid Helium Enclosure

To achieve the calculated operating currents, the coils must be submerged in liquid helium. This reservoir allows for rapid dissipation of any heat generated within the coils. In this section, we describe the enclosure that we constructed to surround the coils and separate the cryogen volume, outer insulating vacuum, and inner trap vacuum.

A central challenge in constructing this enclosure is to minimize the distance between the trap boundary (the inner surface of the Penning-trap electrodes) and the octupole coil windings, which generate a field that diminishes rapidly over this distance. If, for example, the enclosure occupied a radial thickness of 3 mm, the trap depth would be reduced by more than 30%. In addition, the joining techniques used to construct the enclosure are restricted by the requirement that the coil structure not be damaged during its fabrication. Given the proximity of the windings to the side ports, in particular, we decided that the feasibility of welding side tubes to a bore tube was not certain and would require a substantial effort to study. Instead, the joining method chosen was epoxy overlap joints, which do not require an increased temperature and enable the coil bore to serve as the bore of the enclosure. As discussed above, these epoxy joints are what AML was not able to successfully fabricate.

The enclosure was assembled with twenty sequential epoxy joints made between the twelve parts shown in Fig. 9.5a. First, the two aluminum end plates are fastened to the G-10 outer tube and winding structure. Each end plate contains five explosively bonded titanium flanges which allow for seals to the cryogen and trap-vacuum spaces.

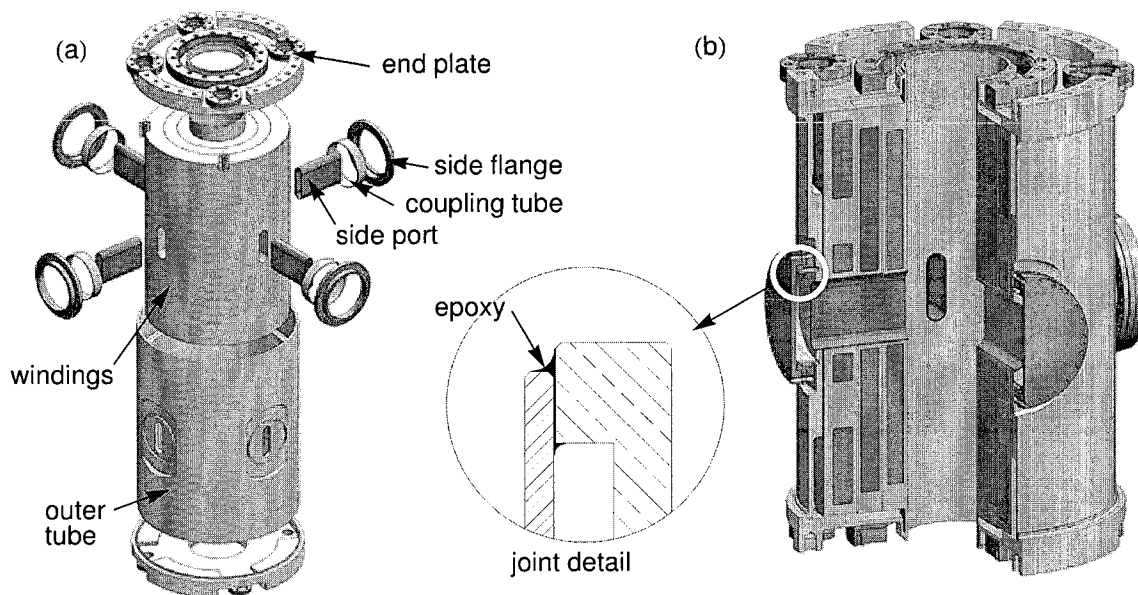


Figure 9.5: (a) Exploded view of the liquid helium enclosure. (b) Cut-away view with a detailed view of an epoxy joint.

Next, four side ports are joined to the inner bore of the windings and the outer tube. At this point, the cryogen space is sealed. Lastly, to separate the inner trap vacuum and outer insulating vacuum, four copper indium-seal flanges are attached to the outer tube with a short G-10 coupling tubes.

A typical epoxy joint is detailed in Fig. 9.5b. On all joints, a low-viscosity cryogenic epoxy (Stycast 1266) was applied to the top of a  $0.0030 \pm 0.0005$  inch gap. Over a period of approximately 10 minutes, the epoxy wicks onto the clean, lightly sanded surfaces to fill the gap (with a minimum length of 0.10 inch) and create smooth fillets at the joint corners, as shown. This technique has previously been used to create vacuum cells in cryogenic apparatus by joining G-10 to both metal and glass [135]. We constructed many test joints between G-10, Al, and Cu, and found that the method was reliable and the joints survived dozens of thermal cycles between 300

and 77 K.

During the process of designing the enclosure, three full-sized mock-ups were created to test joint geometries and assembly jigs. The first test prompted a redesign of the end-plate joints to minimize the overlap of excess epoxy with the top aluminum surface. It was found that the epoxy cracks in this region after thermal cycling, and a leak appeared after 15 thermal cycles. A second mock-up tested a revised geometry that limits the surface exposed to excess epoxy and survived 40 thermal cycles. In testing the final enclosure, it was found that the substantial thermal mass of the coils, which was not present in the mock-ups, resulted in catastrophic temperature gradients during thermal cycling. Small leaks in each joint between the side-port tubes and winding structure were repaired by applying a few drops of epoxy to the joint while the cryogen space was under vacuum. The enclosure then survived three gradual thermal cycles in which the cooling occurred over 12 hours and the end-plate temperatures we observed not to differ by more than 30 K. Thermal cycling of the magnet system when it is incorporated in the full apparatus will be more gradual. By current methods, this process takes over 30 hours.

## 9.4 Rapid Turn Off and Quench Protection

To count antihydrogen atoms captured in the trap, a magnet coil is rapidly de-energized (Section 3.3) and coinciding antiproton annihilations are detected. For our new magnet system, this will be accomplished with the high-current magnet circuitry shown in Fig. 9.6 for each of the four coil sets (octupole, quadrupole, pinch, and bucking) that are run independently. In normal operation, the current from a power

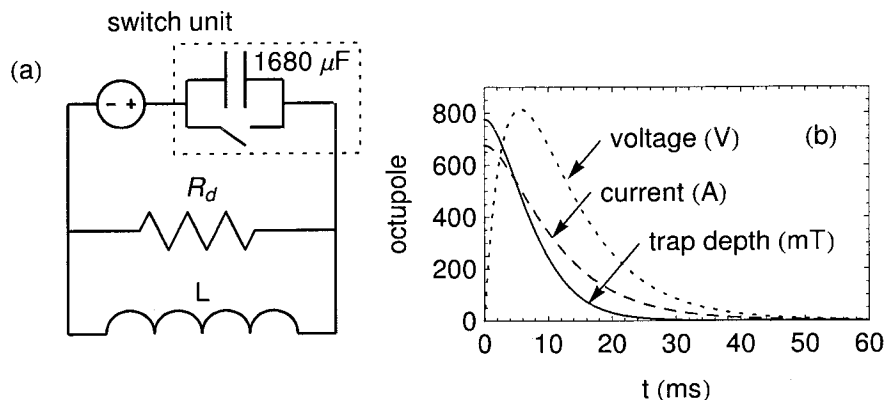


Figure 9.6: (a) Schematic of high-current magnet circuit. (b) The calculated turn off of the octupole coil.

supply (one or two Agilent 6681A units) passes through a closed switch (Semikron SkiiP 1513GB172, IGBT-based integrated power device) and continues through the magnet coil. To de-energize a coil, its switch is opened and the current is diverted through a dump resistance  $R_d$  located outside of the cryostat. The calculated resulting decay of the current in the octupole circuit, for example, is shown in Fig. 9.6b.

To minimize the turn-off time, the dump resistance and capacitance should be chosen so that the maximum acceptable voltage is achieved and the circuit is critically damped. We estimate a maximum voltage of 800 V to use for calculations here. The switch and magnet coils are rated for more than 1 kV, but a potential limit comes from the current and voltage-sense wires in the cryostat. These leads exit the cryostat in helium, a gas with particularly low breakdown voltage, so a lower voltage limit may be determined as this installation is tested. We choose a parallel capacitance of  $1680 \mu\text{F}$  to be pre-installed in the switches, and while this may be altered, it puts us in an acceptable operating range. The resistors  $R_d$  are then chosen so that the circuits are slightly overdamped (to prevent oscillations) and the voltage does not exceed the

	Inductance $L$	Dump resistor $R_d$	Turn off ( $1/e$ )
octupole coil	19.9 mH	1.6 $\Omega$	8.5 ms
quadrupole coil	113.1 mH	1.8 $\Omega$	60 ms
pinch coil	107.4 mH	3.5 $\Omega$	23 ms
bucking coil	19.5 mH	1.5 $\Omega$	9.6 ms

Table 9.2: Circuit parameters for each coil and the resulting turn-off time.

determined limit. The achieved turn-off time for each coil, defined as the time over which the current reduces by a factor of  $\exp(1)$ , and the chosen  $R_d$  are shown in Table 9.2.

The octupole turn-off time of 8.5 ms results in a 90% trap reduction in 15 ms. For the detection of antihydrogen atoms during this window, a single count is a signal of at least one trapped atom with 99% confidence for the detector scheme employed in Section 3.3. If the detection efficiency is increased to over 50% (see Fig. 2.3.3), a single count still corresponds to nearly 80% confidence. This calculation suggests the feasibility of single-trial, single-atom detection with the new Ioffe trap.

To achieve these turn-off times, quench protection diodes could not be incorporated in the magnet windings. As a result, an active quench-protection system is used [134]. A quench is detected by monitoring voltages across coil segments. A comparison between different segments differentiates a resistive voltage, indicative of a quench, from expected inductive voltages caused by changes in current. If a quench is detected, the turn-off switch is triggered and the coil energy is rapidly dissipated.

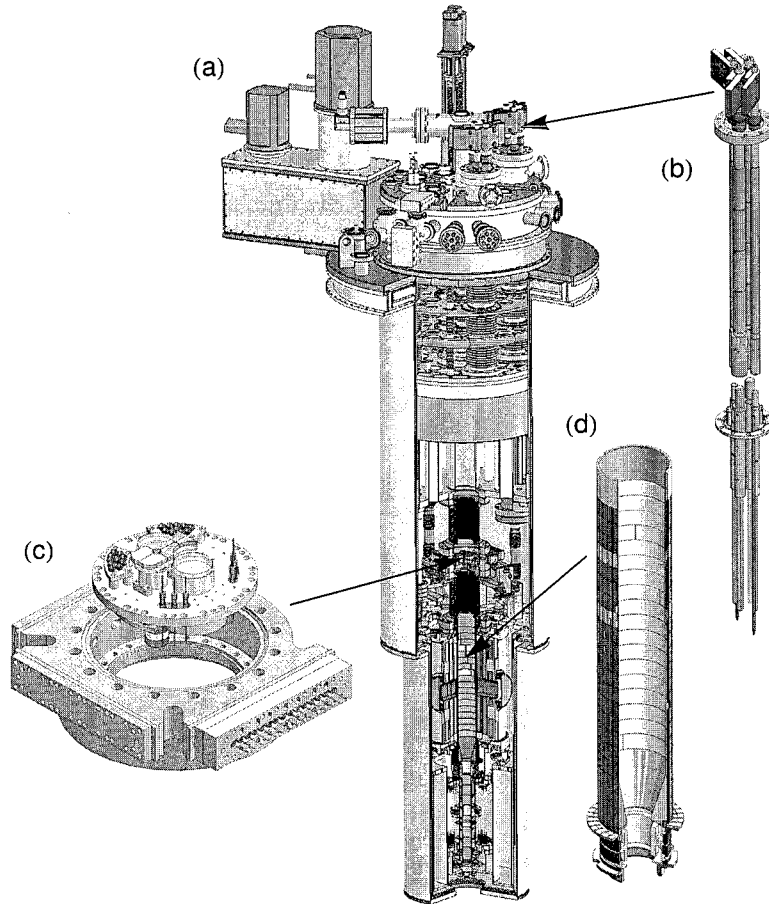


Figure 9.7: (a) The new Penning-Ioffe trap and cryostat, with enlarged views of a (b) custom high-current lead cluster, (c) compact window flange, and (d) stack of ultrathin Penning-trap electrodes.

## 9.5 Penning Trap and Cryostat

While the new Ioffe trap is broadly compatible with the current apparatus, a new cryostat (shown in Fig. 9.7) was needed to accommodate large currents to operate the magnets. Two custom current-lead clusters are each constructed from two 750 A and two 350 A detachable vapor-cooled current leads and superconducting bus bars (American Magnetics Inc.). The hat, baffles, and liquid helium container were

modified from those shown in Fig. 2.2 to accommodate these large assemblies.

Other important revisions to the apparatus include ultrathin, large-diameter Penning-trap electrodes, shown in Fig. 9.7d. These electrodes maximize the trap depth by minimizing the distance between the multipole coils and the electrode inner surface (the trap boundary). A detailed description of the novel electrode construction is anticipated in a future thesis [50]. Additionally, a compact window flange has been designed to minimize the necessary X-Y stage travel. While not directly related to the new Ioffe trap, this important improvement will enable use of the stage while minimizing the risk of catastrophic failure of its edge-welded bellows [48]. This new design has recently been installed in the previous apparatus as well. Lastly, it should be mentioned that an additional cryocooler-cooled insert dewar has been acquired for operation of this cryostat. This insert matches the dimensions of our previous apparatus, and has demonstrated slightly improved performance due to increased insulation between the dewar layers. This second insert is foreseen to enable the interchange of two cold apparatus, eliminating the loss of experiment time due to thermal cycling.

The entire apparatus shown in Fig. 9.7, as well as the high-current and control circuitry for the new magnet, has recently arrived at CERN, and mounting of the magnet is currently underway by members of ATRAP. The first experiments with this new apparatus, including quench training of the magnet system, should take place soon.

# Chapter 10

## Conclusion

The feasibility of producing antihydrogen within a combined Penning-Ioffe trap, envisioned long ago [4], has now been demonstrated [6]. Despite well-founded concerns about the stability of charged particles in this trap geometry [61, 62], we measured typical confinement times on the order of 100 s, sufficient for atom production [5]. A proof-of-principle demonstration follows in which antihydrogen that was formed in a Ioffe trap with a trap depth of 380 mK for ground-state atoms was detected by a counting antiprotons stripped by a Stark-ionization.[6]. A first search for trapped antihydrogen determines a limit of fewer than 20 atoms trapped per trial while more recent experiments lower this bound to 12. Within the last year, similar experiments with an apparatus optimized for detection sensitivity found at first 0.1 atoms [68] (and later, up to 1 atom [45]) trapped per trial.

The principle motivation of this thesis is to greatly increase the number of antihydrogen atoms that may be captured in a magnetic trap for spectroscopy. Progress has been made on two fronts. First, we implement experimental methods to measure and



control the properties of trapped antiproton and positron plasmas used for the synthesis of antihydrogen. Second, we design and construct a second-generation Penning-Ioffe apparatus which promises greatly improved performance and some unique capabilities for antihydrogen experiments.

To characterize and control our antimatter plasmas, we first implement a method to determine the geometry and density of a trapped plasma by measuring its oscillation frequencies. This diagnostic enables the study of rotating electric fields that compress electron and positron plasmas to radii as small as 2 mm. Reproducible plasma geometries that are independent of particle loading methods are now the standard in our apparatus.

The temperature of trapped plasmas, the second critical parameter for antihydrogen experiments, is investigated by two methods. First, the temperature of antiprotons is measured by counting particles that escape past a diminishing potential barrier. An analysis which accounts for the evolving space-charge potential of the plasma extends this standard technique to our few-Kelvin antiproton plasmas. A second temperature diagnostic, which does not rely on the sensitive detection of a small number of ejected particles, comes from the temperature dependence of plasma oscillation frequencies. In relative temperature measurements, electron plasma temperatures are studied with a resolution on the order of 100 mK as the trap-electrode temperature is modulated.

The trapped plasma diagnostics are applied in studies that allow for the preparation of greatly improved plasmas for trapped-antihydrogen experiments. A two-step process for cooling antiprotons was demonstrated [103]. First, a small number of

embedded electrons within an antiproton plasma effectively remove heat prior to antihydrogen synthesis. Additional adiabatic cooling is achieved by letting the plasma expand. These two methods together produce plasmas of up to 3 million antiprotons at a temperature of 3.5 K,  $10^3$  more particles at 3-times lower temperature than has previously been measured for cryogenic antiprotons. These cooling methods increase the fraction of antiprotons with energy lower than our Ioffe trap depth by a factor of 25, a promising improvement for increasing the trapping efficiency of antihydrogen, and further improvements seem attainable.

Substantial increases in the number of antiprotons and positrons available to produce antihydrogen are reported. An increased magnetic field, generated by a new antiproton-loading solenoid, and compression by the rotating-wall technique greatly improves the antiproton loading efficiency. This approach is used to accumulate over 10 million antiprotons into our Penning trap for antihydrogen experiments, a 14-fold improvement over previous methods. The rotating-wall technique also counteracts gradual expansion of large plasmas realized during positron accumulation. A constant positron loading rate achieves up to 4 billion positrons, a 20-fold improvement for our apparatus. These large particle numbers provide a promising start towards scaling-up the production of trappable antihydrogen. The efficiency of  $6 \times 10^{-5}$  trapped atoms per initial antiproton recently reported in Ref. [45], for example, corresponds to 700 trapped atoms if it can be equaled with our large antiprotons plasmas. A recent thesis [48] incorporated these particle-loading improvements in the charge-exchange production of antihydrogen and demonstrated a factor of 200 increase in antihydrogen yield from a proof-of-principle demonstration with many fewer particles [93].

Centrifugal separation is observed for electron-antiproton plasmas [125], a first for these two-component plasmas used in all cold antiproton and antihydrogen experiments. Implications for the geometry of antiprotons prepared for experiments is discussed. The separated geometry provides for a gradual procedure to remove electrons and a potential new method for determining the plasma temperature from the antiproton radial distribution.

The second focus of this thesis, undertaken concurrently with the experimental advances, is the design and construction of a second-generation Penning-Ioffe trap for trapped-antihydrogen experiments. The central improvement of this apparatus is a unique Ioffe trap which provides a number of advantages over the first-generation trap used for the experiments in this thesis. Recent developments in magnet fabrication methods enable a nested octupole-quadrupole coil design that allows the use and comparison of these two trapping-field geometries. A second key feature is a turn-off time sufficient for single-trial, single-atom detection with our current annihilation detector system. The magnet operates with currents roughly 10-times larger than those in the first-generation magnet, and an active quench protection system allows for large voltages to de-energize the coils. A considerable challenge arose when the manufacturer failed to produce a liquid helium enclosure for the new magnet system. Nevertheless, we were able to design and fabricate a proper enclosure at Harvard after thorough development and testing of epoxy joining techniques. Construction of the second-generation Penning-Ioffe trap, and the new cryostat with which it operates, is complete.

These advances are substantial progress toward our long-term goal of precise spec-

troscopy with antihydrogen confined in a magnetic trap. We now seek to apply these improvements to antihydrogen-trapping experiments. Studies undertaking scaled-up antihydrogen production in the first-generation Penning-Ioffe trap are underway, and meanwhile, the second-generation magnet has just been mounted on its cryostat at CERN. Much remains before precise tests with antihydrogen can be undertaken, but there are good reasons for optimism about the future of antihydrogen research.

# Bibliography

- [1] M. Amoretti, C. Amsler, G. Bonomi, A. Bouchta, P. Bowe, C. Carraro, C. L. Cesar, M. Charlton, M. J. T. Collier, M. Doser, V. Filippini, K. S. Fine, A. Fontana, M. C. Fujiwara, R. Funakoshi, P. Genova, J. S. Hangst, R. S. Hayano, M. H. Holzscheiter, L. V. Jorgensen, V. Lagomarsino, R. Landua, D. Lindelof, E. L. Rizzini, M. Macri, N. Madsen, G. Manuzio, M. Marchesotti, P. Montagna, H. Pruis, C. Regenfus, P. Riedler, J. Rochet, A. Rotondi, G. Rouleau, G. Testera, A. Variola, T. L. Watson, and D. P. van der Werf, *Nature* **419**, 456 (2002).
- [2] G. Gabrielse, N. S. Bowden, P. Oxley, A. Speck, C. H. Storry, J. N. Tan, M. Wessels, D. Grzonka, W. Oelert, G. Schepers, T. Sefzick, J. Walz, H. Pittner, T. W. Hänsch, and E. A. Hessels, *Phys. Rev. Lett.* **89**, 213401 (2002).
- [3] G. Gabrielse, N. S. Bowden, P. Oxley, A. Speck, C. H. Storry, J. N. Tan, M. Wessels, D. Grzonka, W. Oelert, G. Schepers, T. Sefzick, J. Walz, H. Pittner, T. W. Hänsch, and E. A. Hessels, *Phys. Rev. Lett.* **89**, 233401 (2002).
- [4] G. Gabrielse, in *Fundamental Symmetries*, edited by P. Bloch, P. Paulopoulos, and R. Klapisch (Plenum, New York, 1987), p. 59.
- [5] G. Gabrielse, P. Laroche, D. Le Sage, B. Levitt, W. S. Kolthammer, I. Kuljanishvili, R. McConnell, J. Wrubel, F. M. Esser, H. Glueckler, D. Grzonka, G. Hansen, S. Martin, W. Oelert, J. Schillings, M. Schmitt, T. Sefzick, H. Soltner, Z. Zhang, D. Comeau, M. C. George, E. A. Hessels, C. H. Storry, M. Weel, A. Speck, F. Nillius, J. Walz, and T. W. Haensch, *Phys. Rev. Lett.* **98**, 113002 (2007).
- [6] G. Gabrielse, P. Laroche, D. Le Sage, B. Levitt, W. S. Kolthammer, R. McConnell, P. Richerme, J. Wrubel, A. Speck, M. C. George, D. Grzonka, W. Oelert, T. Sefzick, Z. Zhang, A. Carew, D. Comeau, E. A. Hessels, C. H. Storry, M. Weel, and J. Walz, *Phys. Rev. Lett.* **100**, 113001 (2008).
- [7] G. Lüders, *Ann. Phys.* **2**, 1 (1957).
- [8] T. D. Lee and C. N. Yang, *Phys. Rev.* **104**, 254 (1956).

- [9] C. S. Wu, E. Ambler, R. W. Hayward, D. D. Hoppes, and R. P. Hudson, *Phys. Rev.* **105**, 1413 (1957).
- [10] L. D. Landau, *Nucl. Phys.* **3**, 127 (1957).
- [11] J. H. Christenson, J. W. Cronin, V. L. Fitch, and R. Turlay, *Phys. Rev. Lett.* **13**, 138 (1964).
- [12] T.W. Hänsch, J. Alnis, P. Fendel, M. Fischer, C. Gohle, M. Herrmann, R. Holzwarth, N. Kolachevsky, Th. Udem, and M. Zimmermann, *Phil. Trans. R. Soc. A* **363**, 2155, (2005).
- [13] C. L. Cesar, D. G. Fried, T. C. Killian, A. D. Polcyn, J. C. Sandberg, I. A. Yu, T. J. Greytak, D. Kleppner, and J. M. Doyle, *Phys. Rev. Lett.* **77**, 255 (1996).
- [14] T. Hänsch and C. Zimmermann, *Hyperfine Interact.* **76**, 47 (1993).
- [15] G. Gabrielse, *Adv. At. Mol. Opt. Phys.* **50**, 155 (2005).
- [16] K. Nakamura and Particle Data Group, *J. Phys. G: Nucl. Part. Phys.* **37**, 075021 (2010).
- [17] R. S. Van Dyck, Jr., P. B. Schwinberg, and H. G. Dehmelt, *Phys. Rev. Lett.* **59**, 26 (1987).
- [18] G. Gabrielse, A. Khabbaz, D. S. Hall, C. Heimann, H. Kalinowsky, and W. Jhe, *Phys. Rev. Lett.* **82**, 3198 (1999).
- [19] G. Gabrielse, *Adv. At. Mol. Opt. Phys.* **50**, 155 (2005).
- [20] P. J. Mohr, B. N. Taylor, and D. B. Newell, *Rev. Mod. Phys.* **80**, 633, (2008).
- [21] V. A. Kostelecký and N. Russell, *Rev. Mod. Phys.* **83**, 11 (2011).
- [22] R. Bluhm, V. A. Kostelecký, and N. Russell, *Phys. Rev. Lett.* **82**, 2254 (1999).
- [23] E. Widmann, R. S. Hayano, M. Hori, and T. Yamazaki, *Nuc. Inst. Meth. B* **214**, 31 (2004).
- [24] M. H. Holzschneider, R. E. Brown, J. B. Camp, S. Cornford, T. Darling, P. Dyer, T. Goldman, S. Høibråten, K. Hosea, R. J. Hughes, N. Jarmie, R. A. Kenefick, N. S. P. King, D. C. Lizon, M. M. Nieto, M. M. Midzor, S. P. Parry, J. Rochet, R. A. Ristinen, M. M. Schauer, J. A. Schecker, and F. C. Witteborn, *Nucl. Phys. A* **558**, 709 (1993).
- [25] J. Walz and T. Hänsch, *General Relativity and Gravitation* **36**, 561 (2004).

- [26] G. Gabrielse, *Hyperfine Interact.* **44**, 349 (1988).
- [27] A. Kellerbauer, M. Amoretti, A. S. Belov, G. Bonomi, I. Boscolo, R. S. Brusa, M. Büchner, V. M. Byakov, L. Cabaret, C. Canali, C. Carraro, F. Castelli, S. Cialdi, M. de Combarieu, D. Comparat, G. Consolati, N. Djourellov, M. Doser, G. Drobychev, A. Dupasquier, G. Ferrari, P. Forget, L. Formaro, A. Gervasini, M. G. Giammarchi, S. N. Gninenko, G. Gribakin, S. D. Hogan, M. Jacquety, V. Lagomarsino, G. Manuzio, S. Mariazzi, V. A. Matveev, J. O. Meier, F. Merkt, P. Nedelec, M. K. Oberthaler, P. Pari, M. Prevedelli, F. Quasso, A. Rotondi, D. Sillou, S. V. Stepanov, H. H. Stroke, G. Testera, G. M. Tino, G. Trenec, A. Vairo, J. Vigue, H. Walters, U. Warring, S. Zavatarelli, and D. S. Zvezhinskij, *Nuc. Inst. Meth. B* **266**, 351 (2008).
- [28] M. Doser, Progress report on the AEGIS experiment (CERN-SPSC-2011-007 / SPSC-SR-079).
- [29] J. S. Hangst, ALPHA Experimental Summary for the SPSC 2010 (CERN-SPSC-2011-004 / SPSC-SR-076).
- [30] D. Barna *et al.*, ASACUSA Status Report: ASACUSA progress during 2010 and plans for 2011 (CERN-SPSC-2011-00 / SPSC-SR-075).
- [31] G. Gabrielse, The Production and Study of Cold Antihydrogen: ATRAP Progress in 2010 (CERN-SPSC-2011-008 / SPSC-SR-080).
- [32] G. Gabrielse, X. Fei, L. A. Orozco, S. L. Rolston, R. L. Tjoelker, T. A. Trainor, J. Haas, H. Kalinowsky, and W. Kells, *Phys. Rev. A* **40**, 481 (1989).
- [33] G. Gabrielse, X. Fei, K. Helmerson, S. L. Rolston, R. L. Tjoelker, T. A. Trainor, H. Kalinowsky, J. Haas, and W. Kells, *Phys. Rev. Lett.* **57**, 2504 (1986).
- [34] G. Gabrielse, X. Fei, L. A. Orozco, R. L. Tjoelker, J. Haas, H. Kalinowsky, T. A. Trainor, and W. Kells, *Phys. Rev. Lett.* **63**, 1360 (1989).
- [35] S. L. Rolston and G. Gabrielse, *Hyperfine Interact.* **44**, 233 (1988).
- [36] G. Gabrielse, N. S. Bowden, P. A. Speck, C. H. Storry, J. N. Tan, M. Wessels, D. Grzonka, W. Oelert, G. Schepers, T. Sefzick, J. Walz, H. Pittner, and E. A. Hessels, *Phys. Lett. B* **548**, 140 (2002).
- [37] C. M. Surko, M. Leventhal, and A. Passner, *Phys. Rev. Lett.* **62**, 901 (1989).
- [38] G. Baur, *Phys. Lett. B* **311**, 343 (1993).

- [39] G. Baur, G. Boero, S. Brauksiepe, A. Buzzo, W. Eyrich, R. Geyer, D. Grzonka, J. Hauffe, K. Kilian, M. Lo Vetere, M. Macri, M. Moosburger, R. Nellen, W. Oelert, S. Passaggio, A. Pozzo, K. Rohrich, K. Sachs, G. Schepers, T. Sefzick, R. S. Simon, R. Stratmann, F. Stinzinger, and M. Wolke, *Phys. Lett. B* **368**, 251 (1996).
- [40] G. Blanford, D. C. Christian, K. Gollwitzer, M. Mandelkern, C. T. Munger, J. Schultz, and G. Zioulas, *Phys. Rev. Lett.* **80**, 3037 (1998).
- [41] G. Gabrielse, S. L. Rolston, L. Haarsma, and W. Kells, *Phys. Lett. A* **129**, (1988).
- [42] G. Gabrielse, D. S. Hall, T. Roach, P. Yesley, A. Khabbaz, J. Estrada, C. Heimann, and H. Kalinowsky, *Phys. Lett. B* **455**, 311 (1999).
- [43] G. Gabrielse, J. Estrada, J. N. Tan, P. Yesley, N. S. Bowden, P. Oxley, T. Roach, C. H. Storry, M. Wessels, J. Tan, D. Grzonka, W. Oelert, G. Schepers, T. Sefzick, W. Breunlich, M. Cargnelli, H. Fuhrmann, R. King, R. Ursin, J. Zmeskal, H. Kalinowsky, C. Wesdorp, J. Walz, K. S. E. Eikema, and T. Hänsch, *Phys. Lett. B* **507**, 1 (2001).
- [44] G. Gabrielse, A. Speck, C. H. Storry, D. Le Sage, N. Guise, D. Grzonka, W. Oelert, G. Schepers, T. Sefzick, H. Pittner, J. Walz, T. W. Hänsch, D. Comeau, and E. A. Hessels, *Phys. Rev. Lett.* **93**, 073401 (2004).
- [45] G. B. Andresen, M. D. Ashkezari, M. Baquero-Ruiz, W. Bertsche, P. D. Bowe, E. Butler, C. L. Cesar, M. Charlton, A. Deller, S. Eriksson, J. Fajans, T. Friesen, M. C. Fujiwara, D. R. Gill, A. Gutierrez, J. S. Hangst, W. N. Hardy, R. S. Hayano, M. E. Hayden, A. J. Humphries, R. Hydromako, S. Jonsell, S. L. Kemp, L. Kurchaninov, N. Madsen, S. Menary, P. Nolan, K. Olchanski, A. Olin, P. Pusa, C. Ø. Rasmussen, F. Robicheaux, E. Sarid, D. M. Silveira, C. So, J. W. Storey, R. I. Thompson, D. P. van der Werf, J. S. Wurtele, and Y. Yamazaki, *Nat. Phys.* **7**, 558 (2011).
- [46] E. A. Hessels, D. M. Homan, and M. J. Cavagnero, *Phys. Rev. A* **57**, 1668 (1998).
- [47] A. Speck, C. H. Storry, E. A. Hessels, and G. Gabrielse, *Phys. Lett. B* **597**, 257 (2004).
- [48] R. McConnell, Ph.D. thesis, Harvard University, 2011.
- [49] D. Lesage, Ph.D. thesis, Harvard University, 2008.
- [50] P. Richerme, Ph.D. thesis, Harvard University, in preparation.



- [51] D. Fitzakerley, Ph.D. thesis, York University, in preparation.
- [52] P. Larochelle, Ph.D. thesis, Harvard University, 2009.
- [53] J. Wrubel, G. Gabrielse, W. S. Kolthammer, P. Larochelle, R. McConnell, P. Richerme, D. Grzonka, W. Oelert, T. Sefzick, M. Zielinski, J. S. Borbely, M. C. George, E. A. Hessels, C. H. Storry, M. Weel, A. Müllers, J. Walz, and A. Speck, *Nucl. Instr. and Meth. A* **640**, 232 (2011).
- [54] L. S. Brown and G. Gabrielse, *Rev. Mod. Phys.* **58**, 233 (1986).
- [55] D. H. E. Dubin and T. M. O’Neil, *Rev. Mod. Phys.* **71**, 87 (1999).
- [56] T. Bergman, G. Erez, and H. Metcalf, *Phys. Rev. A* **35**, 1535 (1987).
- [57] B. Levitt, G. Gabrielse, P. Larochelle, D. Le Sage, W. S. Kolthammer, R. McConnell, J. Wrubel, A. Speck, D. Grzonka, W. Oelert, T. Sefzick, Z. Zhang, D. Comeau, M. C. George, E. A. Hessels, C. H. Storry, M. Weel, and J. Walz, *Phys. Lett. B* **656**, 25 (2007).
- [58] A. Speck, Ph.D. thesis, Harvard University, 2005.
- [59] G. Bendiscioli and D. Kharzeev, *Nuovo Cimento* **17**, 1 (1994).
- [60] Z. Zhang, Ph.D. thesis, Ruhr-Universität Bochum, 2007.
- [61] T. M. Squires, P. Yesley, and G. Gabrielse, *Phys. Rev. Lett.* **86**, 5266 (2001).
- [62] E. P. Gilson and J. Fajans, *Phys. Rev. Lett.* **90**, 015001 (2003).
- [63] L. S. Brown and G. Gabrielse, *Rev. Mod. Phys.* **58**, 233 (1986).
- [64] J. Fajans, W. Bertsche, K. Burke, S. F. Chapman, and D. P. van der Werf, *Phys. Rev. Lett.* **95**, 155001 (2005).
- [65] E. Gilson and J. Fajans, in *Non-neutral Plasma Physics IV*, edited by F. Anderegg, L. Schweikhard, and C. F. Driscoll (American Institute of Physics, New York, 2002), p. 378.
- [66] E. Gilson, Ph.D. thesis, University of California at Berkeley, 2001.
- [67] T. M. O’Neil and P. G. Hjorth, *Phys. Fluids* **28**, 3241 (1985).
- [68] G. B. Andresen, M. D. Ashkezari, M. Baquero-Ruiz, W. Bertsche, P. D. Bowe, E. Butler, C. L. Cesar, S. Chapman, M. Charlton, A. Deller, S. Eriksson, J. Fajans, T. Friesen, M. C. Fujiwara, D. R. Gill, A. Gutierrez, J. S. Hangst, W. N. Hardy, M. E. Hayden, A. J. Humphries, R. Hydomako, M. J. Jenkins,

- S. Jonsell, L. V. Jørgensen, L. Kurchaninov, N. Madsen, S. Menary, P. Nolan, K. Olchanski, A. Olin, A. Povilus, P. Pusa, F. Robicheaux, E. Sarid, S. Seif el Nasr, D. M. Silveira, C. So, J. W. Storey, R. I. Thompson, D. P. van der Werf, J. S. Wurtele, and Y. Yamazaki, *Nature* **468**, 673 (2010).
- [69] J. J. Bollinger and D. J. Wineland, *Phys. Rev. Lett.* **53**, 348 (1984).
- [70] J. J. Bollinger, D. J. Wineland, and Daniel H. E. Dubin, *Phys. Plasmas* **1**, 1403 (1994).
- [71] J. H. Malmberg and C. F. Driscoll, *Phys. Rev. Lett.* **44**, 654 (1980).
- [72] P. Oxley, N. S. Bowden, R. Parrott, A. Speck, C. Storry, J. N. Tan, M. Wessels, G. Gabrielse, D. Grzonka, W. Oelert, G. Schepers, T. Sefzick, J. Walz, H. Pittner, T. W. Hänsch, and E. A. Hessels, *Phys. Lett. B* **595**, 60 (2004).
- [73] D. H. E. Dubin, *Phys. Rev. Lett.* **66**, 2076 (1991).
- [74] R. L. Spencer, S. N. Rasband, and R. R. Vanfleet, *Phys. Fluids B* **5**, 4267 (1993).
- [75] A. Speck, G. Gabrielse, P. Larochele, D. Le Sage, B. Levitt, W. S. Kolthammer, R. McConnell, J. Wrubel, D. Grzonka, W. Oelert, T. Sefzick, Z. Zhang, D. Comeau, M. C. George, E. A. Hessels, C. Storry, M. Weel, and J. Walz, *Phys. Lett. B* **650**, 119 (2007).
- [76] M. D. Tinkle, R. G. Greaves, C. M. Surko, R. L. Spencer, and G. W. Mason, *Phys. Rev. Lett.* **40**, 352 (1994).
- [77] D. J. Heinzen, J. J. Bollinger, F. L. Moore, W. M. Itano, and D. J. Wineland, *Phys. Rev. Lett.* **66**, 2080 (1991).
- [78] T. Mitchell, J. Bollinger, X.-P. Huang, and W. Itano, *Opt. Express* **2**, 314 (1998).
- [79] C. S. Weimer, J. J. Bollinger, F. L. Moore, and D. J. Wineland, *Phys. Rev. A* **49**, 3842 (1994).
- [80] M. Amoretti, G. Bonomi, A. Bouchta, P. D. Bowe, C. Carraro, C. L. Cesar, M. Charlton, M. Doser, A. Fontana, M. C. Fujiwara, R. Funakoshi, P. Genova, J. S. Hangst, R. S. Hayano, L. V. Jorgensen, V. Lagomarsino, R. Landua, E. L. Rizzini, M. Macri, N. Madsen, G. Manuzio, G. Testera, A. Variola, and D. P. van der Werf, *Phys. Plasmas* **10**, 3056 (2003).
- [81] E. Butler, Ph.D. thesis, Swansea University, 2011.

- [82] X.-P. Huang, F. Anderegg, E. M. Hollmann, C. F. Driscoll, and T. M. O'Neil, *Phys. Rev. Lett.* **78**, 875 (1997).
- [83] F. Anderegg, E. M. Hollmann, and C. F. Driscoll, *Phys. Rev. Lett.* **81**, 4875 (1998).
- [84] E. M. Hollmann, F. Anderegg, and C. F. Driscoll, *Phys. Plasmas* **7**, 2776 (2000).
- [85] J. R. Danielson and C. M. Surko, *Phys. Rev. Lett.* **94**, 035001 (2005).
- [86] J. R. Danielson and C. M. Surko, *Phys. Plasmas* **13**, 055706 (2006).
- [87] J. R. Danielson and C. M. Surko, in *Non-Neutral Plasma Physics VI*, edited by M. Drewsen, U. Uggerhøj, and H. Knudsen (American Institute of Physics, New York, 2006), p. 19.
- [88] X.-P. Huang, J. J. Bollinger, T. B. Mitchell, and W. M. Itano, *Phys. Rev. Lett.* **80**, 73 (1998).
- [89] X.-P. Huang, J. J. Bollinger, T. B. Mitchell, W. M. Itano, and D. H. E. Dubin, *Phys. Plasmas* **5**, 1656 (1998).
- [90] R. G. Greaves and C. M. Surko, *Phys. Rev. Lett.* **85**, 1883 (2000).
- [91] L. V. Jørgensen, M. Amoretti, G. Bonomi, P. D. Bowe, C. Canali, C. Carraro, C. L. Cesar, M. Charlton, M. Doser, A. Fontana, M. C. Fujiwara, R. Funakoshi, P. Genova, J. S. Hangst, R. S. Hayano, A. Kellerbauer, V. Lagomarsino, R. Landua, E. Lodi Rizzini, M. Macrì, N. Madsen, D. Mitchard, P. Montagna, A. Rotondi, G. Testera, A. Variola, L. Venturelli, D. P. van der Werf, and Y. Yamazaki, *Phys. Rev. Lett.* **95**, 025002 (2005).
- [92] R. Funakoshi, M. Amoretti, G. Bonomi, P. D. Bowe, C. Canali, C. Carraro, C. L. Cesar, M. Charlton, M. Doser, A. Fontana, M. C. Fujiwara, P. Genova, J. S. Hangst, R. S. Hayano, L. V. Jørgensen, A. Kellerbauer, V. Lagomarsino, R. Landua, E. Lodi Rizzini, M. Macrì, N. Madsen, G. Manuzio, D. Mitchard, P. Montagna, L. G. C. Posada, A. Rotondi, G. Testera, A. Variola, L. Venturelli, D. P. van der Werf, Y. Yamazaki, and N. Zurlo, *Phys. Rev. A* **76**, 012713 (2007).
- [93] C. H. Storry, A. Speck, D. Le Sage, N. Guise, G. Gabrielse, D. Grozonka, W. Oelert, G. Scheppers, T. Seftick, J. Walz, H. Pittner, M. Herrmann, T. W. Hänsch, D. Comeau, and E. A. Hessels, *Phys. Rev. Lett.* **93**, 263401 (2004).
- [94] F. Robicheaux, *J. Phys. B* **41**, 192001 (2008).
- [95] D. L. Eggleston, C. F. Driscoll, B. R. Beck, A. W. Hyatt, and J. H. Malmberg, *Phys. Fluids B* **4**, 3432 (1992).

- [96] M. Glinsky, T. O'Neil, M. N. Rosenbluth, K. Tsuruta, and S. Ichimaru, *Phys. Fluids B* **4**, 1156 (1992).
- [97] W. Ketterle and N. J. Van Druten, *Adv. At. Mol. Opt. Phys.* **37**, 181 (1996).
- [98] C. Biedermann G. Fussmann and R. Radtke, in *Advanced Technologies Based on Wave and Beam Generated Plasmas*, edited by H. Schlüter and A. Shivarova (Kluwer Academic Publishers, Netherlands, 1999), p. 429.
- [99] L. Spitzer, *Physics of Fully Ionized Gases* (Interscience Publishers, New York, 1962).
- [100] D. K. Geller and J. C. Weisheit, *Phys. Plasmas* **4**, 4258 (1997).
- [101] T. M. O'Neil and C. F. Driscoll, *Physics of Fluids* **22**, 266 (1979).
- [102] G. W. Hart and B. G. Peterson, *Phys. Plasmas* **13**, 022101 (2006).
- [103] G. Gabrielse, W. S. Kolthammer, R. McConnell, P. Richerme, R. Kalra, E. Novitski, D. Grzonka, W. Oelert, T. Sefzick, M. Zielinski, D. Fitzakerley, M. C. George, E. A. Hessels, C. H. Storry, M. Weel, A. Müllers, and J. Walz, *Phys. Rev. Lett.* **106**, 073002 (2011).
- [104] G. B. Andresen, M. D. Ashkezari, M. Baquero-Ruiz, W. Bertsche, P. D. Bowe, E. Butler, C. L. Cesar, S. Chapman, M. Charlton, J. Fajans, T. Friesen, M. C. Fujiwara, D. R. Gill, J. S. Hangst, W. N. Hardy, R. S. Hayano, M. E. Hayden, A. Humphries, R. Hydromako, S. Jonsell, L. Kurchaninov, R. Lambo, N. Madsen, S. Menary, P. Nolan, K. Olchanski, A. Olin, A. Povilus, P. Pusa, F. Robicheaux, E. Sarid, D. M. Silveira, C. So, J. W. Storey, R. I. Thompson, D. P. van der Werf, D. Wilding, J. S. Wurtele, and Y. Yamazaki, *Phys. Rev. Lett.* **105**, 013003 (2010).
- [105] Daniel H. E. Dubin, *Phys. Rev. E* **53**, 5268 (1996).
- [106] Daniel H. E. Dubin, *Phys. Plasmas* **12**, 042107 (2005).
- [107] M. Amoretti, C. Amsler, G. Bonomi, A. Bouchta, P. D. Bowe, C. Carraro, C. L. Cesar, M. Charlton, M. Doser, V. Filippini, A. Fontana, M. C. Fujiwara, R. Funakoshi, P. Genova, J. S. Hangst, R. S. Hayano, L. V. Jørgensen, V. Lagomarsino, R. Landua, D. Lindelöf, E. Lodi Rizzini, M. Macrí, N. Madsen, G. Manuzio, P. Montagna, H. Pruys, C. Regenfus, A. Rotondi, G. Testera, A. Variola, and D. P. van der Werf, *Phys. Rev. Lett.* **91**, 55001 (2003).
- [108] H. Higaki, N. Kuroda, T. Ichioka, K. Yoshiki Franzen, Z. Wang, K. Komaki, Y. Yamazaki, M. Hori, N. Oshima, and A. Mohri, *Phys. Rev. E* **65**, 046410 (2002).

- [109] F. Andereg, N. Shiga, D. H. E. Dubin, C. F. Driscoll, and R. W. Gould, *Phys. Plasmas* **10**, 1556 (2003).
- [110] N. Shiga, F. Andereg, D. H. E. Dubin, C. F. Driscoll, and R. W. Gould, *Phys. Plasmas* **13**, 022109 (2006).
- [111] Daniel H. E. Dubin, *Phys. Rev. Lett.* **94**, 025002 (2005).
- [112] B. R. Beck, J. Fajans, and J. H. Malmberg, *Phys. Plasmas* **3**, 1250 (1996).
- [113] F. Robicheaux and J. Fajans, *J. Phys. B* **40**, 3143 (2007).
- [114] G. Gabrielse, *Adv. At. Mol. Opt. Phys.* **45**, 1 (2001).
- [115] H. Imao, K. Michishio, Y. Kanai, N. Kuroda, Y. Enomoto, H. Higaki, K. Kira, A. Mohri, H. A. Torii, Y. Nagata, C. Kim, Y. Matsuda, Y. Nagashima, and Y. Yamazaki, *J. Phys. Conf. Ser.* **225**, 012018 (2010).
- [116] G. Gabrielse, N. S. Bowden, P. Oxley, A. Speck, C. H. Storry, J. N. Tan, M. Wessels, D. Grzonka, W. Oelert, G. Schepers, T. Sefzick, J. Walz, H. Pittner, and E. A. Hessels, *Phys. Lett. B* **548**, 140 (2002).
- [117] G. B. Andresen, W. Bertsche, P. D. Bowe, C. C. Bray, E. Butler, C. L. Cesar, S. Chapman, M. Charlton, J. Fajans, M. C. Fujiwara, R. Funakoshi, D. R. Gill, J. S. Hangst, W. N. Hardy, R. S. Hayano, M. E. Hayden, R. Hydomako, M. J. Jenkins, L. V. Jorgensen, L. Kurchaninov, R. Lambo, N. Madsen, P. Nolan, K. Olchanski, A. Olin, A. Povilus, P. Pusa, F. Robicheaux, E. Sarid, S. Seif El Nasr, D. M. Silveira, J. W. Storey, R. I. Thompson, D. P. van der Werf, J. S. Wurtele, and Y. Yamazaki, *Phys. Rev. Lett.* **100**, 203401 (2008).
- [118] N. Kuroda, H. A. Torii, M. Shibata, Y. Nagata, D. Barna, M. Hori, D. Horváth, A. Mohri, J. Eades, K. Komaki, and Y. Yamazaki, *Phys. Rev. Lett.* **100**, 203402 (2008).
- [119] C. A. Ordonez, *Phys. Rev. E* **76**, 017402 (2007).
- [120] T. M. O'Neil, *Physics of Fluids* **24**, 1447 (1981).
- [121] D. J. Larson, J. C. Bergquist, J. J. Bollinger, W. M. Itano, and D. J. Wineland, *Phys. Rev. Lett.* **57**, 70 (1986).
- [122] D. Wineland, C. Weimer, and J. Bollinger, *Hyperfine Interact.* **76**, 115 (1993).
- [123] H. Imajo, K. Hayasaka, R. Ohmukai, U. Tanaka, M. Watanabe, and S. Urabe, *Phys. Rev. A* **55**, 1276 (1997).

- [124] B. M. Jelenkovic, A. S. Newbury, J. J. Bollinger, W. M. Itano, and T. B. Mitchell, *Phys. Rev. A* **67**, 063406 (2003).
- [125] G. Gabrielse, W. S. Kolthammer, R. McConnell, P. Richerme, J. Wrubel, R. Kalra, E. Novitski, D. Grzonka, W. Oelert, T. Sefzick, M. Zielinski, J. S. Borge, D. Fitzakerley, M. C. George, E. A. Hessels, C. H. Storry, M. Weel, A. Müllers, J. Walz, and A. Speck, *Phys. Rev. Lett.* **105**, 213002 (2010).
- [126] G. Gabrielse, X. Fei, L. A. Orozco, R. L. Tjoelker, J. Haas, H. Kalinowsky, T. A. Trainor, and W. Kells, *Phys. Rev. Lett.* **63**, 1360 (1989).
- [127] G. B. Andresen, M. D. Ashkezari, M. Baquero-Ruiz, W. Bertsche, P. D. Bowe, E. Butler, C. L. Cesar, S. Chapman, M. Charlton, A. Deller, S. Eriksson, J. Fajans, T. Friesen, M. C. Fujiwara, D. R. Gill, A. Gutierrez, J. S. Hangst, W. N. Hardy, M. E. Hayden, A. J. Humphries, R. Hydomako, S. Jonsell, N. Madsen, S. Menary, P. Nolan, A. Olin, A. Povilus, P. Pusa, F. Robicheaux, E. Sarid, D. M. Silveira, C. So, J. W. Storey, R. I. Thompson, D. P. van der Werf, J. S. Wurtele, and Y. Yamazaki, *Phys. Rev. Lett.* **106**, 145001 (2011).
- [128] R. B. Meinke, C. Goodzeit, W. Hinson, C. Gung, J. Minervini, A. Radovinsky, J. Schultz, B. Smith, R. Camille, and L. Myatt, *Proceedings of the 2001 Particle Accelerator Conference* 3436 (2001).
- [129] P. Wanderer, M. Anerella, J. Escallier, A. Ghosh, A. Jain, A. Marone, J. Muratore, B. Parker, A. Prodell, P. Thompson, and K. C. Wu, *IEEE T. Appl. Supercon.* **12**, 305 (2002).
- [130] B. Parker and J. Escallier, *Proceedings of the 2005 Particle Accelerator Conference* 737 (2005).
- [131] W. Bertsche, A. Boston, P. D. Bowe, C. L. Cesar, S. Chapman, M. Charlton, M. Chartier, A. Deutsch, J. Fajans, M. C. Fujiwara, R. Funakoshi, Gomberoff, J. S. Hangst, R. S. Hayano, M. J. Jenkins, L. V. Jorgensen, P. Ko, N. Madsen, P. Nolan, R. D. Page, L. G. C. Posada, A. Povilus, E. Sarid, D. M. Silveira, D. P. van der Werf, Y. Yamazaki, B. Parker, J. Escallier, and A. Ghosh, *Nuc. Inst. Meth. A* **566**, 746 (2006).
- [132] C. Gung, J. V. Minervini, J. H. Schultz, R. B. Meinke, C. L. Goodzeit, G. Sabbi, and P. Seidl, *IEEE T. Appl. Supercon.* **13**, 1508 (2003).
- [133] N. N. Matovetsky, R. R. Manahan, R. B. Meinke, L. Chiesa, A. F. Lietzke, G. L. Sabbi, and P. A. Seidl, *IEEE T. Appl. Supercon.* **14**, 316 (2004).
- [134] M. N. Wilson, *Superconducting Magnets* (Oxford University Press, Oxford, 2002).

- 
- [135] J. Weinstein, Ph.D. thesis, Harvard University, 2001.